

Unveiling a multiscale view of massive star and cluster formation

LAW CHI YAN

Department of Space, Earth and Environment
CHALMERS UNIVERSITY OF TECHNOLOGY
Gothenburg, Sweden 2022

THESIS FOR THE DEGREE OF LICENTIATE OF PHILOSOPHY

Unveiling a multiscale view of massive star and cluster formation

LAW CHI YAN



Department of Space, Earth and Environment
CHALMERS UNIVERSITY OF TECHNOLOGY
Göteborg, Sweden 2022

Unveiling a multiscale view of massive star and cluster formation
LAW CHI YAN

© LAW CHI YAN, 2022.

Licentiatavhandlingar vid Chalmers tekniska högskola
Technical report No. 3471
ISSN 0346-718X

Department of Space, Earth and Environment
Chalmers University of Technology
SE-412 96 Göteborg, Sweden
Telephone + 46 (0) 31 – 772 1000

Cover: ALMA 1.3mm total continuum image of the massive protostellar system
G28.2-0.05.

Typeset by the author using L^AT_EX.

Printed by Chalmers Reproservice
Göteborg, Sweden 2022

*When I consider your heavens, the work of your fingers, the moon and the stars,
which you have set in place, what is man that you are mindful of him, the son of
man that you care for him? (Psalm 8: 3-4)*

Abstract

Massive stars regulate the physical and chemical evolution of galaxies. Most stars within these galaxies, including massive ones, appear to be born in star clusters and associations. However, many questions remain unanswered about how massive stars and clusters form from the diffuse gas of interstellar space. For example it is not yet known whether magnetic fields, turbulence or feedback are the most important actors in regulating gravitational collapse to give birth to these systems. It is also unclear to what extent potential protostellar crowding within a protocluster may affect massive star formation. Overdense clumps within giant molecular clouds (GMCs), often appearing in their earliest phases as infrared dark clouds (IRDCs), are the nurseries of massive stars and clusters. Properties of turbulence and magnetic fields in IRDCs are thus important to measure to give inputs for theoretical models of the formation processes. On the smaller scales of individual massive star formation, various theories, including core accretion, competitive accretion and protostellar collisions, may be viable depending on environmental conditions. Hence, studying how massive stars are forming in environments with relatively extreme conditions, e.g., in terms of crowding or isolation, may yield the most stringent constraints on these models.

This licentiate thesis first presents a study of a massive protostar (G28.2-0.05) that appears to be forming in relative isolation. Observational data, especially from the Atacama Large Millimeter/Submillimeter Array (ALMA), are used to investigate the nature of the system, including its dense and ionized gas structures, small-scale kinematics and dynamics and large-scale outflows. Mid to Far Infrared observations and archival data are used to measure the spectral energy distribution (SED) to further constrain protostellar properties. We conclude the system is a massive ($\sim 24 M_{\odot}$) protostar that has an accretion powered wide angle bipolar molecular outflow and is also in the first stages of producing significant ionizing feedback. An examination of the mm dust continuum emission in the surroundings finds a near complete dearth of other sources, which is evidence for the system's isolation and a strong constraint on competitive accretion models. Overall, core accretion models appear to give a good description of the protostar.

We also present first results of an observational program that attempts to use molecular gas kinematics and dust polarized continuum emission to measure properties of turbulence and magnetic fields across a range of scales from GMCs to IRDCs to individual massive protostars. We discuss the methods to be used and present the first data collected for the project. The overall work of this thesis leads in a direction of characterization of both large-scale molecular cloud environments and individual massive protostars forming within them to reveal a holistic, multi-scale view of the birth of massive stars and clusters.

Keywords: ISM: clouds — stars: formation

Acknowledgments

I want to sincerely thank my supervisor, Jonathan Tan, for all his help and guidance and for being super patient. I also thank him for really giving me the experience of what is meant to be an independent researcher, in both attitude and also the skills (even on a figure) to work on my Ph.D. projects. I also thank Jouni Kainulainen for being my second supervisor, for providing suggestions and valuable advice in navigating a research career or on the attitude in conducting research. I would like to thank Prasanta Gorai, Giuliana Cosentino, Rubén Fedriani, Juan Farias, and Yichen Zhang for hearing me out on many things, on and off research, and being patient with me in providing helpful feedback on my research and writing. I also want to thank Daniel Tafoya, Maria Carmen Toribio and the Nordic ALMA arcnode staff for the great help during long and painful ALMA data reduction and understanding the ALMA data. I also want to thank Wouter Vlemmings for being my examiner, giving me feedback on my thesis and helpful advice along the way.

It is my honor to meet a lot of amazing colleagues at Chalmers and Onsala Space Observatory, who have helped me out a lot throughout my Ph.D. I would first sincerely thank Andri Spilker, Chia-Jung Hsu, Kyoko Onishi, Sara Piras, Sandra Treviño Morales and Mamiko Sato. I cannot imagine what my Ph.D. life would be like without you guys, even though I know I am really bad in communications! I am also really grateful to meet Iskra Georgieva, Kiana Kade, Jan Orkisz, Sara Rezaei Kh. and many others. My Ph.D. life becomes lively with you guys around!

Finally and most importantly, I would want to give a huge thanks to my family in Hong Kong for the great support in all the ups and downs! I also want to thank all the brothers and sisters in Christ near and far (NCCC Göteborg, Kwan's, CFC (youth), Boys, Elpida, research fellowship, and more).

LAW CHI YAN
Göteborg, January 2022

List of Publications

This thesis is based on the following appended papers:

Paper 1. Chi-Yan Law, Jonathan C. Tan, Prasanta Gorai, Yichen Zhang, Rubén Fedriani, Daniel Tafoya, Kei Tanaka, Giuliana Cosentino and Yao-Lun Yang. *Isolated Massive Star Formation in G28.2-0.05*, in prep. for submission to the Astrophysical Journal.

Other publications not included in this Licentiate:

Law, C. Y., Li, H.-B, Cao Zhuo and Ng, C.-Y. *The links between magnetic fields and filamentary clouds III: field regulated mass cumulative functions* Monthly Notices of the Royal Astronomical Society, Volume 498, Issue 1, pp. 850, 2020.

Álvarez-Gutiérrez, R. H., Stutz, A. M., **Law, C. Y.**, Reissl, S., Klessen, R. S., Leigh, N. W. C., Liu, H. -L. and Reeves, R. A. *Filament Rotation in the California L1482 Cloud* The Astrophysical Journal, Volume 908, Issue 1, pp. 86, 2021.

Álvarez-Gutiérrez, R. H., Stutz, A. M., **Law, C. Y.**, Reissl, S., Klessen, R. S., Leigh, N. W. C., Liu, H. -L. and Reeves, R. A. *Filament Rotation in the California L1482 Cloud* The Astrophysical Journal, Volume 908, Issue 1, pp. 86, 2021.

Barnes, A. T.,..., **Law, C. Y.**, et al, *ALMA-IRDC: dense gas mass distribution from cloud to core scales* Monthly Notices of the Royal Astronomical Society, Volume. 503, Issue 3, pp. 4601, 2021.

Fontani, F.,..., **Law, C. Y.**, et al, *ALMA-IRDC - II. First high-angular resolution measurements of the N-14/N-15 ratio in a large sample of infrared-dark cloud cores* Monthly Notices of the Royal Astronomical Society, Volume 503, Issue 3, pp. 4320, 2021.

Contents

Abstract	iv
Acknowledgments	v
List of Publications	vii
 I Introduction	 1
1 Scientific context	3
2 Physical processes and evolutionary stages of massive star and star cluster formation	7
2.1 Physical processes	7
2.2 Evolutionary stages	10
2.2.1 Infrared dark clouds (IRDCs)	10
2.2.2 Fragmentation of IRDCs into Prestellar Cores	13
2.2.3 Massive protostellar cores / hot molecular cores	16
2.2.4 Ionizing feedback as traced by HII regions	17
2.3 A short note on interferometry	19
3 Paper summary and future works	23
3.1 Paper summary	23
3.2 Future works	23
4 Turbulence and magnetic fields in IRDC G38.9-0.74	25
4.1 Introduction	25
4.2 Methods	26
4.2.1 Velocity Channel Gradient (VCG)	26
4.3 Observational Data	27
4.3.1 GBT-ARGUS ^{13}CO data	27
4.3.2 SOFIA-HAWC+ polarized dust emission data	28
4.4 Results	28
4.4.1 CO Kinematics	28
4.4.2 Polarized Dust Emission	28
4.4.3 B-field Analysis	29

II	Appended papers	41
1	Isolated Massive Star Formation in G28.2-0.05	43

Part I

Introduction

Chapter 1

Scientific context

Stars are the main visible, baryonic component of the Milky Way and most other galaxies. Depending on their mass, stars will evolve to different outcomes (see Fig. 1.1), with ‘massive’ or ‘high-mass’ stars typically being defined as those that start their lives with eight solar masses or more. These massive stars eventually end their lives in core collapse supernova explosions. While the theory of stellar evolution is relatively well developed and understood, one key aspect where many open questions remain is in the crucial formation stage of the stars from the interstellar medium (ISM). This Licentiate thesis contributes to understanding the processes of the formation of massive stars and star clusters.

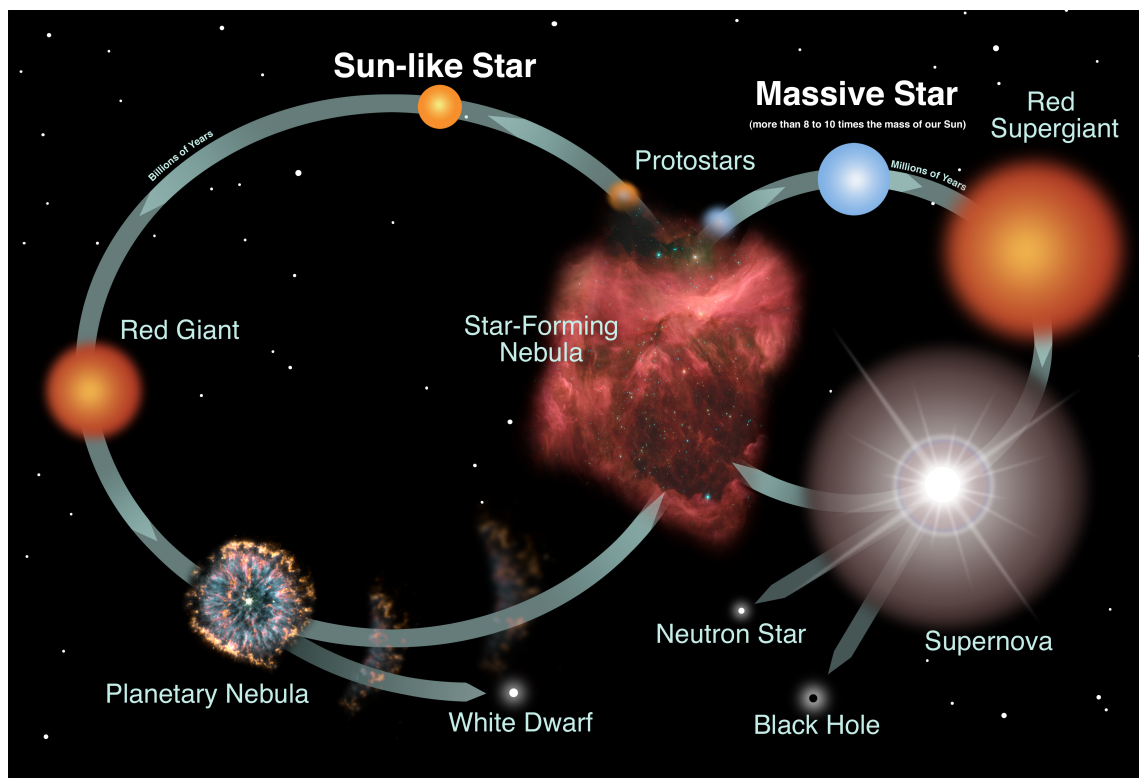


Figure 1.1: A simplified synoptic diagram summarizing the main stages of the life cycle of stars. (Credit: Image credit: NASA and Night Sky Network).

While massive stars are a relatively small fraction of the total stellar mass, they dominate radiative, mechanical and chemical feedback on the ISM and galaxies, including via the regulation of further star formation. For instance, at very early stages, forming massive protostars may shape the physical conditions of any surrounding protocluster by radiative heating and mechanical feedback from outflows. Eventually stellar winds and ionizing feedback from fully formed massive stars are likely to be the main agents that disperse remnant molecular gas halting further star formation in the vicinity. Massive stars are responsible for the nucleosynthesis of most chemical species. The nucleosynthetic yields from supernovae help set galactic chemical evolution (e.g. Kobayashi et al., 2011; Romano et al., 2019)

Thus we see that massive stars have important impacts on many aspects of astrophysical processes. However, there remain many open questions concerning the formation process or processes of massive stars. Supersonic turbulence, magnetic fields and feedback are expected to be the main mechanisms interacting with gravitational collapse to regulate massive star and star cluster formation. However, the relative importance between them are debated. Various theoretical models have been proposed, which involve different relative importance between these mechanisms (see, e.g., Tan et al., 2014, for a review)

While this thesis will focus on the formation of massive stars, it is first worth providing a summary of the main stages of the more well studied process of low-mass star formation, since this forms the basis of one of the main classes of massive star formation theories, i.e., core accretion. Figure 1.2 presents a schematic diagram of low-mass star formation. Giant molecular clouds (GMCs) are mainly composed of molecular hydrogen and are the primary sites of massive star and star cluster formation in our Galaxy. Observational studies of the gas motion in GMCs suggest that they are supersonically turbulent. Polarimetric studies toward molecular clouds indicate an ordered magnetic field morphology, which suggests that magnetic fields also play a role in regulating the large-scale environment of star formation. In the densest regions ('clumps') in molecular clouds, where gravity starts to dominate, prestellar cores emerge. Within these a quasi-hydrostatic protostar forms and the system is then referred to as a protostellar core. As gas infalls, rotational support tends to increase and accretion is mediated via a disk. Associated with this disk is the launching of bipolar protostellar outflows, which are accretion powered, but launched by magnetic fields that are spinning with the disk. These outflows are the main agents of feedback that disperse a significant fraction of gas that is in the core, such that its efficiency of star formation may be only $\sim 30 - 50\%$. The young low-mass star will then become visible as a pre-main sequence T-Tauri object.

One of the main open questions in massive star formation research is whether this evolutionary sequence can be scaled-up to be applicable to birth of massive stars. Another related open question is the role of the protocluster environment on massive star formation. Finally, defining an evolutionary sequence for star cluster formation and understanding the key processes that control it remains another outstanding challenge. Thus motivated, this Licentiate thesis aims, in Paper I, to provide an observational study of the physical properties of a massive protostellar system, G28.2-0.05, which is already known to be exhibiting the early stages of ionizing feedback by

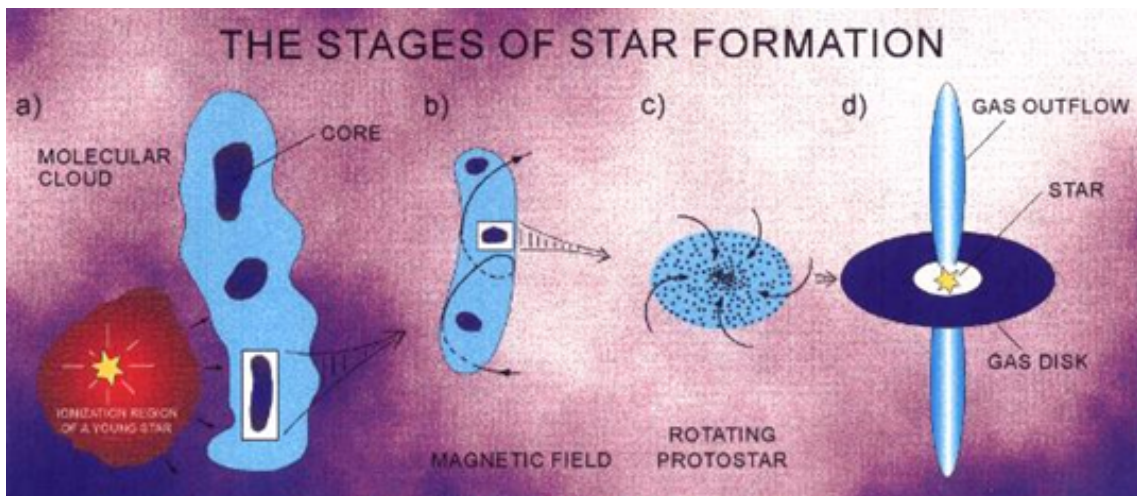


Figure 1.2: A schematic diagram illustrating the major stages of low-mass star formation. Molecular clouds are the environments from which stars form. Dense regions (also known as ‘clumps’) where gravity dominates over turbulence and magnetic fields collapse and fragment into dense cores. Within the cores, protostars are born, each fed by a rotating disk and collapsing envelope. The disks launch bipolar outflows that disperse the remaining core gas to reveal a pre-main sequence T-Tauri star, which can still retain a circumstellar disk. (Credit: The Arizona Radio Observatory).

creating an Ultra-Compact HII (UC-HII) region. One feature of particular interest revealed by our study is that this massive star appears to be forming in relative isolation. Preliminary results also presented in this thesis (to appear as Paper II) toward the large-scale gas-kinematics and magnetic field properties of an infrared dark cloud (IRDC), with these systems known to be the progenitors of massive star and star cluster formation.

Before presentation of the papers, in Chapter 2 we first summarise relevant scientific background on key topics. In particular we overview the interaction of self-gravity with turbulence, magnetic fields and feedback. We also summarise the main evolutionary phases of massive star and star cluster formation, including infrared dark clouds (IRDCs), star-forming clumps, pre-stellar cores, protostellar cores (including hot molecular cores), and HII regions. Chapter 3 presents a summary of the papers. Chapter 4 discusses future work and outlook.

Chapter 2

Physical processes and evolutionary stages of massive star and star cluster formation

2.1 Physical processes

Massive star and star cluster formation requires gravitational collapse, but this may also be regulated by the processes of magnetic field support, turbulence and feedback from the forming star or surrounding stars. However, the relative importance of these processes is unknown. Here we review key aspects about the processes relevant at early stages in IRDCs, i.e., only focusing on gravity, magnetic fields and turbulence, and assuming feedback is relatively weak. A more extensive review of these topics is given by McKee and Ostriker (2007)

Gravitational collapse: The key parameter that evaluates the importance of self-gravity for a structure is the virial parameter, α_{vir} , (Bertoldi and McKee, 1992) which measures the ratio of internal kinetic to gravitational energy. For a spherical system, the virial parameter is given by:

$$\alpha_{\text{vir}} \equiv 5\sigma^2 R / (GM), \quad (2.1)$$

where σ is the 1D velocity dispersion, R is the radius, G is the gravitational constant and M is the mass. According to the simple virial theorem (neglecting surface terms and magnetic fields), a system is in virial equilibrium if the internal kinetic energy, K , and the gravitational potential energy, U , satisfy:

$$2T + U = 0. \quad (2.2)$$

For a uniform density sphere, virial equilibrium is thus equivalent to $\alpha_{\text{vir}} = 1$, which the condition of being gravitationally bound is given by $\alpha_{\text{vir}} < 2$. The terms ‘sub-virial’ and ‘super-virial’ are often used to describe systems that have $\alpha_{\text{vir}} < 1$ and > 1 , respectively. Bertoldi and McKee (1992) have evaluated the effects of internal (power law) density structure and elongation (i.e., ellipsoidal structures) on the virial parameter and the condition for virial equilibrium. They have also examined the effects of magnetic fields and surface pressure terms.

For a system that is gravitational bound and unstable and in the limit of negligible internal pressure support, the timescale for collapse is described as the ‘free-fall’ time and is given by:

$$t_{\text{ff}} = \sqrt{\frac{3\pi}{32G\rho}} = \frac{4.4 \times 10^4 \text{ yr}}{\sqrt{n_{\text{H}}/10^6 \text{ cm}^{-3}}}, \quad (2.3)$$

where n_{H} is the number density of hydrogen nuclei and the normalization assumes $n_{\text{He}} = 0.1n_{\text{H}}$.

Magnetic fields: Magnetic fields act as an additional pressure term that can provide support against gravitational collapse. The relative importance of the magnetic energy and gravitational energy in a structure is described by the mass-to-flux ratio, λ . The critical mass-to-flux ratio for gas to be able to collapse against magnetic pressure is defined by (Krumholz, 2011):

$$\lambda_{\text{crit}} = \left(\frac{M}{\Phi}\right)_{\text{crit}} = \frac{c_{\Phi}}{G^{1/2}}, \quad (2.4)$$

where Φ is the magnetic flux and c_{Φ} is a dimensionless coefficient that is related to the shape and the density distribution of the cloud. If $\lambda > \lambda_{\text{crit}}$, the system is said to be magnetically supercritical, i.e., B -fields cannot prevent collapse. If $\lambda < \lambda_{\text{crit}}$, the system is said to be magnetically subcritical, i.e., B -fields prevent collapse, but only in directions perpendicular to the field lines and only if the material is well-coupled to the field lines by being sufficiently ionized.

As both magnetic fields and turbulence may provide support against gravity, it is normal to compare their relative importance. A key parameter for this is the Alfvén Mach number (M_A), defined as the ratio between the turbulence velocity (v) and the Alfvén velocity (v_a), where $v_a = B/(4\pi\rho)^{1/2}$ (Krumholz, 2011). The ratio of magnetic to turbulent energy densities (i.e., pressures) is described by

$$\beta = \frac{2M_A^2}{M_s^2}, \quad (2.5)$$

where M_s is the sonic Mach number of the turbulence, i.e., the ratio of turbulent velocity dispersion to sound speed.

Molecular clouds are mostly neutral. Only the ions are directly coupled to the magnetic fields and neutral can undergo ‘ambipolar’ drift across field lines (Ward-Thompson and Whitworth, 2011). For a structure with length scale L and threaded by magnetic field with an average uniform strength B , the ambipolar diffusion timescale, t_{AD} , is:

$$t_{\text{AD}} \sim \frac{8\pi L^2}{B^2} n_n n_i \langle \sigma v \rangle \frac{\mu_n \mu_i}{\mu_n + \mu_i}, \quad (2.6)$$

where n_n, n_i are the number density of neutral and ion species, respectively, μ_n and μ_i are the mean masses of these neutral and ion species, and $\langle \sigma v \rangle$ is the collision rate coefficient between the ion and neutral species. For typical conditions, t_{AD} can be about 10 times longer than t_{ff} .

Magnetic fields are expected to have an effect on the orientation of dust grains, with the long axis of the grains aligning in directions perpendicular to the field lines.

Thus the thermal continuum emission from the such aligned grains is expected to be polarized with direction of polarization perpendicular to the (projected) B -field orientation in the plane of the sky (see, e.g. Crutcher, 2012). Thus mapping FIR/sub-mm polarization of molecular clouds provides a method to infer plane of sky B -field morphology. Once this morphology is mapped, if the turbulent velocity dispersion is known, then, from the degree of ordering of the polarization vectors, the B -field strength can be estimated via the Davis-Chandrasekhar-Fermi (DCF) method (Chandrasekhar and Fermi, 1953). However, there are number of caveats associated with this, including the effects of self-gravity in distorting B -field orientations. The most direct method of inferring B -field strengths (along the line of sight) remains via measuring Zeeman splitting of certain line emission. Via this method, quite constant B -field strengths of $\sim 10 \mu\text{G}$ have been inferred in clouds with densities up to $n_{\text{H}} \sim 300 \text{ cm}^{-3}$. At higher densities, the field strength is observed to increase as $B \sim 10(n_{\text{H}}/300 \text{ cm}^{-3})^{0.65} \mu\text{G}$ (Crutcher, 2012).

Turbulence: The large-scale gas motions in molecular clouds are observed to be supersonic turbulent (Krumholz, 2011). Statistical properties of the turbulence may depend on the environmental and star formation properties of the cloud (see, e.g., Burkhart, 2021, for a review). Two basic parameters are used to describe the observed properties of turbulent gas are the Reynolds number and the sonic Mach number. The Reynolds number is defined by the following equation at a length scale (L), gas velocity (v) and viscosity (ν):

$$\text{Re} = vL/\nu. \quad (2.7)$$

Gas flow with a low Reynolds number is characterized by ordered, laminar flow. Gas flow with large Reynolds number develops turbulence.

The sonic Mach number (M_s) is the ratio of turbulent velocity dispersion to sound speed. In molecular clouds, the temperatures are $\sim 10 \text{ K}$, i.e., with sound speeds of $\sim 0.2 \text{ km s}^{-1}$. Observed 1D velocity dispersions of IRDCs and GMCs can be ~ 1 to 10 km s^{-1} , implying $M_s \sim 5$ to 50 . Thus the turbulence is described as being supersonic, which is expected to lead to a network of shock compressed regions. Shocks dissipate energy, so supersonic turbulence is expected to decay relatively quickly, i.e., with an exponential decay time that is about equal to a flow crossing time $t_{\text{cross}} = L/v$, which is similar to a free-fall time for a self-gravitating cloud.

The classic study by Larson (Larson, 1981) found that the internal velocity dispersion of CO velocity spectra (Δv) are correlated with the cloud sizes (L). The correlation can be described by a power-law ($\Delta v \propto L^{0.38}$). More recent studies find a power law index of about 0.5 McKee and Ostriker (see, e.g., 2007). The value of this index is an important property to describe the nature of interstellar turbulence.

An important property of turbulent gas flow in relation with magnetic fields is the potential anisotropic nature of the flow. If the magnetic field is dynamically important, then a greater degree of anisotropy is expected, with energy dissipation perpendicular to the B -field happening faster than along the field, i.e., motions are more constrained in directions perpendicular to the B -field. This aspect is summarised in Figure 2.1. The turbulence eddies are represented as ellipses, that have major axes in direction aligned with the local magnetic field direction, while the

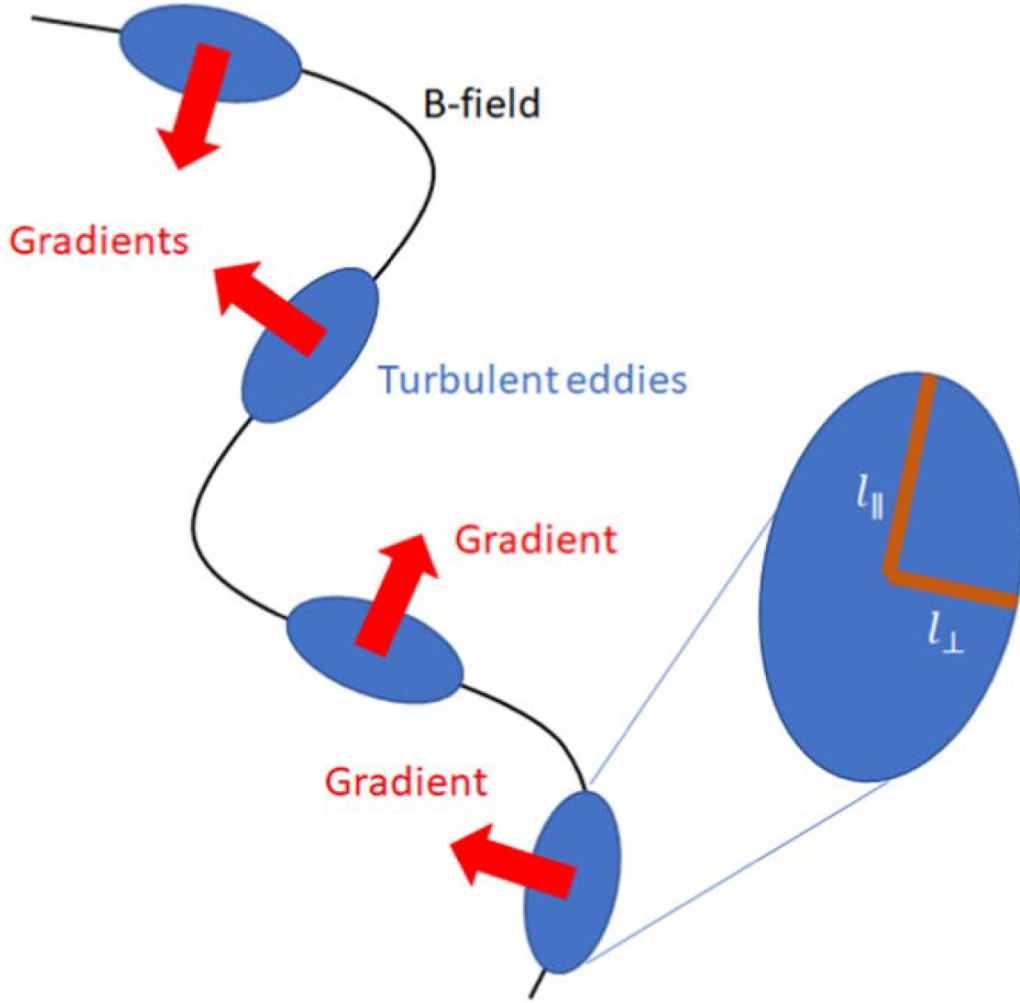


Figure 2.1: Schematic diagram adopted from Lazarian et al. (2018) showing the turbulence eddies in the dynamically important magnetic field, the elongations of the turbulence eddies are align with the magnetic field direction. Notice that the anisotropy is related to the local magnetic field direction.

minor axis is orthogonal to this. Thus spatial gradients in velocity are expected to be largest in directions perpendicular to the B -field. This opens up the possibility of kinematic methods for inferring magnetic field orientation (see, e.g., Burkhart, 2021, for a review).

2.2 Evolutionary stages

2.2.1 Infrared dark clouds (IRDCs)

Massive stars and star clusters are thought to form from dense molecular clumps within giant molecular clouds (GMCs). In their early stages, these clumps can appear as infrared dark clouds (IRDCs), i.e., IR shadows against the diffuse Galactic mid-IR background (Perault et al., 1996; Egan et al., 1998; Simon et al., 2006). Figure 2.2

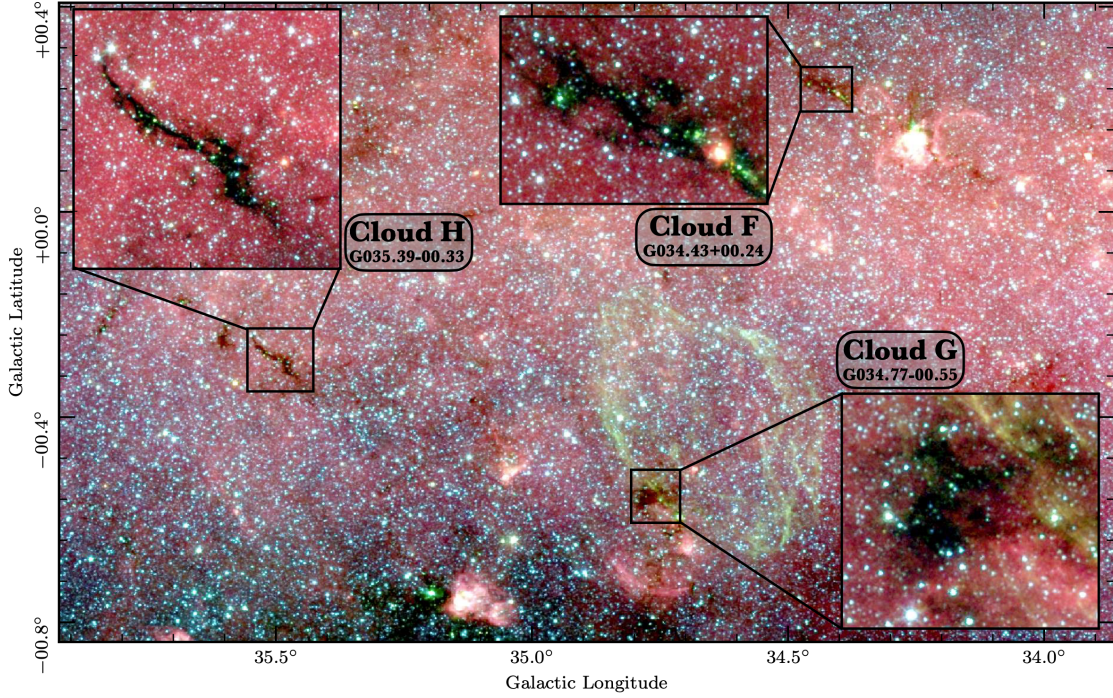


Figure 2.2: (From Barnes et al., 2021): three-color image of part of the Galactic plane which highlights several infrared dark clouds (IRDCs). In this image, red is $8\ \mu\text{m}$, green is $5.8\ \mu\text{m}$ and blue is $4.5\ \mu\text{m}$ emission from the Spitzer GLIMPSE survey (Carey et al., 2009). The three IRDCs are Clouds F ($G034.43+0.24$), G ($G034.77-0.55$), and H ($G035.39-0.33$) following the naming in Butler & Tan (2009). The inset panels show zoom-ins of these IRDCs.

shows three well studied IRDCs exhibited as such dark silhouettes in front of the mid-infrared Galactic emission as observed with the Spitzer space telescope (Barnes et al., 2021).

Many IRDCs appear to be globally filamentary or to contain filamentary sub-structures (e.g., Kainulainen and Tan, 2013). Such filaments may arise due to local turbulent shock compression within GMCs, collisions between GMCs (e.g., Wu et al., 2018), compression in feedback shells (e.g. Cosentino et al., 2020), collision of feedback shells with each other (e.g. Inutsuka et al., 2015), magnetically regulated collapse (e.g. Li et al., 2014), or some combination of these processes.

Numerous of studies have been carried out to characterize the physical conditions of IRDCs (e.g., Rathborne et al., 2006; Butler and Tan, 2009, 2012; Kainulainen and Tan, 2013; Hernandez and Tan, 2015; Sokolov et al., 2017). Figure 2.3 shows the dust extinction map of Cloud H ($G035.39-00.33$) from Kainulainen and Tan (2013). The extinction map is constructed by combining mid-infrared and near infrared extinction data. The high extinction up to at least $A_V \sim 100$ mag indicates high column densities ($N_H \sim 1.87 \times 10^{23}\ \text{cm}^{-2}$ assuming a conversion factor of $N_H/A_V = 1.87 \times 10^{21}\ (\text{cm}^{-2}/\text{mag})$ (Bohlin et al., 1978) Based on such column density maps, estimates of the volume densities can be made, with values of $n_H \sim 10^3\text{--}10^6\ \text{cm}^{-3}$ inferred for structures with masses in the range $\sim 10^5$ down to $10\ M_\odot$ (Butler and Tan, 2012). Temperatures in IRDCs have been measured from studies of NH_3 emission

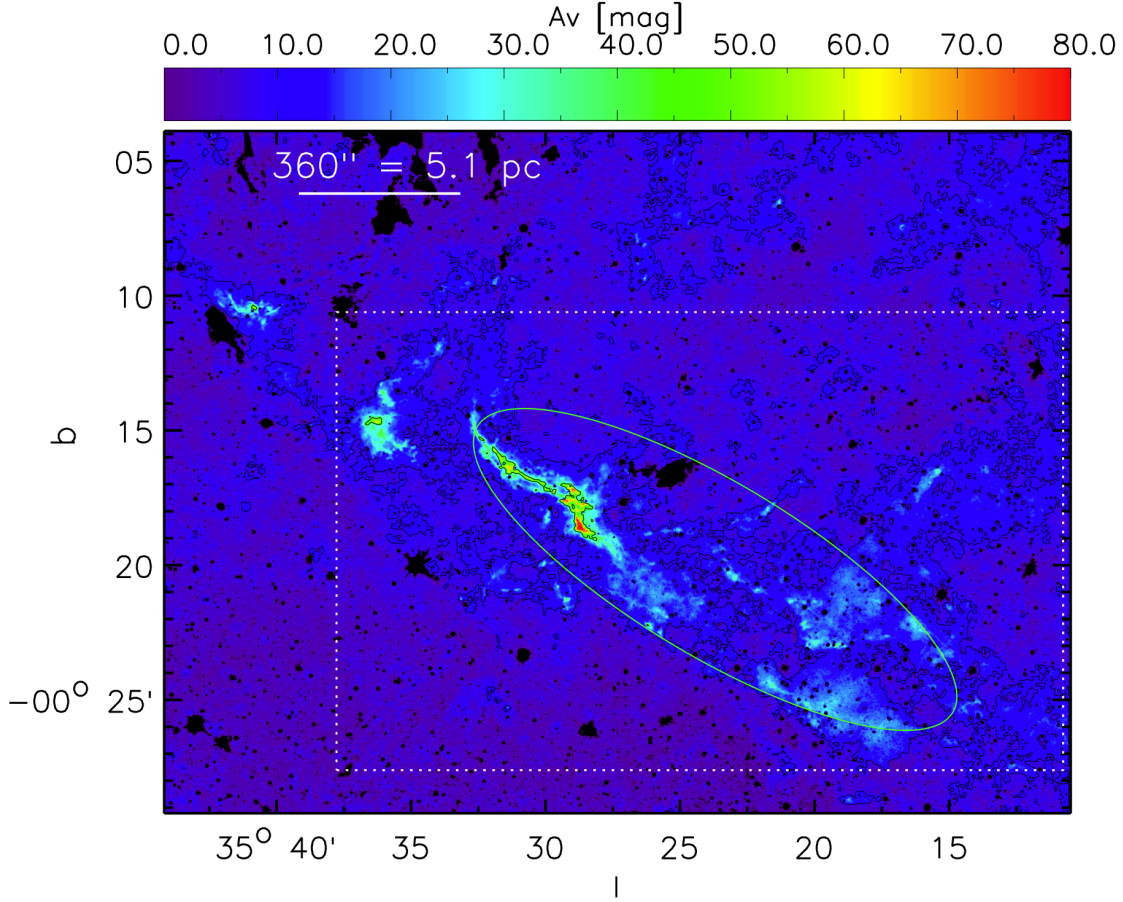


Figure 2.3: Dust extinction map of Cloud H (G35.39-00.33) constructed from mid-infrared and near-infrared data (Kainulainen and Tan, 2013).

(Pillai et al., 2015) and from FIR dust SEDs (Lim et al., 2016), with values of ~ 15 K inferred. Pillai et al. (2015) (see also Soam et al., 2019; Tang et al., 2019) mapped the plane of sky magnetic fields using polarized dust continuum emission toward two IRDCs and, via the DCF method, inferred the presence of dynamically strong, \sim mG B -fields and sub-Alfvénic turbulence $M_A \sim 0.5$.

On the astrochemical side, as IRDCs are cold and dense, high levels of CO freeze-out (depletion) have been detected. The CO depletion factor (f_D) is defined as the ratio between an abundance of CO assuming all C is in the form of CO in the gas phase and the actual CO gas phase abundance. Values of $f_D \sim 3$ to 10 have been measured (Hernandez et al., 2011; Jiménez-Serra et al., 2014; Entekhabi et al., 2021).

2.2.2 Fragmentation of IRDCs into Prestellar Cores

The previous section summarized the main observed environmental properties of IRDCs. To form massive stars and star clusters, requires fragmentation and collapse within IRDCs. How such fragmentation proceeds is expected to influence the properties of the resulting stars and star clusters. For example, massive star formation theories involve different levels of fragmentation. In the Turbulent Core Accretion model (McKee and Tan, 2003), some rare cases of massive prestellar cores with limited fragmentation results. These objects contain many thermal Jeans masses, i.e., the mass that can be supported against gravity purely by thermal pressure, so their fragmentation must be prevented by some combination of turbulent and magnetic pressure. On the other hand, the Competitive Accretion model (Bonnell et al., 2001) invokes high levels of fragmentation to thermal Jeans scale.

The core accretion model (see Figure 2.4) proposes that massive stars form by a process that is a scaled-up version of the low-mass star formation model (Shu et al., 1987), thus the formation of a massive star happens from material localized in a well-defined region, i.e., the dense core. However, the core will be massive and is partially supported by turbulence and magnetic fields (e.g., Butler and Tan, 2012; Tan et al., 2014) to prevent its fragmentation. Nevertheless, the model also suggests a more disordered collapse of the dense core due to its turbulent nature, perhaps including significant accretion via over-dense filaments and other sub-structures, e.g., as seen in magnetohydrodynamical (MHD) simulations of such structures (Seifried et al., 2012; Myers et al., 2013; Hsu et al., 2021). On the other hand, in the Competitive Accretion model (see Figure 2.4), stars chaotically gain their mass via the global collapse of the clump without passing through the massive pre-stellar core phase. The prediction of this model is that massive stars always form in clustered environments, i.e., surrounded by many lower-mass protostars.

Several observational features can provide important information to help distinguish between core and competitive accretion: (1) Core mass function; (2) Identification of massive dense cores and levels of fragmentation; (3) Existence of massive protostars in relative isolated regions.

(1) Core mass function: A characteristic feature of core accretion models is a more direct linkage of the pre-stellar core mass function (CMF) and the stellar initial mass function (IMF). Several observational studies have found CMF shapes that are similar to that of the IMF (Alves et al., 2007; André et al., 2010; Könyves et al., 2015; Cheng et al., 2018). On the other hand, in the competitive accretion framework, there is no correlation between the CMF and the IMF as the accretion involve randomly fed ambient gas materials from the clump or the parent cloud (e.g. Padoan et al., 2020).

(2) Identification of massive pre-stellar cores Another important observational features to disentangle between the two scenarios is to look for massive dense core, especially pre-stellar cores. For instance, some CMF studies (e.g. Motte et al., 2018; Liu et al., 2018; O’Neill et al., 2021) have found relatively shallow CMF indices, suggesting the existence of massive dense cores. Furthermore, ALMA observations toward IRDC G28.37+0.07 by Tan et al. (2013) identified two massive dense prestellar core candidates with masses as high as $60 M_{\odot}$. Csengeri et al. (2017)

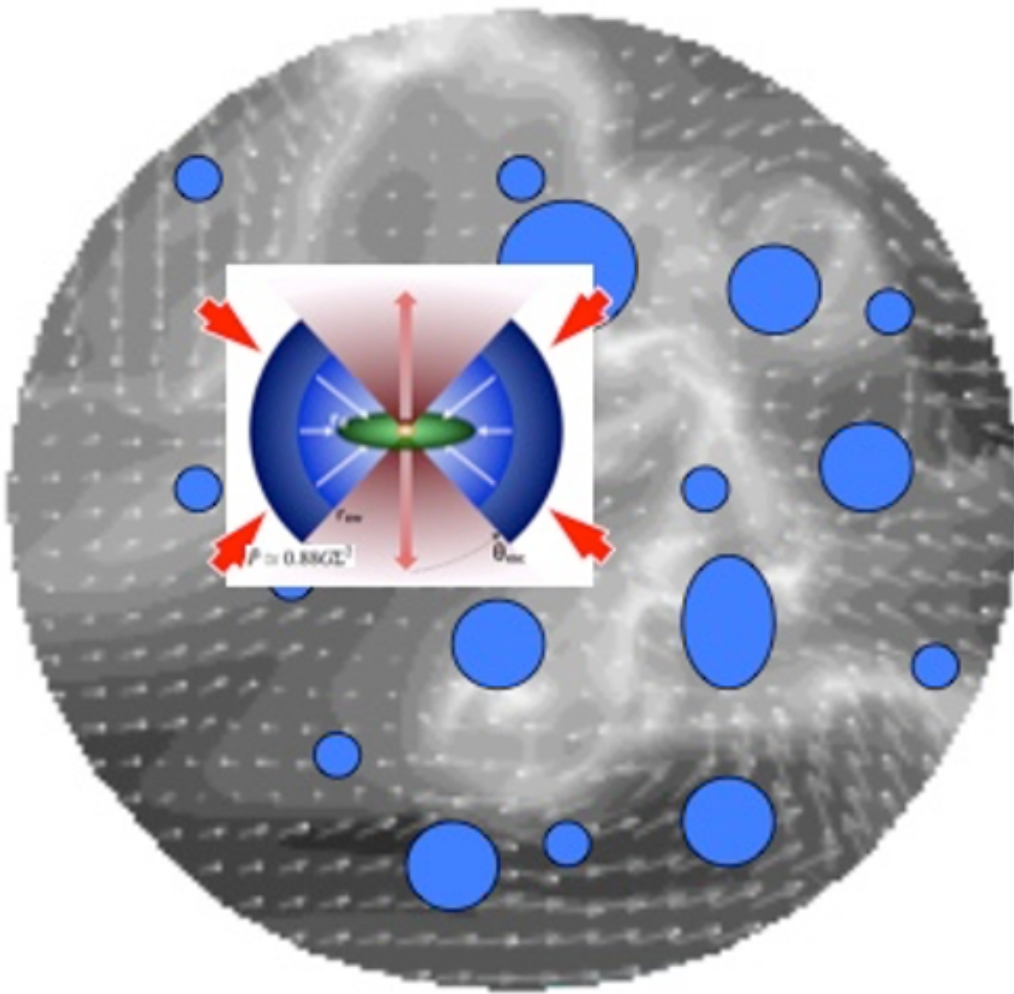


Figure 2.4: A schematic diagram showing the core accretion model. (image credit: Jonathan Tan).

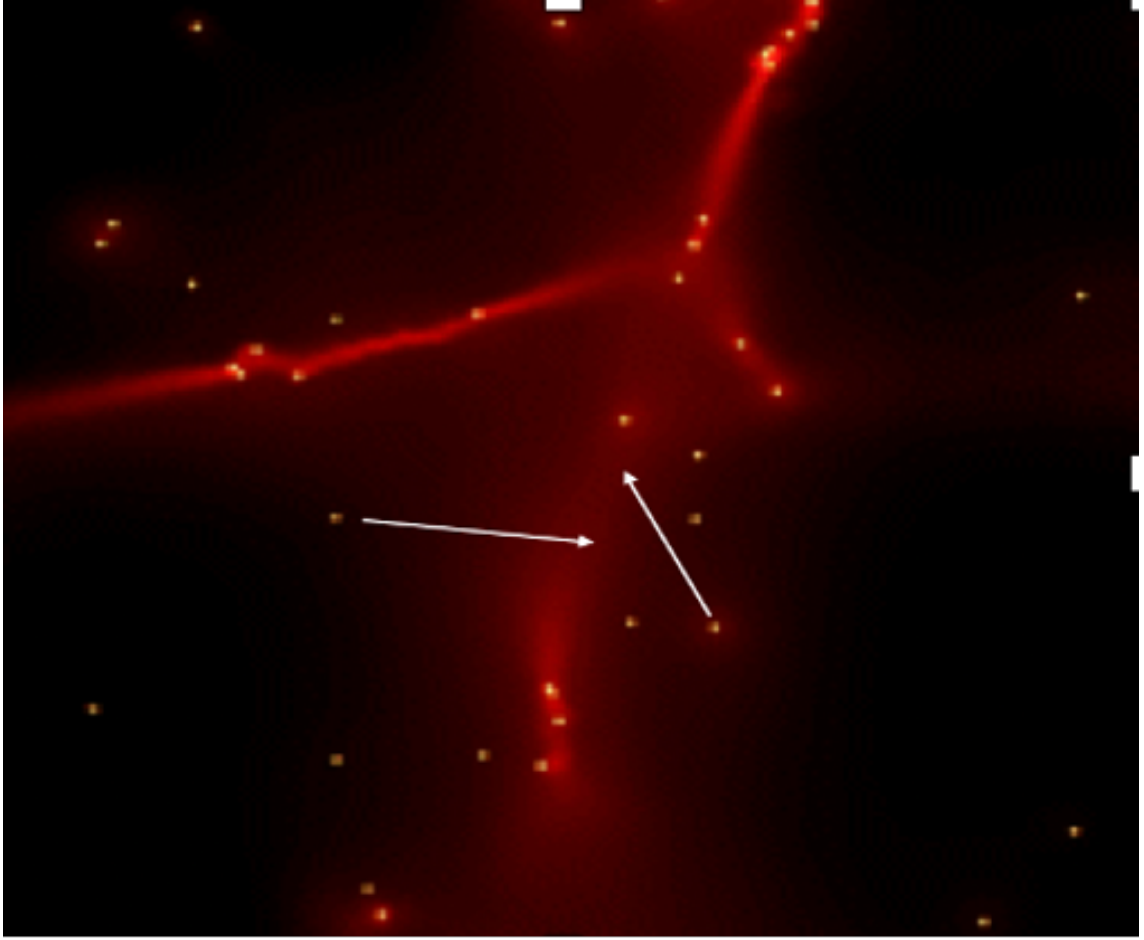


Figure 2.5: A schematic diagram of competitive accretion model (image credit: Bonnell et al. (2001)).

surveyed 35 sources with ALMA and found that most of them show limited fragmentation, with at most 3 cores per clump. On the other hand, some observations find higher levels of fragmentation: e.g., Cyganowski et al. (2017) studied the high-mass star-forming region G11.92-0.61 finding that the three massive protostars in the region are surrounded by at least 16 lower mass protostellar sources within a region about 0.3 pc in radius; Sanhueza et al. (2019) studied 12 IRDCs clumps and revealed a higher level of fragmentation with a large population of low-mass cores with sizes smaller than 0.1 pc, but no high-mass counterparts.

(3) Massive protostars in isolated environments: A main observational prediction of competitive accretion models is that massive stars must form in crowded environments. Hence, identification of massive stars forming in relative isolated environments would provides evidence in favor of core accretion, at least in these regions. G28.2-0.05, the massive protostellar system analyzed in this thesis provides a case study for this type of investigation.

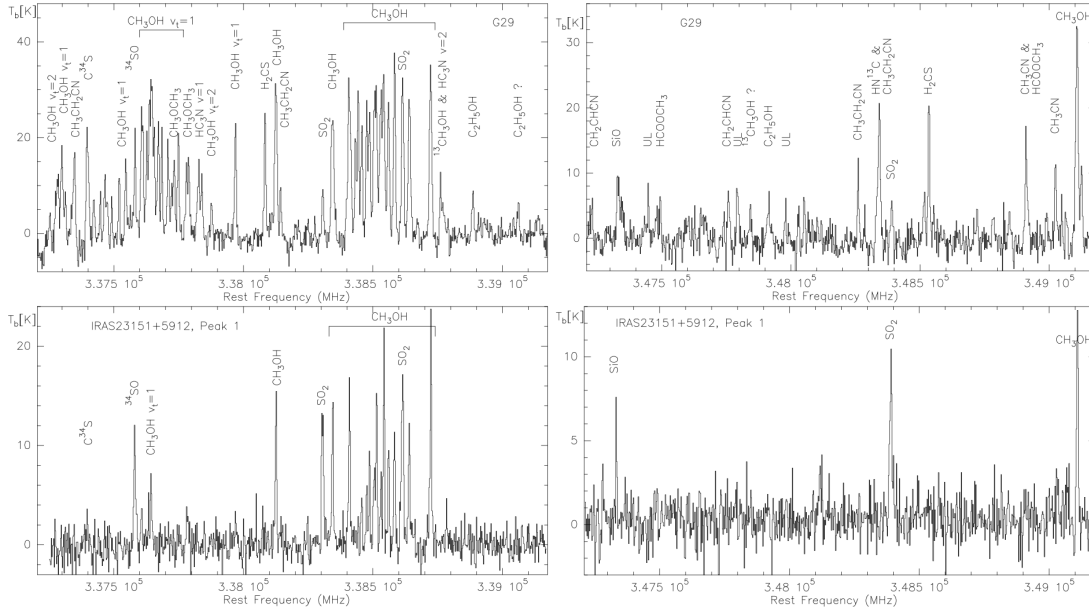


Figure 2.6: SMA spectra adopted from Beuther et al. (2007a,b) toward two massive star-forming regions (Top: G29.96; Bottom: IRAS 23151+5912). The spectra show forests of simple and complex species.

2.2.3 Massive protostellar cores / hot molecular cores

Massive protostars, being sources of high luminosity and surrounded by large quantities of dense gas, lead to astrochemically rich conditions, observed as ‘hot molecular cores’ (HMCs). These cores are characterized by being compact (≤ 0.1 pc), warm ($T > 100$ K), and dense ($n_{\text{H}} > 10^6 \text{ cm}^{-3}$) (e.g., van der Tak, 2004; Beuther, 2007; Tan et al., 2014). Examples of a radio spectrum toward two HMCs are presented in Figure 2.6 (Beuther et al., 2007a,b). In particular, many complex organic molecules (COMs) have been identified in such spectra, including species that are building blocks of prebiotic molecules, such as amino acids and proteins (e.g., Chakrabarti and Chakrabarti, 2000; Garrod, 2013).

Following the cold IRDC and pre-stellar core phases, molecules are mostly frozen on to dust grains. The HMC phase involves these species being thermally desorbed into the gas phase. Chemical processing can occur both in the ices before desorption and in the gas phase. The massive protostar G28.2-0.05 that is studied in this thesis has been revealed to be one of the most chemically rich sources (Gorai et al. in-prep). The physical characterization of the source we have carried out will be important for the astrochemical modeling of this source.



Figure 2.7: Four color image of the HII region Sh2-284 as seen by WISE. Blue and cyan corresponds to emission at 3.4 and 4.6 μm , while green and red show emission at 12 and 22 μm , respectively. Credit: NASA/JPL-Caltech/UC

2.2.4 Ionizing feedback as traced by HII regions

HII regions are the locations where H is ionised (Hoare et al., 2007). Young massive stars produce high quantities of EUV photons that efficiently photoionize the gas around them. Gas may also be ionized by strong shocks, e.g., driven by protostellar outflows and stellar winds. Photoionized gas reaches temperatures of about 10,000 K and so is overpressured compared to surrounding molecular cloud gas (Hoare et al., 2007; Churchwell, 2002). Thus HII regions begin to expand into their surroundings and this may be a crucial feedback process that destroys molecular clouds (e.g. Kirsanova et al., 2008; Devaraj et al., 2021).

As an example, Figure 2.7 presents an image of the HII region Sh2-284, which is powered by photoionization from already formed massive stars. These HII regions are among the brightest objects in the mid infrared to radio wavelengths (Hoare et al., 2007; Churchwell, 2002). Owing to such high luminosity, HII regions are targeted by observers as the ‘signpost’ for recently formed massive stars. To date, over 2,000 HII regions have been detected across the Galaxy, including using MIR survey data, followed up by studies of cm radio continuum free-free emission (Wenger et al., 2021).

During the earlier protostellar phase, HII regions are smaller and indeed are characterized via their size, i.e., Hyper-Compact (HC) HII regions (< 0.01 pc) and Ultra-Compact (UC) HII regions (Churchwell, 2002). Large samples of UC HII regions

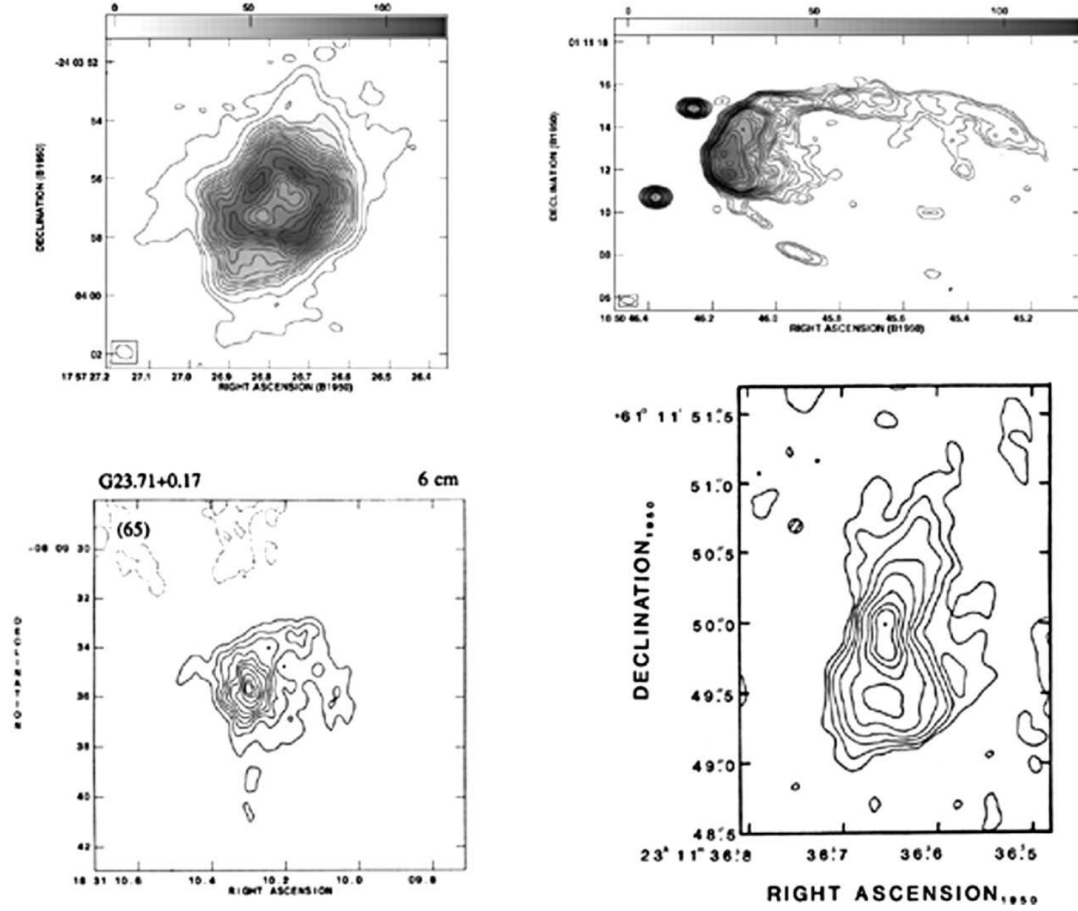


Figure 2.8: Examples of UC-HII regions with different morphologies: Shell-like (top left), Cometary (top right), Core-halo (bottom left), Bipolar (bottom right). Figure is adapted from Rodríguez (2005).

were first characterized by Wood and Churchwell (1989) based on the IRAS data. Some examples of UC-HII regions in radio wavelengths are presented in Figure 2.8, which display different basic morphology. For instance, G28.2-0.05, the source analysed in this project, is a shell-like HC-HII region (Sewilo et al., 2008). The different morphology could potentially be important in understanding the evolution of the massive star forming environments, as it retains memories on the information before ionization (Churchwell, 2002).

The radio spectral energy distribution (SED) of an HII region typically has a shape presented in Figure 2.9. The spectral break corresponds to the frequency when optical depth $\tau \sim 1$ Condon and Ransom (2016). At frequencies lower than the break, where $\tau > 1$, the SED follows a black body with spectral index $\alpha_\nu \simeq 2$, where $S_\nu \propto \nu^{\alpha_\nu}$. On the optically thin side, the optically thin free-free emission results in a characteristic spectral index of $\alpha_\nu \simeq -0.1$ Condon and Ransom (2016). However, the radio SED of an HII region can involve a more intermediate power law index over a broader range of frequencies if there is an underlying density structure in the HII region, e.g., as in that of a stellar wind or protostellar outflow (e.g. Tanaka et al., 2017). The radio emission from HCHII regions can be a crucial diagnostic to help

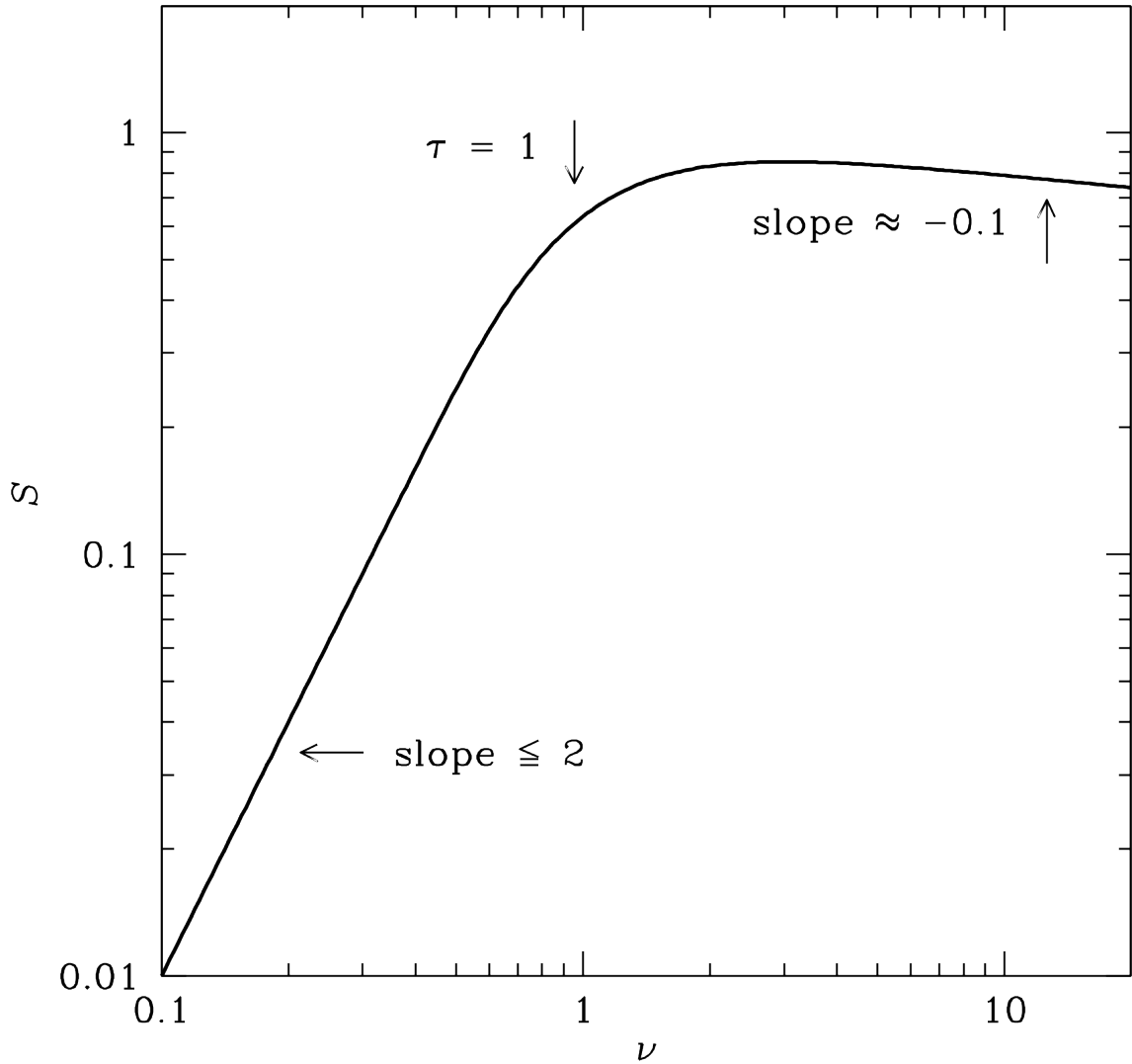


Figure 2.9: The typical shape of the spectral energy distribution of HII regions. The slope at frequency below the spectral break, indicated at the frequency when $\tau = 1$ is optically thick and follow a black body. The drop follows an index of ~ 2 assuming a cylindrical geometry. For the frequency higher than the spectral break, the slope index is -1 , which is correlated with the electron density. Figure from Condon and Ransom (2016).

pinpoint the location of massive protostars that are just starting to ionize their local environments.

2.3 A short note on interferometry

Much of the data analyzed in this thesis has been gathered by the ALMA interferometer. Radio interferometry is needed to achieve the high angular resolution required to probe the scales of distant massive protostars. Taking the source G28.2-0.05 as an example, it has a prominent mm continuum structure on scales of $0.7''$. To have 5 sampling elements across the source, requires an angular resolution of $0.14''$. ALMA

in a configuration with intermediate or long antenna baselines can easily achieve such resolutions at 1.3 mm wavelengths (see Table 2.1).

While interferometry opens up a window to allow such high resolution studies, there are still some caveats. An important problem is the incomplete sampling of the visibility plane ($u - v$ space). The regions sampled are related to the baseline differences between antenna pairs, and there is always a minimum baseline limit between such pairs. Therefore, extended emission beyond some scale will be filtered out, i.e., the maximum recoverable scale (MRS). To recover this extended emission, single dish observations are needed, which can then be combined with the interferometric data.

ALMA is located in the Atacama desert at an elevation of about 5200 m. The astronomical interferometer is composed of 66 antennas (forming the 12 m main array and also the Atacama Compact Array [ACA]). By dynamically moving the antenna to form different combinations, a wide ranges of angular resolutions ¹ as high about a 30 mas scale at 1.3 mm can be achieved. In Paper I, the source was observed by ALMA main 12m array at Band 6 (~ 1.3 mm) with three different array configurations representing different baseline distances and thus various angular resolutions and MRS levels. The corresponding details are summarized in following table.

¹<https://almascience.eso.org/proposing/proposers-guide>

Table 2.1: Summary of ALMA observations toward G28.2-0.05

Start of Obs.	Obs. time (min.)	Config.	Antennas used	Baseline Lengths (m)	Averaged Interval (sec.)	MRS (")	Beam size (")
2016 April 24 07:44:13.2	4.17	C	41	14.7 - 376.9	6.05	11.0	0.735 × 0.813
2016 Sept 11 02:45:50.2	16.2	I	37	47.9 - 1396	6.05	3.40	0.201 × 0.217
2017 Sept 30 01:53:01.1	34.5		41				
2017 Nov 1 00:15:20.2	34.8	E	49	346.5 - 9743	2.02	0.340	0.026 × 0.048
2017 Nov 5 23:00:02.4	61.1		47				

Chapter 3

Paper summary and future works

3.1 Paper summary

In the appended paper, we present a detailed characterization of the physical properties of the massive protostellar system G28.2-0.05. The study was motivated by the apparent isolated nature of the source as a means to more stringently test massive star formation theories. The data was based on ALMA Band 6 observations. The data was reduced by the pipeline and manual reduction was performed on the most extended configuration data. All imaging and self-calibrations were performed with CASA (ver. 5.6.1-8)(McMullin et al., 2007).

We first inspected the overall 1.3 mm continuum morphology and detected a ring-like structure at a scale of about 2,000 au. A similar structure has been seen by the VLA at 1.3 cm, suggesting it traces ionized gas, i.e., from a H_C HII region. We characterized the radio SED, including with an in-band SED analysis, to estimate the contribution of dust emission to the 1.3 mm flux. The dust appears to be concentrated on one side of the ring at the main mm continuum peak, which we identify as the likely location of the massive protostar (see also below). The regions just beyond the ionized ring, also appear to be dominated by dust emission.

We examine line emission in the ALMA data. The H30 α recombination line also traces ionized gas. It shows a strong line of sight velocity gradient at the location of the main mm continuum peak, which is further evidence that this is the location of the massive protostar. A dynamical mass estimate is made of the source from these data. Several hot core molecular species are also identified, with emission in the vicinity of the mm continuum peak. However, a more extensive study of the astrochemistry of the source is deferred for a follow-up paper (Gorai et al., in prep.). Finally, high velocity CO(2-1) emission is detected tracing a wide-angle bipolar outflow that is driven from the region and extends to large scales.

3.2 Future works

Studying more massive protostars in a greater range of environments will allow further constraints on massive star formation theories. The SOFIA Massive (SOMA)

Star Formation survey, which has observed a large sample (> 50) massive protostars in different environments and evolutionary stages provides a prime data base for follow-up studies with ALMA and applying methods similar to those developed here.

Furthermore, additional large scale molecular line surveys, gas kinematics, and magnetic field properties of IRDCs (Gorai et al. 2022 in-prep, Law et al. 2022 in-prep, see next chapter) are essential to connect the larger-scale properties in the parental filament and the IRDCs to the local environment, thus forming a multi-scale diagnostic analyses on the massive star and star cluster mechanisms.

Chapter 4

Turbulence and magnetic fields in IRDC G38.9-0.74

4.1 Introduction

The roles and relative importance of self-gravity, turbulence, magnetic fields and feedback in massive star and star cluster formation remain uncertain (e.g., Tan et al., 2014; Rosen et al., 2020). In particular, it is challenging to measure the properties of magnetic fields (see §1), with most practical methods of inferring B -field morphology and strength in star-forming molecular clouds relying on indirect methods, especially via mapping of polarized emission that is assumed to arise from the alignment of nonspherical dust grains with magnetic field directions (e.g., Li et al., 2014). Significant advances in this kind of observational data have occurred recently with the results of PLANCK, BLAST-POL, JCMT-POL2, and SOFIA-HAWC+. Another relatively novel method is to try and infer the effect of magnetic fields on turbulent motions (see §1). Such methods have typically been calibrated against idealized simulations of turbulence, but there have been relatively few studies that test their results against independent observational measures of B -fields, such as from polarizaration. This comparison is the primary goal of this project, with the target to be studied an example Infrared Dark Cloud (IRDC) that has been observed with high spatial and kinematic resolution in CO lines and has had its polarization morphology mapped in the FIR.

IRDCs were identified via their high opacity at mid infrared (MIR) wavelengths (e.g., Rathborne et al., 2006; Barnes et al., 2021). These massive dense clouds are known to be the progenitors of massive stars and star clusters (e.g., Butler and Tan, 2012; Kainulainen and Tan, 2013; Hernandez and Tan, 2015; Sokolov et al., 2017). Direct observations of the magnetic field strengths in IRDCs are very challenging, e.g., because molecules normally used for Zeeman measurements, like CN, are frozen out onto dust grains. Some constraints on B -field morphology and strength have been derived based on maps of polarized dust emission and by utilizing the Chandrasekhar & Fermi method (Chandrasekhar and Fermi, 1953). For example, Pillai et al. (2015) and Soam et al. (2019) have found relatively ordered degrees of polarization and inferred that dynamically important magnetic fields are presented

in IRDCs. However, there are significant uncertainties with this method of B -field estimation, including its reliance on the uncertain physics of dust grain alignment with B -fields. Alternative methods are thus needed to compliment as well as to provide independent information on the magnetic field properties.

Models and simulations of interstellar turbulence (e.g., Goldreich and Sridhar, 1995) allow predictions to be made for the influence of magnetic fields on velocity anisotropies and how these may be inferred from analysis of spectral line cubes of molecular lines, especially CO. have made ways to various techniques to infer magnetic field orientations and other properties using the spectral line cube of molecular lines (see, e.g., Burkhart, 2021, for a review). In particular, the Velocity Channel Gradient (VCG) technique has been shown to capable to reveal magnetic field morphology and other properties (e.g., Yuen and Lazarian, 2017; Lazarian et al., 2018).

Observationally, the VCG method has been applied to a few low-mass star-forming regions (e.g., Hu et al., 2019; Heyer et al., 2020) and in the massive star forming region DR21 (Alina et al., 2020). However, it is unclear how reliable VCG may be in regions with strong outflow feedback from star formation. Thus additional observational studies are needed to test VCG analysis, ideally in early-stage clouds, like IRDCs, that may be relatively free of feedback.

The IRDC G38.9-0.74 (kinematic distance of 2.7 kpc) is one (Cloud I) of the ten clouds (A-J) in the sample of Butler and Tan (2009, 2012); Kainulainen and Tan (2013), who produced high resolution MIR-based extinction maps of the regions. Hernandez and Tan (2015) studied the kinematics and dynamics of these clouds, including Cloud I, using the relatively low resolution (about $46''$) $^{13}\text{CO}(1-0)$ data of the Galactic Ring Survey (GRS) (Jackson et al. 2006). The study by Cosentino et al. (2020) detected a wide spread of SiO morphology over Cloud I, which indicates a potential shock interaction with the nearby HII regions N74 and N75. Two cores have been identified toward the cloud, in which one has found with signatures of molecular outflow and in-fall signature based on single dish SiO studies, while the second core is more quiescent. The existence of both kinds of environment provides an ideal test-bed to for the VCG techniques.

Here, using IRDC G38.9-0.74 (Cloud I) as a test case, we present preliminary results from a project to perform the first comprehensive study of the magnetic field morphologies and properties of IRDCs utilizing the high-resolution (about $6''$) $^{13}\text{CO}(1-0)$ Green Bank Telescope (GBT)-Argus observations, complimented with SOFIA-HAWC+ dust continuum polarimetry data.

4.2 Methods

4.2.1 Velocity Channel Gradient (VCG)

The VCG method using spectral line cube data is described in detail by Yuen and Lazarian (e.g., 2017); Lazarian et al. (e.g., 2018); Heyer et al. (e.g., 2020). In brief, the method applies a simple Sobel kernel to compute the gradient in intensities of a given “thin” channel map. The condition of being “thin” is simply that the velocity

range of the channel map be smaller than the velocity dispersion of the cloud. Then the direction and magnitude of the gradient in intensity, i.e., brightness temperature, T , are described by

$$\nabla T_k(x, y, v) = \left[\left(\frac{\partial T_k(x, y, v)}{\partial x} \right)^2 + \left(\frac{\partial T_k(x, y, v)}{\partial y} \right)^2 \right]^{1/2}, \quad (4.1)$$

$$\Psi_{G,k}(x, y, v) = \arctan \left[\frac{\partial T_k(x, y, v)}{\partial x} / \frac{\partial T_k(x, y, v)}{\partial y} \right]. \quad (4.2)$$

In practice, the original map is dissected into multiple blocks which the mean of gradient in each block is computed. Here we take the block size to be the same as the three beam resolutions, which correspond to $18''$ by $18''$. This size is also equivalent to the SOFIA beam resolution.

4.3 Observational Data

4.3.1 GBT-ARGUS ^{13}CO data

Argus (Sieth et al., 2014) is a 16-element heterodyne ‘radio camera’ operating with the GBT in the range of 85-116 GHz. The 16 heterodyne pixel receivers of Argus are mounted in a 4×4 layout and have a beam separation of $30.4''$ in both the elevation and cross-elevation directions.

Simultaneous mapping of the $^{13}\text{CO}(1-0)$ and $\text{C}^{18}\text{O}(1-0)$ emission from the target IRDC was performed using the GBT Argus on the 27 April 2021. The observations utilised a ‘fast-mapping’ method in which the heterodyne pixel receivers are scanned across the sky in rows of Galactic longitude, separated by $5.58''$ ($0.8 \times$ the beam size). This might be expected to undersample the plane of the sky in comparison with Nyquist sampling, in which a separation of $<0.5 \times$ the beam size is required. However, the effects of sky rotation in relation to the scan direction, in addition to that fact that any given point in the sky is observed by multiple beams, allows for a relaxation of this requirement, without loss of information.

The data were reduced using the GBTIDL package, with calibration achieved through observations of the Argus ‘Vane’, essentially a warm load placed in the beam of the receiver. Atmospheric opacity estimates were taken from the forecast values obtained from the CLEO¹ application, which are the average of the values from three surrounding local sites.

After baseline fitting and removal was performed on spectra from each ARGUS feed, these data were then gridded using the GBO tool ‘gibtgridder’ with a Gaussian beam assumption and a pixel size of $2''$. The resulting cube was then subjected to further iterative baseline fitting and removal in order to equalize background noise levels.

¹<https://www.gb.nrao.edu/rmaddale/GBT/CLEOManual/index.html>

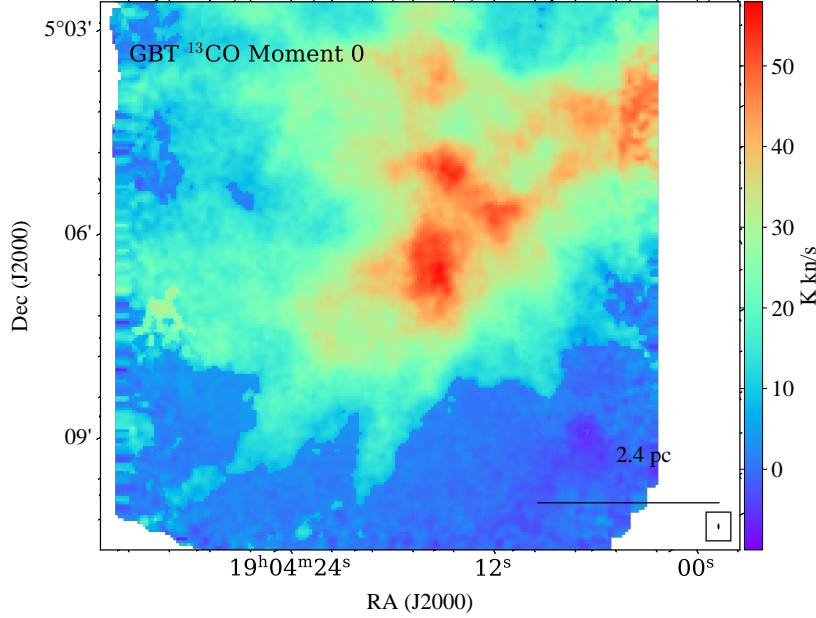


Figure 4.1: $^{13}\text{CO}(1-0)$ Moment 0 map of IRDC G38.9-0.74 integrated from $v_{\text{lsr}} = 32$ to 50 km s^{-1} .

4.3.2 SOFIA-HAWC+ polarized dust emission data

The *SOFIA*-HAWC+ observation was carried out on 8 Sept. 2021 (Proj. ID 09_0104, PI: Tan) in polarization OFTMAP mode to map the large-scale dust continuum and polarization at $215 \mu\text{m}$ (band E). The angular resolution is $18''$. The mapped region is $6.2' \times 4.2'$ centered at R.A.: $19^{\text{h}}04^{\text{m}}10.00^{\text{s}}$, Dec.: $+05^{\circ}06^{\text{m}}20.0^{\text{s}}$. The science ready data were delivered after pipeline reductions performed by the *SOFIA* science staff.

4.4 Results

4.4.1 CO Kinematics

The overall $^{13}\text{CO}(1-0)$ integrated intensity morphology is presented in Figure 4.1. It shows peak intensities of about 50 K km/s , concentrated in several main clumps that are surrounded by a more extended structure. We also inspect the velocity spectrum (Figure 4.2) to infer the systemic velocity of the cloud of 41.2 km s^{-1} . We notice that this velocity is consistent with the 41.6 km s^{-1} that was reported in Rathborne et al. (2006).

4.4.2 Polarized Dust Emission

Figure 4.3 presents the Stokes I maps toward the G38.9-0.74 region. The overlaid HAWC+ inferred magnetic field directions shows ordered magnetic field morphology

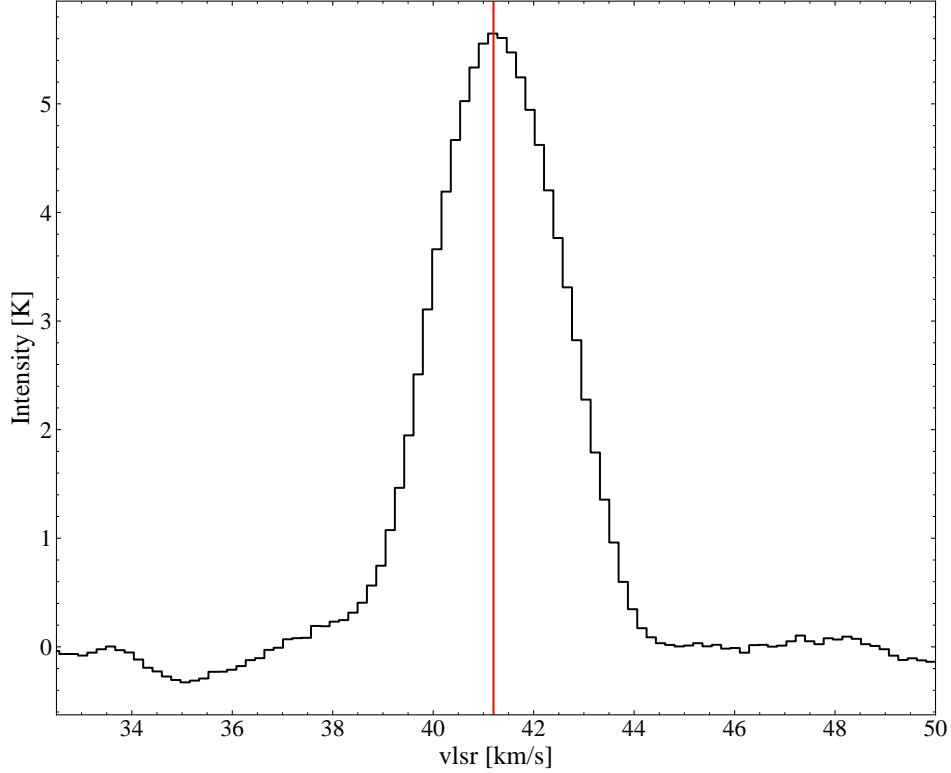


Figure 4.2: Averaged $^{13}\text{CO}(1-0)$ spectrum of G38.9-0.74. The red line shows the inferred systemic velocity of 41.2 km s^{-1} .

around the cloud. We only select polarization vectors that have $I/\sigma I \geq 50$, $\text{SNR}(\text{P}) \geq 2$, $\text{P}(\%) \leq 50$, and the uncertainty of the polarization angle $\delta\theta \leq 30$. However, we notice that most of the vectors seems to be off the main filament but detecting the nearby HII regions. None the less, as the GBT-ARGUS data cover the same region, thus allow us to compare the magnetic field morphology.

4.4.3 B-field Analysis

For the CO data, we carry out the VCG analysis on a thin channel near the peak of the spectrum. The results are shown in Figure 4.5. A first inspection of the overall morphology suggests no particular anisotropy in the direction.

Next, we show the HAWC+ inferred B-field orientations overlaid on the CO map of the IRDC. The map shows the presence of ordered polarization vectors detected toward the relatively bright regions, with much of the inferred B-field vectors in the North to South direction.

Thus, from a first preliminary analysis of these data, we do not see clear evidence for agreement between the VCG and dust polarization methods for inferring B-field

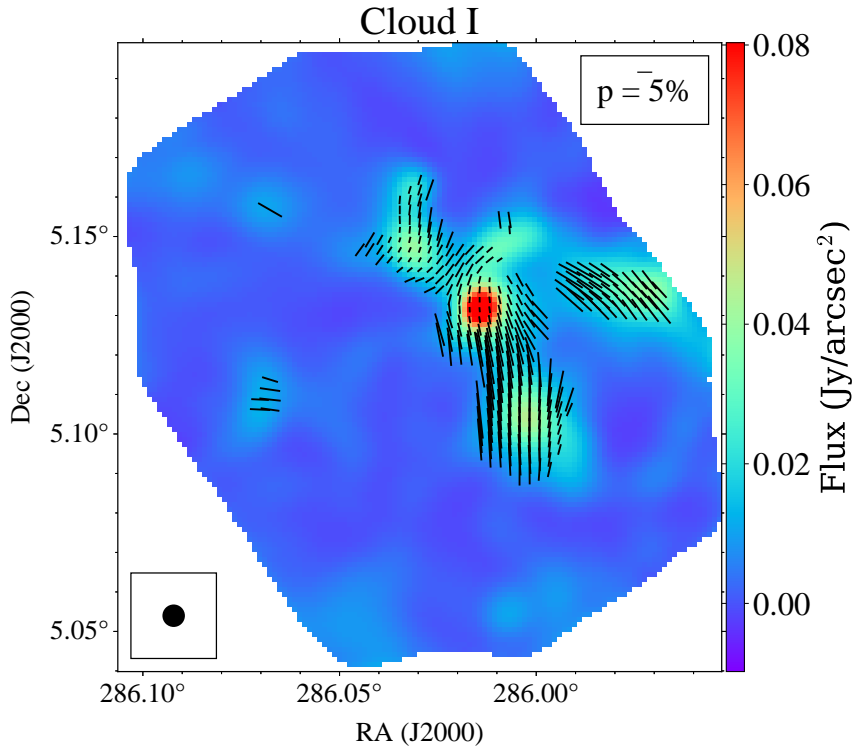


Figure 4.3: SOFIA 215 μ m Stokes I intensity map overlaid with the magnetic field direction.

orientation. Further work is needed to examine the robustness of this conclusion.

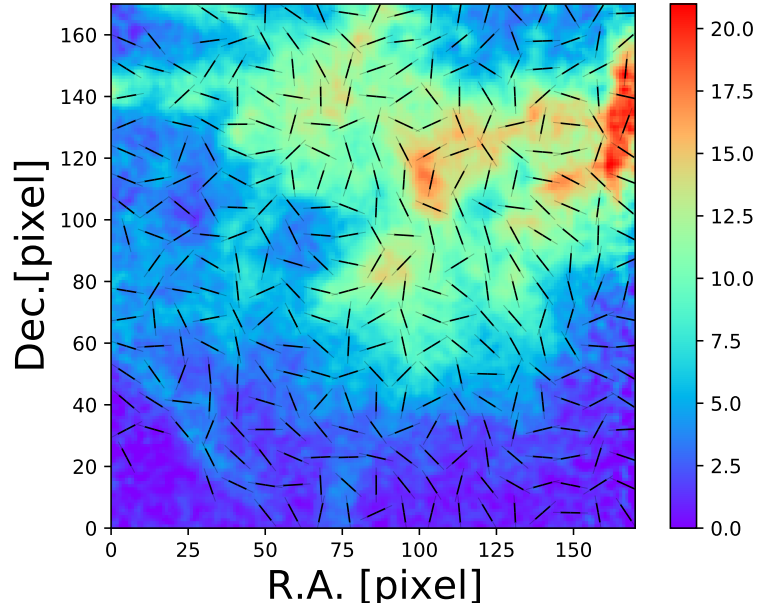


Figure 4.4: Top: $^{13}\text{CO}(1-0)$ Moment 0 map of IRDC G38.9-0.74 overlaid with the the HAWC+ $215\mu\text{m}$ Stoke I intensity contours (silver) and the 8 intensity contours (black). The inferred magnetic field (by rotating the polarization angle with 90 degrees) is overlaid as vectors. The SOFIA beam size is presented in the bottom left corner with FWHM of $18''$. We only select polarization vectors that have $I/\sigma I \geq 50$, $\text{SNR}(P) \geq 2$, $P(\%) \leq 50$, and the uncertainty of the polarization angle $\delta\theta \leq 30$. Bottom: plane of sky magnetic field morphology inferred from the $^{13}\text{CO}(1-0)$ spectral cube using the velocity gradient technique. The background presents the moment 0 map toward the velocity channel at the systemic velocity (peak of the spectrum).

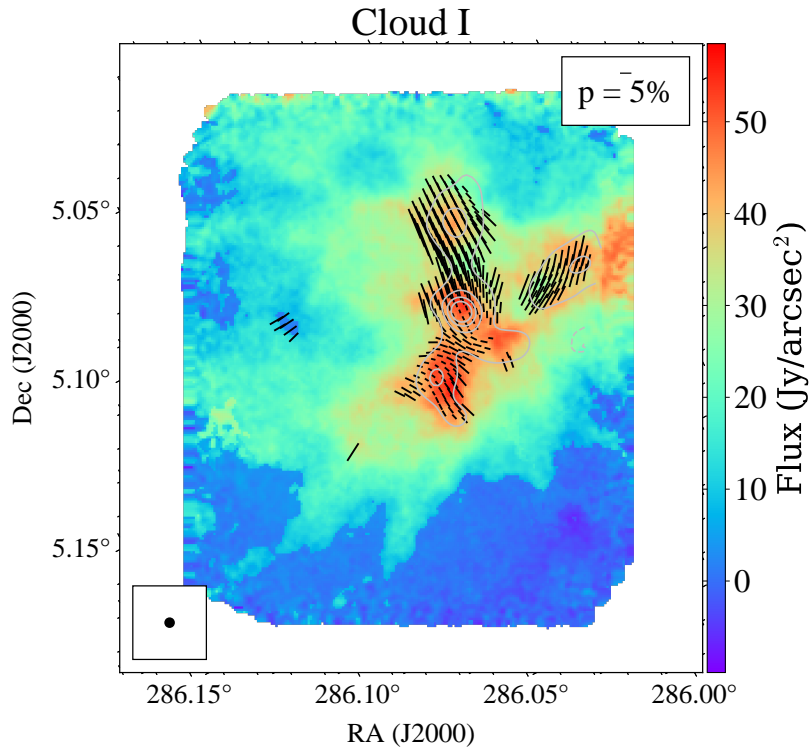


Figure 4.5: $^{13}\text{CO}(1-0)$ Moment 0 map of IRDC G38.9-0.74 overlaid with the the HAWC+ $215\mu\text{m}$ Stokes I intensity contours (silver) and the 8 intensity contours (black). The inferred magnetic field (by rotating the polarization angle with 90 degrees) is overlaid as vectors. The SOFIA beam size is presented in the bottom left corner with FWHM of $18''$. We only select polarization vectors that have $I/\sigma I \geq 50$, $\text{SNR}(P) \geq 2$, $P(\%) \leq 50$, and the uncertainty of the polarization angle $\delta\theta \leq 30$.

Bibliography

- D. Alina, J. Montillaud, Y. Hu, A. Lazarian, I. Ristorcelli, E. Abdikamalov, S. Sagynbayeva, M. Juvela, T. Liu, and J. S. Carrière. Large-scale magnetic field in the Monoceros OB-1 East molecular cloud. *arXiv e-prints*, art. arXiv:2007.15344, July 2020.
- J. Alves, M. Lombardi, and C. J. Lada. The mass function of dense molecular cores and the origin of the IMF. , 462(1):L17–L21, Jan. 2007. doi: 10.1051/0004-6361:20066389.
- P. André, A. Men’shchikov, S. Bontemps, V. Könyves, F. Motte, N. Schneider, P. Didelon, V. Minier, P. Saraceno, D. Ward-Thompson, J. di Francesco, G. White, S. Molinari, L. Testi, A. Abergel, M. Griffin, T. Henning, P. Royer, B. Merín, R. Vavrek, M. Attard, D. Arzoumanian, C. D. Wilson, P. Ade, H. Aussel, J. P. Baluteau, M. Benedettini, J. P. Bernard, J. A. D. L. Blommaert, L. Cambrésy, P. Cox, A. di Giorgio, P. Hargrave, M. Hennemann, M. Huang, J. Kirk, O. Krause, R. Launhardt, S. Leeks, J. Le Penec, J. Z. Li, P. G. Martin, A. Maury, G. Olofsson, A. Omont, N. Peretto, S. Pezzuto, T. Prusti, H. Roussel, D. Russeil, M. Sauvage, B. Sibthorpe, A. Sicilia-Aguilar, L. Spinoglio, C. Waelkens, A. Woodcraft, and A. Zavagno. From filamentary clouds to prestellar cores to the stellar IMF: Initial highlights from the Herschel Gould Belt Survey. , 518:L102, July 2010. doi: 10.1051/0004-6361/201014666.
- A. T. Barnes, J. D. Henshaw, F. Fontani, J. E. Pineda, G. Cosentino, J. C. Tan, P. Caselli, I. Jiménez-Serra, C. Y. Law, A. Avison, F. Bigiel, S. Feng, S. Kong, S. N. Longmore, L. Moser, R. J. Parker, Á. Sánchez-Monge, and K. Wang. ALMA-IRDC: dense gas mass distribution from cloud to core scales. , 503(3):4601–4626, May 2021. doi: 10.1093/mnras/stab803.
- F. Bertoldi and C. F. McKee. Pressure-confined Clumps in Magnetized Molecular Clouds. , 395:140, Aug. 1992. doi: 10.1086/171638.
- H. Beuther. Physics and chemistry of hot molecular cores. In B. G. Elmegreen and J. Palous, editors, *Triggered Star Formation in a Turbulent ISM*, volume 237, pages 148–154, Jan. 2007. doi: 10.1017/S1743921307001378.
- H. Beuther, Q. Zhang, E. A. Bergin, T. K. Sridharan, T. R. Hunter, and S. Leurini. Dust and gas emission in the prototypical hot core G29.96-0.02 at sub-arcsecond resolution. , 468(3):1045–1056, June 2007a. doi: 10.1051/0004-6361:20066954.

- H. Beuther, Q. Zhang, T. R. Hunter, T. K. Sridharan, and E. A. Bergin. The $10^5 L_{\odot}$ high-mass protostellar object IRAS 23151+5912. , 473(2):493–500, Oct. 2007b. doi: 10.1051/0004-6361:20077992.
- R. C. Bohlin, B. D. Savage, and J. F. Drake. A survey of interstellar H I from Lalpha absorption measurements. II. , 224:132–142, Aug. 1978. doi: 10.1086/156357.
- I. A. Bonnell, M. R. Bate, C. J. Clarke, and J. E. Pringle. Competitive accretion in embedded stellar clusters. , 323(4):785–794, May 2001. doi: 10.1046/j.1365-8711.2001.04270.x.
- B. Burkhardt. Diagnosing turbulence in the neutral and molecular interstellar medium of galaxies. 6 2021. URL <http://arxiv.org/abs/2106.02239>.
- M. J. Butler and J. C. Tan. Mid-Infrared Extinction Mapping of Infrared Dark Clouds: Probing the Initial Conditions for Massive Stars and Star Clusters. , 696(1):484–497, May 2009. doi: 10.1088/0004-637X/696/1/484.
- M. J. Butler and J. C. Tan. Mid-infrared Extinction Mapping of Infrared Dark Clouds. II. The Structure of Massive Starless Cores and Clumps. , 754(1):5, July 2012. doi: 10.1088/0004-637X/754/1/5.
- S. J. Carey, A. Noriega-Crespo, D. R. Mizuno, S. Shenoy, R. Paladini, K. E. Kraemer, S. D. Price, N. Flagey, E. Ryan, J. G. Ingalls, T. A. Kuchar, D. Pinheiro Gonçalves, R. Indebetouw, N. Billot, F. R. Marleau, D. L. Padgett, L. M. Rebull, E. Bressert, B. Ali, S. Molinari, P. G. Martin, G. B. Berriman, F. Boulanger, W. B. Latter, M. A. Miville-Deschenes, R. Shipman, and L. Testi. MIPS GAL: A Survey of the Inner Galactic Plane at 24 and 70 μm . , 121(875):76, Jan. 2009. doi: 10.1086/596581.
- S. Chakrabarti and S. K. Chakrabarti. Can DNA bases be produced during molecular cloud collapse? , 354:L6–L8, Feb. 2000.
- S. Chandrasekhar and E. Fermi. Magnetic Fields in Spiral Arms. , 118:113, July 1953. doi: 10.1086/145731.
- Y. Cheng, J. C. Tan, M. Liu, S. Kong, W. Lim, M. Andersen, and N. Da Rio. The Core Mass Function in the Massive Protocluster G286.21+0.17 Revealed by ALMA. , 853(2):160, Feb. 2018. doi: 10.3847/1538-4357/aaa3f1.
- E. Churchwell. Ultra-Compact HII Regions and Massive Star Formation. , 40:27–62, Jan. 2002. doi: 10.1146/annurev.astro.40.060401.093845.
- J. J. Condon and S. M. Ransom. *Essential Radio Astronomy*. 2016.
- G. Cosentino, I. Jiménez-Serra, J. D. Henshaw, P. Caselli, S. Viti, A. T. Barnes, J. C. Tan, F. Fontani, and B. Wu. SiO emission as a probe of cloud-cloud collisions in infrared dark clouds. , 499(2):1666–1681, Dec. 2020. doi: 10.1093/mnras/staa2942.
- R. M. Crutcher. Magnetic Fields in Molecular Clouds. , 50:29–63, Sept. 2012. doi: 10.1146/annurev-astro-081811-125514.

- T. Csengeri, S. Bontemps, F. Wyrowski, F. Motte, K. M. Menten, H. Beuther, L. Bronfman, B. Commerçon, E. Chapillon, A. Duarte-Cabral, G. A. Fuller, T. Henning, S. Leurini, S. Longmore, A. Palau, N. Peretto, F. Schuller, J. C. Tan, L. Testi, A. Traficante, and J. S. Urquhart. ALMA survey of massive cluster progenitors from ATLASGAL. Limited fragmentation at the early evolutionary stage of massive clumps. , 600:L10, Apr. 2017. doi: 10.1051/0004-6361/201629754.
- C. J. Cyganowski, C. L. Brogan, T. R. Hunter, R. Smith, J. M. D. Kruijssen, I. A. Bonnell, and Q. Zhang. Simultaneous low- and high-mass star formation in a massive protocluster: ALMA observations of G11.92-0.61. , 468(3):3694–3708, July 2017. doi: 10.1093/mnras/stx043.
- R. Devaraj, D. P. Clemens, L. K. Dewangan, A. Luna, T. P. Ray, and J. Mackey. Magnetic Fields and Star Formation around H II Regions: The S235 Complex. , 911(2):81, Apr. 2021. doi: 10.3847/1538-4357/abe9b1.
- M. P. Egan, R. F. Shipman, S. D. Price, S. J. Carey, F. O. Clark, and M. Cohen. A Population of Cold Cores in the Galactic Plane. , 494(2):L199–L202, Feb. 1998. doi: 10.1086/311198.
- N. Entekhabi, J. C. Tan, G. Cosentino, C.-J. Hsu, P. Caselli, C. Walsh, W. Lim, J. D. Henshaw, A. T. Barnes, F. Fontani, and I. Jiménez-Serra. Astrochemical Modelling of Infrared Dark Clouds. *arXiv e-prints*, art. arXiv:2111.05379, Nov. 2021.
- R. T. Garrod. A Three-phase Chemical Model of Hot Cores: The Formation of Glycine. , 765(1):60, Mar. 2013. doi: 10.1088/0004-637X/765/1/60.
- P. Goldreich and S. Sridhar. Toward a Theory of Interstellar Turbulence. II. Strong Alfvénic Turbulence. , 438:763, Jan. 1995. doi: 10.1086/175121.
- A. K. Hernandez and J. C. Tan. The Giant Molecular Cloud Environments of Infrared Dark Clouds. , 809(2):154, Aug. 2015. doi: 10.1088/0004-637X/809/2/154.
- A. K. Hernandez, J. C. Tan, P. Caselli, M. J. Butler, I. Jiménez-Serra, F. Fontani, and P. Barnes. Mapping Large-scale CO Depletion in a Filamentary Infrared Dark Cloud. , 738(1):11, Sept. 2011. doi: 10.1088/0004-637X/738/1/11.
- M. Heyer, J. D. Soler, and B. Burkhart. The relative orientation between the magnetic field and gradients of surface brightness within thin velocity slices of ^{12}CO and ^{13}CO emission from the Taurus molecular cloud. , 496(4):4546–4564, Aug. 2020. doi: 10.1093/mnras/staa1760.
- M. G. Hoare, S. E. Kurtz, S. Lizano, E. Keto, and P. Hofner. Ultracompact Hii Regions and the Early Lives of Massive Stars. In B. Reipurth, D. Jewitt, and K. Keil, editors, *Protostars and Planets V*, page 181, Jan. 2007.
- C.-J. Hsu, J. C. Tan, M. D. Goodson, P. Caselli, B. Körtgen, and Y. Cheng. Deuterium chemodynamics of massive pre-stellar cores. , 502(1):1104–1127, Mar. 2021. doi: 10.1093/mnras/staa4031.

- Y. Hu, K. H. Yuen, V. Lazarian, K. W. Ho, R. A. Benjamin, A. S. Hill, F. J. Lockman, P. F. Goldsmith, and A. Lazarian. Magnetic field morphology in interstellar clouds with the velocity gradient technique. *Nature Astronomy*, 3:776–782, June 2019. doi: 10.1038/s41550-019-0769-0.
- S.-i. Inutsuka, T. Inoue, K. Iwasaki, and T. Hosokawa. The formation and destruction of molecular clouds and galactic star formation. An origin for the cloud mass function and star formation efficiency. , 580:A49, Aug. 2015. doi: 10.1051/0004-6361/201425584.
- I. Jiménez-Serra, P. Caselli, F. Fontani, J. C. Tan, J. D. Henshaw, J. Kainulainen, and A. K. Hernandez. Gas kinematics and excitation in the filamentary IRDC G035.39-00.33. , 439(2):1996–2013, Apr. 2014. doi: 10.1093/mnras/stu078.
- J. Kainulainen and J. C. Tan. High-dynamic-range extinction mapping of infrared dark clouds. Dependence of density variance with sonic Mach number in molecular clouds. , 549:A53, Jan. 2013. doi: 10.1051/0004-6361/201219526.
- M. S. Kirsanova, A. M. Sobolev, M. Thomasson, D. S. Wiebe, L. E. B. Johansson, and A. F. Seleznev. Star formation around the HII region Sh2-235. , 388(2): 729–736, Aug. 2008. doi: 10.1111/j.1365-2966.2008.13429.x.
- C. Kobayashi, A. I. Karakas, and H. Umeda. The evolution of isotope ratios in the milky way galaxy. *Monthly Notices of the Royal Astronomical Society*, 414: 3231–3250, 7 2011. ISSN 00358711. doi: 10.1111/j.1365-2966.2011.18621.x.
- V. Könyves, P. André, A. Men’shchikov, P. Palmeirim, D. Arzoumanian, N. Schneider, A. Roy, P. Didelon, A. Maury, Y. Shimajiri, J. Di Francesco, S. Bontemps, N. Peretto, M. Benedettini, J. P. Bernard, D. Elia, M. J. Griffin, T. Hill, J. Kirk, B. Ladjelate, K. Marsh, P. G. Martin, F. Motte, Q. Nguyễn Luong, S. Pezzuto, H. Roussel, K. L. J. Rygl, S. I. Sadavoy, E. Schisano, L. Spinoglio, D. Ward-Thompson, and G. J. White. A census of dense cores in the Aquila cloud complex: SPIRE/PACS observations from the Herschel Gould Belt survey. , 584:A91, Dec. 2015. doi: 10.1051/0004-6361/201525861.
- M. R. Krumholz. Star Formation in Molecular Clouds. In E. Telles, R. Dupke, and D. Lazzaro, editors, *XV Special Courses at the National Observatory of Rio de Janeiro*, volume 1386 of *American Institute of Physics Conference Series*, pages 9–57, Sept. 2011. doi: 10.1063/1.3636038.
- R. B. Larson. Turbulence and star formation in molecular clouds. , 194:809–826, Mar. 1981. doi: 10.1093/mnras/194.4.809.
- A. Lazarian, K. H. Yuen, K. W. Ho, J. Chen, V. Lazarian, Z. Lu, B. Yang, and Y. Hu. Distribution of Velocity Gradient Orientations: Mapping Magnetization with the Velocity Gradient Technique. , 865(1):46, Sept. 2018. doi: 10.3847/1538-4357/aad7ff.

- H. B. Li, A. Goodman, T. K. Sridharan, M. Houde, Z. Y. Li, G. Novak, and K. S. Tang. The Link Between Magnetic Fields and Cloud/Star Formation. In H. Beuther, R. S. Klessen, C. P. Dullemond, and T. Henning, editors, *Protostars and Planets VI*, page 101, Jan. 2014. doi: 10.2458/azu_uapress_9780816531240-ch005.
- W. Lim, J. C. Tan, J. Kainulainen, B. Ma, and M. Butler. The Mass Surface Density Distribution of a High-Mass Protocluster forming from an IRDC and GMC. In *American Astronomical Society Meeting Abstracts #227*, volume 227 of *American Astronomical Society Meeting Abstracts*, page 424.06, Jan. 2016.
- M. Liu, J. C. Tan, Y. Cheng, and S. Kong. The Core Mass Function across Galactic Environments. II. Infrared Dark Cloud Clumps. , 862(2):105, Aug. 2018. doi: 10.3847/1538-4357/aacb7c.
- C. F. McKee and E. C. Ostriker. Theory of Star Formation. , 45(1):565–687, Sept. 2007. doi: 10.1146/annurev.astro.45.051806.110602.
- C. F. McKee and J. C. Tan. The Formation of Massive Stars from Turbulent Cores. , 585(2):850–871, Mar. 2003. doi: 10.1086/346149.
- J. P. McMullin, B. Waters, D. Schiebel, W. Young, and K. Golap. CASA Architecture and Applications. In R. A. Shaw, F. Hill, and D. J. Bell, editors, *Astronomical Data Analysis Software and Systems XVI*, volume 376 of *Astronomical Society of the Pacific Conference Series*, page 127, Oct. 2007.
- F. Motte, S. Bontemps, and F. Louvet. High-Mass Star and Massive Cluster Formation in the Milky Way. , 56:41–82, Sept. 2018. doi: 10.1146/annurev-astro-091916-055235.
- A. T. Myers, C. F. McKee, A. J. Cunningham, R. I. Klein, and M. R. Krumholz. The Fragmentation of Magnetized, Massive Star-forming Cores with Radiative Feedback. , 766(2):97, Apr. 2013. doi: 10.1088/0004-637X/766/2/97.
- T. J. O’Neill, G. Cosentino, J. C. Tan, Y. Cheng, and M. Liu. The Core Mass Function across Galactic Environments. III. Massive Protoclusters. , 916(1):45, July 2021. doi: 10.3847/1538-4357/ac062d.
- P. Padoan, L. Pan, M. Juvela, T. Haugbølle, and Å. Nordlund. The Origin of Massive Stars: The Inertial-inflow Model. , 900(1):82, Sept. 2020. doi: 10.3847/1538-4357/abaa47.
- M. Perault, A. Omont, G. Simon, P. Seguin, D. Ojha, J. Blommaert, M. Felli, G. Gilmore, F. Guglielmo, H. Habing, S. Price, A. Robin, B. de Batz, C. Cesarsky, D. Elbaz, N. Epchtein, P. Fouque, S. Guest, D. Levine, A. Pollock, T. Prusti, R. Siebenmorgen, L. Testi, and D. Tiphene. First ISOCAM images of the Milky Way. , 315:L165–L168, Nov. 1996.
- T. Pillai, J. Kauffmann, J. C. Tan, P. F. Goldsmith, S. J. Carey, and K. M. Menten. Magnetic Fields in High-mass Infrared Dark Clouds. , 799(1):74, Jan. 2015. doi: 10.1088/0004-637X/799/1/74.

- J. M. Rathborne, J. M. Jackson, and R. Simon. Infrared Dark Clouds: Precursors to Star Clusters. , 641(1):389–405, Apr. 2006. doi: 10.1086/500423.
- L. F. Rodríguez. Radio observations of ultracompact HII regions. In R. Cesaroni, M. Felli, E. Churchwell, and M. Walmsley, editors, *Massive Star Birth: A Crossroads of Astrophysics*, volume 227, pages 120–127, Jan. 2005. doi: 10.1017/S1743921305004436.
- D. Romano, F. Matteucci, Z.-Y. Zhang, R. J. Ivison, and P. Ventura. The evolution of cno isotopes: the impact of massive stellar rotators. *Monthly Notices of the Royal Astronomical Society*, 490:2838–2854, 12 2019. ISSN 0035-8711. doi: 10.1093/mnras/stz2741.
- A. L. Rosen, S. S. R. Offner, S. I. Sadavoy, A. Bhandare, E. Vázquez-Semadeni, and A. Ginsburg. Zooming in on individual star formation: Low- and high-mass stars. 216:62, 5 2020. doi: 10.1007/s11214-020-00688-5.
- P. Sanhueza, Y. Contreras, B. Wu, J. M. Jackson, A. E. Guzmán, Q. Zhang, S. Li, X. Lu, A. Silva, N. Izumi, T. Liu, R. E. Miura, K. Tatematsu, T. Sakai, H. Beuther, G. Garay, S. Ohashi, M. Saito, F. Nakamura, K. Saigo, V. S. Veena, Q. Nguyen-Luong, and D. Tafuya. The ALMA Survey of 70 μ m Dark High-mass Clumps in Early Stages (ASHES). I. Pilot Survey: Clump Fragmentation. , 886(2):102, Dec. 2019. doi: 10.3847/1538-4357/ab45e9.
- D. Seifried, R. E. Pudritz, R. Banerjee, D. Duffin, and R. S. Klessen. Magnetic fields during the early stages of massive star formation - II. A generalized outflow criterion. , 422(1):347–366, May 2012. doi: 10.1111/j.1365-2966.2012.20610.x.
- M. Sewilo, E. Churchwell, S. Kurtz, W. M. Goss, and P. Hofner. Internal dynamics of the hypercompact h ii region g28.20-0.04n. 681:350–354, 7 2008. doi: 10.1086/588422.
- F. H. Shu, F. C. Adams, and S. Lizano. Star formation in molecular clouds: observation and theory. , 25:23–81, Jan. 1987. doi: 10.1146/annurev.aa.25.090187.000323.
- M. Sieth, K. Devaraj, P. Voll, S. Church, R. Gawande, K. Cleary, A. C. S. Readhead, P. Kangaslahti, L. Samoska, T. Gaier, P. F. Goldsmith, A. I. Harris, J. O. Gundersen, D. Frayer, S. White, D. Egan, and R. Reeves. Argus: a 16-pixel millimeter-wave spectrometer for the Green Bank Telescope. In W. S. Holland and J. Zmuidzinas, editors, *Millimeter, Submillimeter, and Far-Infrared Detectors and Instrumentation for Astronomy VII*, volume 9153 of *Society of Photo-Optical Instrumentation Engineers (SPIE) Conference Series*, page 91530P, July 2014. doi: 10.1117/12.2055655.
- R. Simon, J. M. Rathborne, R. Y. Shah, J. M. Jackson, and E. T. Chambers. The Characterization and Galactic Distribution of Infrared Dark Clouds. , 653(2): 1325–1335, Dec. 2006. doi: 10.1086/508915.

- A. Soam, T. Liu, B. G. Andersson, C. W. Lee, J. Liu, M. Juvela, P. S. Li, P. F. Goldsmith, Q. Zhang, P. M. Koch, K.-T. Kim, K. Qiu, I. Evans, Neal J., D. Johnstone, M. Thompson, D. Ward-Thompson, J. Di Francesco, Y.-W. Tang, J. Montillaud, G. Kim, S. Mairs, P. Sanhueza, S. Kim, D. Berry, M. S. Gordon, K. Tatematsu, S.-Y. Liu, K. Pattle, D. Eden, P. M. McGehee, K. Wang, I. Ristorcelli, S. F. Graves, D. Alina, K. M. Lacaille, L. Montier, G. Park, W. Kwon, E. J. Chung, V.-M. Pelkonen, E. R. Micelotta, M. Saajasto, and G. Fuller. Magnetic Fields in the Infrared Dark Cloud G34.43+0.24. , 883(1):95, Sept. 2019. doi: 10.3847/1538-4357/ab39dd.
- V. Sokolov, K. Wang, J. E. Pineda, P. Caselli, J. D. Henshaw, J. C. Tan, F. Fontani, I. Jiménez-Serra, and W. Lim. Temperature structure and kinematics of the IRDC G035.39-00.33. , 606:A133, Oct. 2017. doi: 10.1051/0004-6361/201630350.
- J. C. Tan, S. Kong, M. J. Butler, P. Caselli, and F. Fontani. The Dynamics of Massive Starless Cores with ALMA. , 779(2):96, Dec. 2013. doi: 10.1088/0004-637X/779/2/96.
- J. C. Tan, M. T. Beltrán, P. Caselli, F. Fontani, A. Fuente, M. R. Krumholz, C. F. McKee, and A. Stolte. Massive star formation. page 149, 1 2014. doi: 10.2458/azu_uapress_9780816531240-ch007.
- K. E. I. Tanaka, J. C. Tan, and Y. Zhang. The Impact of Feedback During Massive Star Formation by Core Accretion. , 835(1):32, Jan. 2017. doi: 10.3847/1538-4357/835/1/32.
- Y.-W. Tang, P. M. Koch, N. Peretto, G. Novak, A. Duarte-Cabral, N. L. Chapman, P.-Y. Hsieh, and H.-W. Yen. Gravity, Magnetic Field, and Turbulence: Relative Importance and Impact on Fragmentation in the Infrared Dark Cloud G34.43+00.24. , 878(1):10, June 2019. doi: 10.3847/1538-4357/ab1484.
- F. F. S. van der Tak. Hot Molecular Cores and High Mass Star Formation. In M. G. Burton, R. Jayawardhana, and T. L. Bourke, editors, *Star Formation at High Angular Resolution*, volume 221, page 59, Sept. 2004.
- D. Ward-Thompson and A. P. Whitworth. *An Introduction to Star Formation*. Cambridge University Press, 2011. ISBN 9780511974021. doi: 10.1017/CBO9780511974021. URL <http://ebooks.cambridge.org/ref/id/CBO9780511974021>.
- T. V. Wenger, J. R. Dawson, J. M. Dickey, C. H. Jordan, N. M. McClure-Griffiths, L. D. Anderson, W. P. Armentrout, D. S. Balser, and T. M. Bania. The Southern H II Region Discovery Survey. II. The Full Catalog. , 254(2):36, June 2021. doi: 10.3847/1538-4365/abf4d4.
- D. O. S. Wood and E. Churchwell. The Morphologies and Physical Properties of Ultracompact H II Regions. , 69:831, Apr. 1989. doi: 10.1086/191329.

- B. Wu, J. C. Tan, F. Nakamura, D. Christie, and Q. Li. Giant molecular cloud collisions as triggers of star formation. VI. Collision-induced turbulence. , 70:S57, May 2018. doi: 10.1093/pasj/psx140.
- K. H. Yuen and A. Lazarian. Tracing Interstellar Magnetic Field Using Velocity Gradient Technique: Application to Atomic Hydrogen Data. , 837(2):L24, Mar. 2017. doi: 10.3847/2041-8213/aa6255.

Part II

Appended papers

Paper 1

Isolated Massive Star Formation in G28.2-0.05

Law, C.Y., Jonathan C. Tan, Prasanta Gorai, Yichen Zhang,
Rubén Fedriani, Daniel Tafoya, Kei Tanaka, Giuliana Cosentino,
and Yao-Lun Yang

Manuscript intended for Astrophysical Journal

Paper 1. Isolated Massive Star Formation in G28.2-0.05

Law,C.Y., Jonathan C. Tan, Prasanta Gorai, Yichen Zhang, Rubén Fedriani, Daniel
Tafoya, Kei Tanaka, Giuliana Cosentino, and Yao-Lun Yang

Isolated Massive Star Formation in G28.2-0.05

C. Y. LAW,^{1,2} JONATHAN C. TAN,^{1,3} PRASANTA GORAI,¹ YICHEN ZHANG,⁴ RUBÉN FEDRIANI,¹ DANIEL TAFOYA,⁵
KEI TANAKA,^{6,7} GIULIANA COSENTINO,¹ AND YAO-LUN YANG³

¹*Department of Space, Earth & Environment, Chalmers University of Technology, SE-412 96 Gothenburg, Sweden*

²*European Southern Observatory, Karl-Schwarzschild-Strasse 2, D-85748 Garching, Germany*

³*Department of Astronomy, University of Virginia, Charlottesville, VA 22904-4325, USA*

⁴*Star and Planet Formation Laboratory, RIKEN Cluster for Pioneering Research, Wako, Saitama 351-0198, Japan*

⁵*Department of Space, Earth and Environment, Chalmers University of Technology, Onsala Space Observatory, 439 92 Onsala, Sweden*

⁶*National Astronomical Observatory of Japan, Mitaka, Tokyo 181-8588, Japan*

⁷*Department of Earth and Space Science, Osaka University, Toyonaka, Osaka 560-0043, Japan*

(Received; Revised; Accepted)

Submitted to ApJ

ABSTRACT

We report high resolution 1.3 mm continuum and molecular line observations of the massive protostar G28.2-0.05 with the Atacama Large Millimeter/Submillimeter Array (ALMA). We identify a ring-like structure in the continuum image with radius of about 2,000 AU, which has also been reported previously at lower resolution in 1.3 cm observations with the VLA. A spectral index analysis and the presence of H30 α indicates that this ring mostly traces ionized gas, although there is evidence for $\sim 30 M_{\odot}$ of dusty gas near the main mm continuum peak on one side of the ring, as well as around the ring within 3,000 au. High excitation molecular lines tracing dense and warm molecular gas are also seen around the main mm continuum peak. A virial analysis on scales of about 2,000 au yields a dynamical mass of about $80 M_{\odot}$. The H30 α emission around the main mm peak shows a large velocity gradient, which we interpret as a rotating, ionized disk wind that may be launched from the inner ~ 100 au around a massive star of $\sim 30 M_{\odot}$. Such a disk wind is also likely to be the driver of a large-scale, wide-angle bipolar molecular outflow that is seen in CO and SiO emission. We model the spectral energy distribution of G28.2-0.05 from the mid to far-infrared and derive best-fit results for a protostar that currently has $\sim 24 M_{\odot}$ and is forming from a core with initial mass of $\sim 400 M_{\odot}$ in a clump with mass surface density of $\Sigma_{\text{cl}} \sim 3 \text{ g cm}^{-3}$. Structure-finding analysis on the larger-scale continuum image suggests G28.2-0.05 is forming in a relatively isolated environment, with no other concentrated mass structures, i.e., protostellar cores, above $0.4 M_{\odot}$ found on scales from about 0.1 pc to 0.4 pc around the source. Our results indicate that a massive star is able to form in relative isolation from other protostars. The properties of the system can be understood in the context of core accretion models. The dearth of other protostellar companions within the ~ 1 pc scale surroundings is a strong constraint on massive star formation theories that predict the presence of a surrounding protocluster.

Keywords: Interstellar medium, Star formation

1. INTRODUCTION

Massive ($> 8 M_{\odot}$) stars impact many areas of astrophysics, however, the mechanism of their formation is still under debate. Two main scenarios are (i) Core Accretion (e.g., the Turbulent Core Accretion model of Mc-

Kee & Tan 2003) and (ii) Competitive Accretion (e.g., Bonnell et al. 2001; Wang et al. 2010) (see, e.g., Tan et al. 2014 for a review). The former is a scaled-up version of the standard model of low-mass star formation (Shu et al. 1987), although with the internal pressure of the massive pre-stellar core being dominated by turbulence and/or magnetic fields, rather than thermal pressure. This implies the collapse will likely be more

disordered than in the low-mass case, perhaps including significant accretion via overdense filaments and other sub-structures, e.g., as seen in magnetohydrodynamical (MHD) simulations of such structures (e.g. Seifried et al. 2012; Myers et al. 2013; Hsu et al. 2021). A characteristic feature of core accretion models is a more direct linkage of the pre-stellar core mass function (CMF) and the stellar initial mass function (IMF), although perhaps mediated by effects of a varying core-to-star formation efficiency and binary or small- N multiple formation by disk fragmentation within a core.

In Competitive Accretion, stars chaotically gain their mass via the global collapse of the clump without passing through the massive pre-stellar core phase. In the context of the competitive accretion model, there is no correlation between the CMF and the IMF as the accretion involve ambient gas materials of the cloud.

Identification of relatively isolated massive protostar candidates provides a direct way to constrain massive star formation. Relatively isolated massive protostars, i.e., with limited surrounding fragmentation and star formation, indicate that collapse of a massive core has occurred in a relatively monolithic manner. For instance, Csengeri et al. (2017) studied 35 sources with *ALMA* and found that most of them show limited fragmentation, with at most 3 cores per clump. Louvet et al. (2019) also found low levels of fragmentation in the massive cores of the NGC-6334 region. On the other hand, Cyganowski et al. (2017) studied the high-mass star-forming region G11.92-0.61 finding that the three massive protostars in the region are surrounded by at least 16 lower mass protostellar sources within a region about 0.3 pc in radius.

Protostars forming via core accretion, especially in relatively uncrowded environments, are more likely to involve an ordered transition from the infall envelope to a Keplerian disk, as has been claimed in G339.88-1.26 by Zhang et al. (2019). They are also more likely to exhibit relatively ordered outflows, i.e., launched orthogonally to the accretion disk and maintaining their orientation for relatively long periods.

Additional observational studies of relatively isolated massive protostars are important to test theoretical models. In this work, we analyse 1.3 mm (band 6) continuum and line data observed by *ALMA* of the massive protostar G28.2-0.05. This source has been characterized as being a high luminosity ($\sim 1.4 - 1.6 \times 10^5 L_{\odot}$) (Hernández-Hernández et al. 2014; Maud et al. 2015) shell-like hypercompact HII region and a hot molecular core (Walsh et al. 2003; Sewilo et al. 2004; Qin et al. 2008) at a distance of $5.7^{+0.5}_{-0.8}$ kpc (Fish et al. 2003; Sollins et al. 2005; Qin et al. 2008), which will

be adopted throughout this work. The source systemic velocity is $v_{\text{sys}} = 95.6 \pm 0.5 \text{ km s}^{-1}$. We note that some previous studies adopted a larger distance of 9.1 kpc (Kurtz et al. 1994; de la Fuente et al. 2020). Within a radius of 0.48 pc, G28.2-0.05 has an estimated gas mass of $33 M_{\odot}$, and thus a mass surface density of $(33 \times 1.989 \times 10^{33}) / ((3.086 \times 10^{18} \times 0.48)^2 \times \pi) = 9.52 \times 10^{-3} \text{ g cm}^{-2}$ (Hernández-Hernández et al. 2014). Previous studies (e.g., Sollins et al. 2005) have suggested the presence of two components: (i) an infalling equatorial torus molecular gas, whose dense central ionized gas produce HII regions, and (ii) an extended molecular shell which is associated wide angle outflow or wind. Furthermore, Klaassen et al. (2009) presented SMA observations and inferred from a velocity gradient perpendicular to the outflow direction that warm molecular gas (e.g., as traced by SO_2) is undergoing bulk rotation. Klaassen et al. (2011) detected a large and wide angle ^{12}CO ($2 - 1$) outflow based on the *JCMT* observations. Furthermore, various masers (OH , H_2O , CH_3OH) and in-fall motions have been revealed from centimeter wavelengths observations of molecular and radio recombination lines (Sollins et al. 2005; Sewilo et al. 2008).

Qin et al. (2008) presented a chemical study of the source with the SMA to measure the kinetic temperature and column density of the source. Based on multiple K-components of the CH_3CN and rotational diagram method, the authors measure a rotational temperature of about 300 K.

This paper is organized as follows. In §2, we summarise the observations and the reduction procedures. We characterise the spectral energy distribution (SED) of the source in §4. We study the continuum and molecular line morphology of the protostar in §3.1. We model the spectral energy distribution (SED) of the protostar in §4. In §5 we characterise the large scale fragmentation of the source. Finally, a summary is presented in §6.

2. ALMA OBSERVATIONS & DATA REDUCTION

G28.2-0.05 was observed with *ALMA* in Band 6 via a Cycle 3 project (PI: Y. Zhang; 2015.1.01454.S) with compact (C36-2, C)¹ and intermediate (C36-5, I) array configurations and via a Cycle 4 project (PI: J. Tan; 2016.1.00125.S) with a long-baseline (C40-9, E)² configuration (see Table 1). In each case, a single pointing observation was made with a primary beam size (half

¹ <https://almascience.eso.org/documents-and-tools/cycle3/alma-technical-handbook> (Table 7.1)

² <https://arc.iram.fr/documents/cycle4/ALMACycle4TechnicalHandbook-Final.pdf> (Tale 7.1)

power beam width) of $26.9''^3$. All the observations have the same spectral set-up, covering frequencies from 216.7 to 234.9 GHz. Information about the spectral band passes used in the observations is given in Table 2. The total integration times were 4.2, 16.2 and 130.4 minutes in these configurations, respectively. For the Cycle 3 observations, J1427-4206 was used for band-pass calibration, J1617-5848 and Titan were used for flux calibration, and J1636-4102 and J1706-4600 were used as phase calibrators. For the Cycle 4 observations, J1924-2914 was used for band-pass calibration, J1834-0301 and J1846-0651 were used for phase calibration.

All data reduction and imaging was performed with CASA (McMullin et al. 2007) using version 5.6.1-8. After pipeline calibration, we performed the continuum and line imaging separately. For the continuum imaging, we image and self-calibrate each spectral window based on line-free channels with task *tclean* using 'briggs' weighting with a robust parameter of 0.5. We identify line-free channels as follows. We first inspect the raw spectrum of each spectral window and identify representative line free channels. We then define a threshold by the root mean square (rms; $\sigma_{\text{rms}} = \sqrt{\sum_n I_n^2/n}$) of those channels. Any channels that are within four times the rms are counted as line free channels. We then use these line free channels to form the individual spectral window continuum images, as well as the total continuum image. We perform four iterations of phase-only calibrations with solution intervals of 30s, 10s, and 'int' with manual masking. Finally, an iteration of amplitude calibration with manual masking, which we also apply to the line data.

The resulting synthesized beams of each configuration are summarized in Table 1. We self-calibrated each configuration before combining them using the CASA function *concat* to obtain the final combined continuum images. During combination, we weight each configuration based on their average time intervals (Table 1 Column 6)⁴. The final weightings are 1, 1 and 0.33 for the Compact (C), Intermediate (I) and Extended (E) baseline configurations, respectively. The combined (C+I+E) continuum was then cleaned interactively with manual masking with multi-scale deconvolver at scales of 0, 10, 50, 150 pixels. The resulting synthesized beam of the final combined continuum image is $0.060'' \times 0.036''$. A summary of the observations and configuration set up is given in Table 1. We note that the maximum recover-

able scale ranges from $0.34''$ to $11''$, while the resolution ranges from about $0.026''$ to $0.813''$.

The root-mean-squared (rms) noise level in a given continuum image (before primary beam correction) is done by sampling 5000 regions each with area equal to the synthesized beam. We then fit a Gaussian to this distribution of fluxes and estimate the 1σ noise level from the standard deviation of this Gaussian. The 1σ noise levels in the C, C+I and C+I+E configuration images are 1.29, 0.358, and $0.170 \text{ mJy bm}^{-1}$ respectively.

For molecular line imaging, we first subtract the baseline in the uv plane using *uvcontsub* in CASA. The continuum emission is obtained by subtracting line-free channels using the *uvcontsub* function. We apply manual masking during line imaging. We use *tclean* to image the emission lines, again with 'briggs' weighting and robust factor of 0.5 and multiscale deconvolver at scales of 0, 10, 50, 150 pixels. Unless otherwise mentioned specifically, science measurements are performed on the primary beam corrected images.

3. CHARACTERIZING THE PROTOSTAR

3.1. Morphology

Figure 1 presents an overview of the G28.2-0.05 protostellar system and its surroundings. Panel (a) shows the *Spitzer*-IRAC $8 \mu\text{m}$ image of the large-scale environment around the source, spanning 7 pc by 10 pc. The protostar is visible as a MIR-bright compact source that is embedded in a MIR-dark filament, i.e., an IRDC. We note that the G28.2-0.05 source is close in the sky position (about $6'$) to the well-studied, massive IRDC G028.37+00.07 (also known as Cloud C in the sample of Butler & Tan 2009, 2012), which has a similar estimated kinematic distance of 5 kpc. The uncertainties in kinematic distances are such that it is possible these sources could be in close proximity, with the projected separation being about 10 pc.

Figure 1(b) presents the *Herschel* $70 \mu\text{m}$ continuum map of G28.2-0.05. The dynamic range in intensity of this image spans more than a factor of 1,000. In this image the central source appears to be relatively isolated with no detection greater than 1% of peak emission within a $2'$ (3.3 pc) radius around it.

Figure 1(c) shows the primary beam corrected ALMA 1.3 mm continuum image derived from the compact (C) configuration observation. As described above, the 1σ noise level in the central part of this image is 1.29 mJy bm^{-1} . The color stretch is set to have a minimum value of 0.1σ . The image shows a central, compact source that is surrounded by a halo of fainter emission, but with an absence of other bright sources.

³ <https://almascience.nrao.edu/about-alma/alma-basics>

⁴ <https://casaguides.nrao.edu/index.php/DataWeightsAndCombination>

Table 1: Summary of ALMA observations toward G28.2-0.05

Start of Obs.	Obs. time (min.)	Config.	Antennas used	Baseline Lengths (m)	Averaged Interval (sec.)	MRS (")	Beam size (")
2016 April 24 07:44:13.2	4.17	C	41	14.7 - 376.9	6.05	11.0	0.735×0.813
2016 Sept 11 02:45:50.2	16.2	I	37	47.9 - 1396	6.05	3.40	0.201×0.217
2017 Sept 30 01:53:01.1	34.5		41				
2017 Nov 1 00:15:20.2	34.8	E	49	346.5 - 9743	2.02	0.340	0.026×0.048
2017 Nov 5 23:00:02.4	61.1		47				

Table 2: Summary of ALMA spectral windows set-up

Spectral Window	Molecular Line	Frequency range (MHz)	Channel Spacing (kHz)	rms (mJy bm^{-1})
Spw0	CH ₃ OH(4 _{2,3} - 5 _{1,4})	232928.10 - 234928.10	15625.00	0.600
Spw1	H(30) α	231587.86 - 232056.61	488.28	0.810
Spw2	¹² CO(2-1)	230297.25 - 230765.99	488.28	0.310
Spw3	H ₂ CO (9 _{1,8} - 9 _{1,9})	218714.73 - 218656.14	112.07	0.717
Spw4	CH ₃ OH(4 _{-2,3} - 3 _{-1,2})	21839.79 - 218365.55	112.07	0.589
Spw5	C ¹⁸ O (2-1)	219514.81 - 219485.58	112.07	0.460
Spw6	CH ₃ CN	220278.12 - 220248.88	112.07	0.890
Spw7	SiO(5-4)	217147.97 - 217031.03	488.28	0.279
Spw8	SO ₂	216685.46 - 216451.08	488.28	0.710

Figure 1(d) shows the primary beam corrected 1.3 mm continuum image derived from the compact and intermediate combined (C+I) data, with 1σ noise level of $0.358 \text{ mJy } \text{bm}^{-1}$ in the central regions. Again, the color stretch is set to have a minimum value of 0.1σ . This image reveals finer details and substructure of the central source. However, again, there is no clear evidence of strong, compact secondary sources in the wider FOV. We return to this topic with a quantitative analysis of this image for the presence of secondary sources in §5.

Figure 1(e) shows the primary beam corrected 1.3 mm continuum image derived from all the configurations combined (C+I+E), while Figure 1(f) presents a zoom-in view of the central source. The range of intensities shown extends down to 0.1σ , with the 1σ noise level being $0.170 \text{ mJy } \text{bm}^{-1}$ in the central regions. The image reveals a ring-like structure with a radius from its central minimum to bright rim of $\sim 0.01 \text{ pc}$ (2,000 AU). Three peaks have been identified within the ring. The main peak of the continuum emission is on the SW side

at R.A. = $18 : 42 : 58.0997$, DEC. = $-4 : 13 : 57.636$. A secondary peak is found on the NE side and a third relatively faint peak toward the northern part of the ring. Outside of the ring, more extended, fainter structures are visible, especially on each side that is aligned to the apparent long axis of the ring, i.e., NW to SE.

3.2. Radio to mm Spectral Index to Probe Ionized and Dusty Gas

Sewilo et al. (2008, 2011) carried out high resolution VLA observations toward G28.2-0.05 at 1.3 cm (22.4 GHz, i.e., radio K-band) and detected a ring-like structure that is similar to the one we see in the 1.3 mm continuum. Figures 2(a) and (b) present the archival VLA 1.3 cm continuum image overlaid with the E only and C+I+E combined 1.3 mm continuum images, respectively. On first inspection the images show very similar morphology at these two wavelengths. Assuming the 1.3 cm continuum traces free-free emission from ionized gas, this suggests that a significant portion of the 1.3 mm continuum is also contributed by such emission.

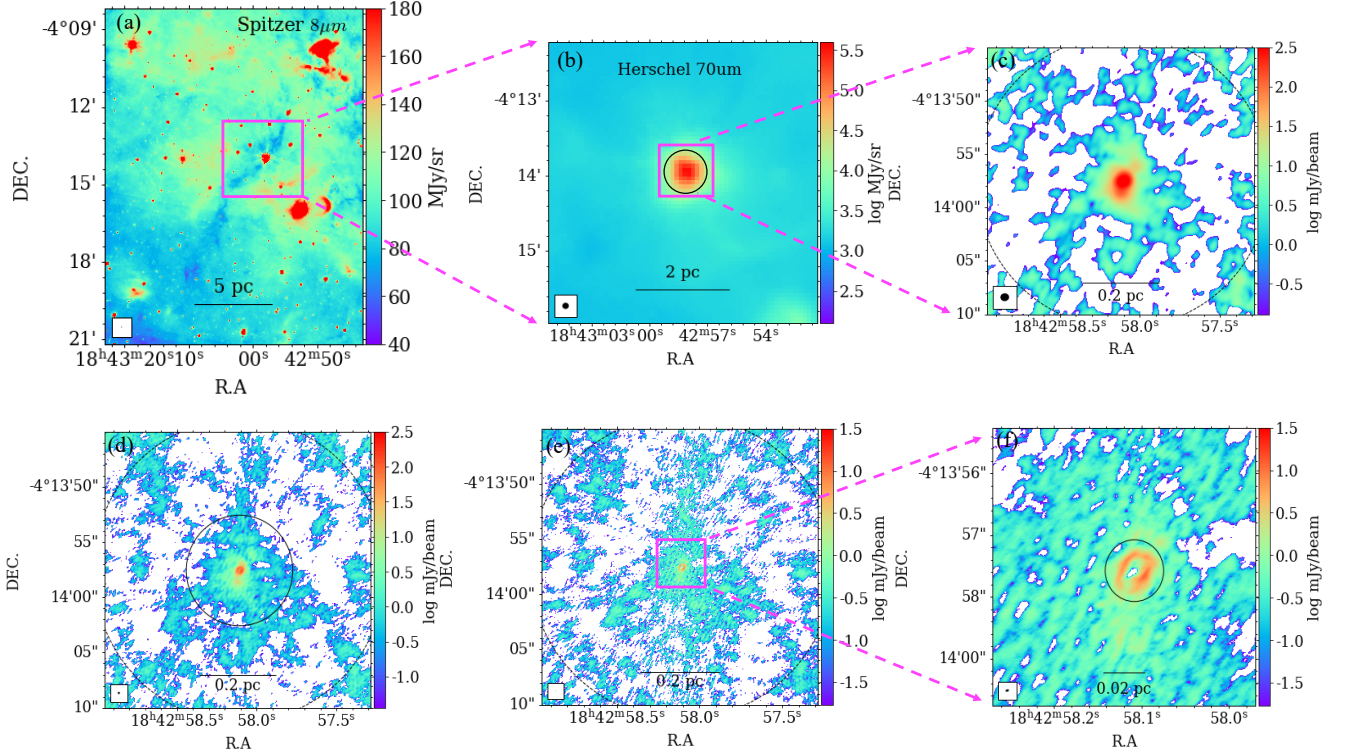


Figure 1: Multi-scale views of the G28.2-0.05 massive protostar. (a) *Top left:* Spitzer $8\ \mu\text{m}$ intensity map of the ~ 20 -pc scale region. A filamentary IRDC, from which the massive protostar appears to have formed, is visible as a dark shadow. The *Spitzer* spatial resolution is $2''$. (b) *Top middle:* Herschel $70\ \mu\text{m}$ continuum image of the ~ 5 pc scale region. The *Herschel* PACS spatial resolution is $5''$. (c) *Top right:* ALMA 1.3 mm compact (C) configuration only continuum map, with color stretch such that the lower edge is 0.1σ ($\sigma = 1.29\ \text{mJy}\ \text{bm}^{-1}$) and upper limit is about $316\ \text{mJy}\ \text{bm}^{-1}$. The dashed circle represents the ALMA 12m primary beam. The beam size for ALMA C configuration is $0.813'' \times 0.735''$. (d) *Bottom left:* The same field of view as (c), but now showing the ALMA 1.3 mm compact + intermediate (C+I) configurations continuum map. The solid circle shows the extent of a $5''$ radius aperture that encloses the main continuum structures and is one scale used for flux measurements. The lower edge of the colorbar extends down to 0.1σ ($\sigma = 0.358\ \text{mJy}\ \text{bm}^{-1}$) intensity level (Section 2). The beam size for ALMA C+I configurations combined is $0.201'' \times 0.217''$. (e) *Bottom middle:* The same field of view as (c), but now showing the ALMA 1.3 mm compact + intermediate + extended (C+I+E) configurations continuum map. The lower edge of the colorbar in extends down to 0.1σ ($\sigma \sim 0.170\ \text{mJy}\ \text{bm}^{-1}$) intensity level. The beam size is $0.060'' \times 0.036''$. (f) *Bottom right:* A zoom in of panel (e) to the inner region of G28.2-0.05, which shows a ring-like structure. The solid circle shows a $0.5''$ radius aperture, which is adopted to measure the flux of the ring. The beam size of $0.060'' \times 0.036''$ is more clearly visible than in panel (e).

On closer examination of the VLA and ALMA images, we notice an apparent offset in peak positions and overall ring structure. Based on 2D Gaussian fits to the 3 peak positions, this offset has a magnitude of $(34.8 \pm 9.5)\text{mas}$ in a direction of P.A. = 216° (from VLA to ALMA). This offset is larger than the astrometric uncertainties of the

VLA ($9\ \text{mas}$)⁵ and ALMA ($3\ \text{mas}$)⁶ observations. The VLA observations were carried out in March 14, 2006, i.e., 11.5 years before our ALMA observations (using the 2017/11/5 date of the longest E configuration observation). Thus, the observed offset corresponds to a proper

⁵ <https://science.nrao.edu/facilities/vla/docs/manuals/oss/performance/positional-accuracy>

⁶ <https://help.almascience.org/kb/articles/what-is-the-astrometric-accuracy-of-alma>

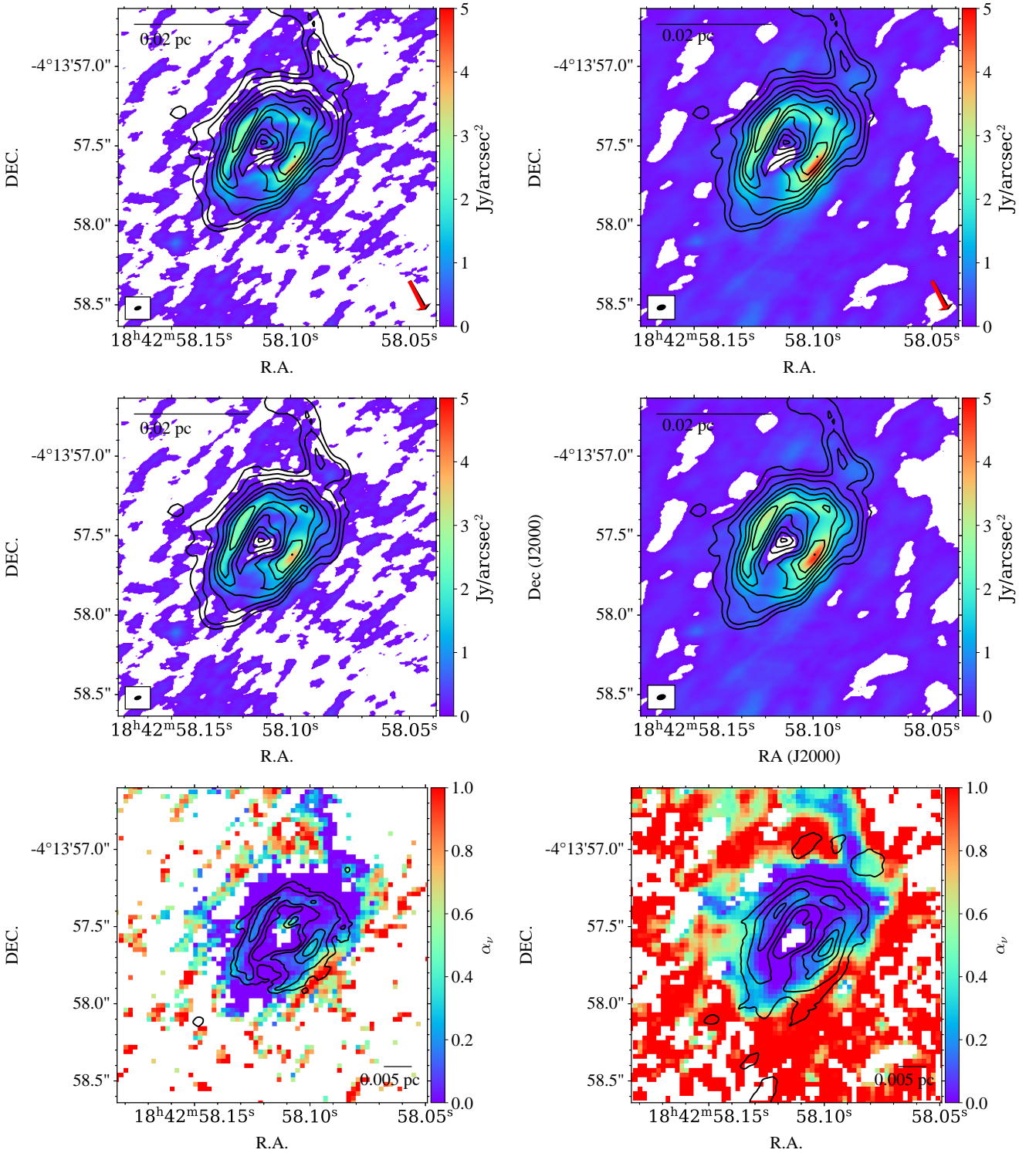


Figure 2: (a) *Top left:* ALMA 1.3 mm continuum image (E config. only) of inner region of G28.2-0.05. The VLA 1.3 cm continuum is shown with contours [0.1, 0.2, 0.4, 0.8, 1.2, 1.6, 2.0, 2.4 Jy/arcsec²]. The beam size of 1.3 mm image is $0.048'' \times 0.026''$ (see inset), while that at 1.3 cm is $0.09''$. An offset of 34.8 mas in direction of P.A. = 216° is seen between the peaks of the VLA and ALMA images (see red arrow in lower right, while black arrow shows direction to Galactic centre). (b) *Top right:* As (a), but now showing 1.3 mm C+I+E combined image, with beam size $0.060'' \times 0.036''$ (see inset). (c) *Middle left:* As (a), but now with the 1.3 cm image translated to align with the 1.3 mm image. (d) *Middle right:* As (b), but now with the 1.3 cm image translated to align with the 1.3 mm image. (e) *Bottom left:* Map of spectral index, $\alpha_\nu = \log(I_{\nu_1}/I_{\nu_2}) / \log(\nu_1/\nu_2)$, where $\nu_1 = 22.4$ GHz and $\nu_2 = 234$ GHz, i.e., evaluated using 1.3 cm and 1.3 mm (E-configuration) fluxes. The contours are the 1.3 mm continuum E configuration image, with levels at [0.5, 1, 1.5, 2, 2.5, 3, 3.5, 4, 4.5, 5, 5.5, 6] Jy/arcsec². (f) *Bottom right:* As (e), but now using the 1.3 mm C+I+E configuration image. The overlaid contours levels are set to be the same as in bottom left panel.

motion of (3.03 ± 0.83) mas yr $^{-1}$, i.e., (82 ± 22) km s $^{-1}$ at the 5.7 kpc distance of source.

The expected proper motion due to Galactic orbital motion (assuming a constant rotation curve of amplitude 200 km s $^{-1}$, solar galactocentric distance of 8.0 kpc and a kinematic distance to the source of 5.7 kpc in the direction of $l = 28.2^\circ$) is 109 km s $^{-1}$ in the direction of decreasing l , i.e., west in Galactic coordinates. The P.A. of this direction along the Galactic plane in R.A.-Dec. projection is 207° . Thus, the observed proper motion, given the uncertainties, is consistent with being entirely in this direction along the Galactic plane. Additional velocity components of ~ 10 km s $^{-1}$ due to non-circular motions in the Galaxy, e.g., due to spiral arms or local turbulence, are also likely to be present, which can also help explain the difference between the observed motion and that predicted by the simple Galactic orbital model. Thus, overall, we conclude that the observed magnitude is approximately consistent with that expected due to Galactic orbital motion. We note that if the source was at the far kinematic distance (9.1 kpc), then the expected motion would be larger, i.e., 243 km s $^{-1}$, corresponding to 5.63 mas yr $^{-1}$. This is supporting evidence that the source is indeed at the near kinematic distance.

We proceed by correcting for the apparent offset, i.e., by shifting the VLA image so that it best aligns with the ALMA image. These overlaid images, the equivalent of Fig. 2(a) and (b), are shown in Fig. 2(c) and (d). Apart from the general close agreement between the images, we also note the presence of an extended spur of emission in the 1.3 cm image extending from the north of the ring.

We next evaluate the spectral index, α_ν , map of the source based on the ratio of the intensities at 1.3 cm and 1.3 mm. The spectral index can help diagnose the physical processes responsible for the emission. In particular, regions where dust starts to make a dominant contribution to the 1.3 mm flux would have larger values of α_ν . We first re-grid the ALMA image to the VLA resolution (i.e., a pixel scale of $0.03''$) using the `imregrid` function in CASA. The spectral index is defined via

$$\alpha_\nu = \log(I_{\nu_1}/I_{\nu_2}) / \log(\nu_1/\nu_2), \quad (1)$$

where $\nu_1 = 22.4$ GHz and $\nu_2 = 234$ GHz. When making the spectral index map, we only consider pixels that are 4 times the corresponding measured rms noise levels in both the ALMA and VLA images, i.e., 0.0689 Jy/arcsec 2 and 0.00679 Jy/arcsec 2 , respectively. Figures 2(e) and (f) present the maps of α_ν using the E and C+I+E ALMA images, respectively.

We see that α_ν takes values of about 0.1 in the main ring structure, as based on VLA to ALMA C+I+E data. As expected, when only ALMA E configuration is used,

smaller values of α_ν are generally seen, which is likely due to missing flux at 1.3 mm in this case. We notice that toward the main 1.3 mm continuum peak there is a local enhancement of α_ν to values of about 0.5. There are also larger values of α_ν , i.e., $\gtrsim 1$, seen immediately surrounding the ring.

To obtain an average value of the spectral index of the inner region we integrate the flux inside a radius of $0.5''$. At 1.3 cm this flux is 0.550 Jy. At 1.3 mm the flux is 0.546 Jy in the E-configuration image and 0.742 Jy in the C+I+E image. Thus the average values of α_ν of the inner region are -0.00311 ± 0.0614 and 0.128 ± 0.0614 , respectively. These data are shown in Figure 3a, along with previous reported flux measurements from the VLA at 14.7 GHz (0.543 Jy with source size of $1.0'' \times 0.7''$) and 43 GHz (0.645 Jy with source size of $0.9''$) (Sewilo et al. 2011). We see that the three VLA data points and the ALMA C+I+E data point can be well fit by a single power law, i.e., $\alpha_\nu = 0.118 \pm 0.0202$. This suggests that a significant fraction of the 1.3 mm continuum flux on these scales is contributed by free-free emission from ionized gas, since approximately power law behavior is often seen in the radio SEDs of ionized structures in the frequency range where they are transitioning from being partially optically thick to optically thin. However, it remains possible that the free-free emission spectrum deviates from this single power law description, i.e., if it reaches the fully optically thin limiting value of $\alpha_\nu = -0.1$ by ~ 100 GHz. In this case a greater proportion of the 1.3 mm flux would be expected to be contributed by dust.

As a further examination on the presence of dust in this region, we evaluate the ALMA in-band SED, i.e., within Band 6 from 216.575 GHz to 233.926 GHz. We make the same continuum measurements of the inner $0.5''$ region, but now carried out separately in the line-free regions of each of the spectral windows of the observation. These data are shown in Figure 3b, as well as in more detail in Figure 4. Here we assume a 10% calibration uncertainty in the integrated fluxes of each measurement, which dominates over other errors. From the in-band data we measure the following spectral indices (α_ν), depending on which image is used: 0.255 ± 2.93 (E); 2.77 ± 0.714 (C+I+E). We note the following results for other combinations: 1.65 ± 0.258 (I); 1.43 ± 0.350 (C+I). These results suggest the potential presence of dust in the inner region, which leads to a steepening of the spectral index compared to the values seen at longer wavelengths.

If dust is contributing significantly, then we may expect local spatial variations to its contributions. In Figure 5 we present the continuum images (both for E-only

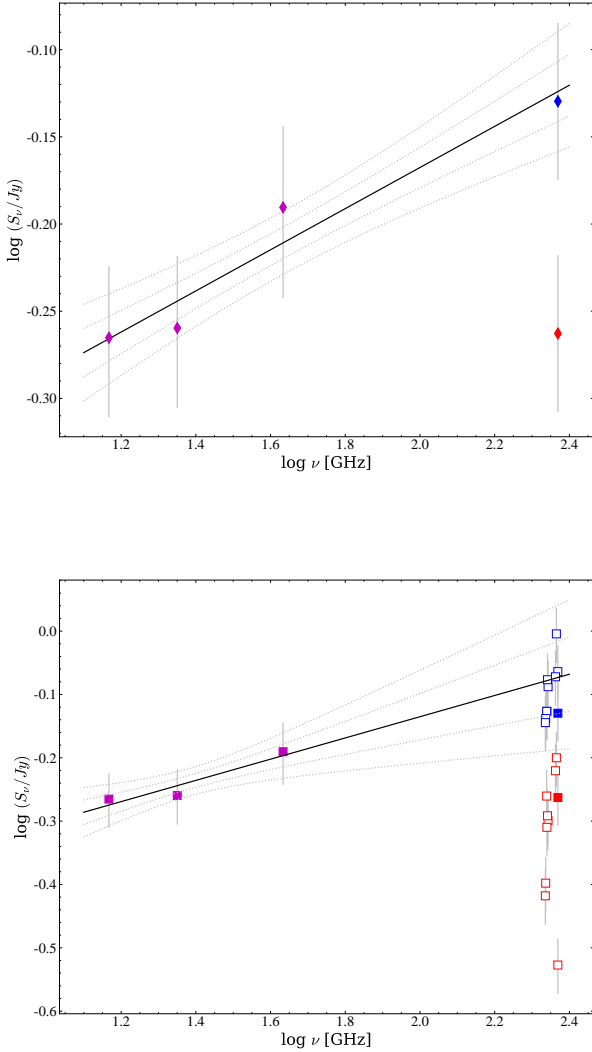


Figure 3: (a) *Top:* Radio to mm SED of the inner $0.5''$ (2,850 au) radius region of G28.2-0.05. Two data points are shown at 230 GHz (1.3 mm) from the ALMA observations. The higher (blue) point is based on the C+I+E combined image, while the lower (red) one is based on the E-only configuration image. Information about the other data points, which are from VLA observations, is given in Table 3. A power law fit to the SED (including ALMA C+I+E measurement) is shown, along with 1σ and 2σ confidence intervals, with derived spectral index of $\alpha_\nu = 0.118 \pm 0.0202$. (b) *Bottom:* As (a), but now showing separate in-band ALMA measurements from 43 to 14.7 GHz (C+I+E - blue open squares; E - red open squares). Solid squares show the equivalent average ALMA fluxes with these configurations from (a). Now the power law fit is only done to the VLA data points and then extrapolated to the ALMA frequencies. This power law has $\alpha_\nu = 0.168 \pm 0.0580$.

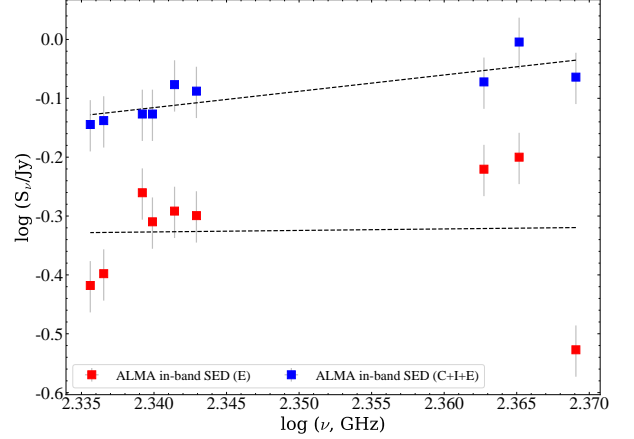


Figure 4: In-band 1.3 mm SED of the inner $0.5''$ (2,850 au) radius region of G28.2-0.05 based on E-only (red points) and C+I+E (blue points) configuration images.

and C+I+E) at 216.575 GHz and 233.926 GHz, i.e., from spectral windows 8 and 0, respectively. We also use these data to present in-band spectral index maps.

While the morphologies are generally quite similar, we notice a modest enhancement of the higher frequency emission in the vicinity of the main continuum peak. In this region of the ring, the in-band value of α_ν has values ~ 1 to 2. Furthermore, the region just outside the ring also shows even larger values. These two features are consistent with those seen in the VLA to ALMA spectral index map.

We thus draw the tentative conclusion that there is dust present in the inner region around the G28.2-0.05 protostar, especially around the main continuum peak and in surrounding regions outside of the ring. We will see below that there is evidence that the protostar is located at the position of the main continuum peak. However, these results motivate the need for high resolution imaging at other frequencies, especially around ~ 300 GHz and higher to better confirm the presence of dust on these scales.

We proceed by making an approximate estimate of the 1.3 mm continuum flux from dust inside $0.5''$. For this we simply take the difference in fluxes between 234 GHz and 217 GHz based on the in-band power law fit, i.e., $0.94 - 0.75 = 0.19$ Jy. For optically thin dust emission, 1.3 mm flux density corresponds to a mass surface den-

sity of

$$\begin{aligned} \Sigma_{\text{mm}} &= 369 \frac{F_\nu (1'')^2}{\text{Jy } \Omega} \frac{\lambda_{1.3}^3}{\kappa_{\nu,0.00638}} \\ &\times \left[\exp \left(0.111 T_{d,100}^{-1} \lambda_{1.3}^{-1} \right) - 1 \right] \text{g cm}^{-2} \quad (2) \\ &\rightarrow 43.2 \frac{F_\nu (1'')^2}{\text{Jy } \Omega} \text{g cm}^{-2}, \end{aligned}$$

where F_ν is the total integrated flux over solid angle Ω , $\kappa_{0.00638}$ is the dust absorption coefficient normalised to $0.00638 \text{ cm}^2 \text{ g}^{-1}$. This fiducial value has been derived assuming an opacity per unit dust mass of $0.899 \text{ cm}^2 \text{ g}^{-1}$ (i.e., from the moderately coagulated thin ice mantle model of [Ossenkopf & Henning 1994](#)) and a gas-to-refractory-component-dust ratio of 141 ([Draine 2011](#)). We note that the mass surface density is sensitive to the temperature of the dust, with the above value normalized to $T_{d,100} \equiv T_d/100 \text{ K} = 1$. Values of $T_d = 50 \text{ K}$ and 200 K change the coefficient by factors of 2.12 and 0.486, respectively.

Applying equation (2) to the inner $0.5''$ circular aperture of G28.2-0.05, i.e., with $\Omega = 0.785 \text{ arcsec}^2$, we estimate $\Sigma_{\text{mm}} = 10.5 \text{ g cm}^{-2}$ (averaged over this region). This corresponds to a mass of $30.3 M_\odot$. This mass is consistent with the $33 M_\odot$ reported in the literature ([Hernández-Hernández et al. 2014](#)). If T_d is in the range from 50 to 200 K, the mass would thus be in the range from about 60 to $15 M_\odot$.

It is possible that the optically thin assumption used for these mass estimates is not valid. To see this, we evaluate the dust optical depth $\tau = \kappa_\nu \Sigma_{\text{mm}}$. For our fiducial estimate of $\Sigma_{\text{mm}} = 10.5 \text{ g cm}^{-2}$, we have $\tau = 0.067$, which implies the optically thin approximation is valid. As shown in Figure 6, only if the dust temperature is as low as $\sim 20 \text{ K}$ does τ start to become significant. However, as discussed below, such low temperatures are not expected to be realistic for this region that is so close to a massive protostar. On the other hand, these estimates assume the dust is spread out uniformly over the $0.5''$ scale region. The actual distribution is likely to show some spatial concentration and thus involve higher values of Σ_{mm} . If the 0.19 Jy emission from dusty gas is concentrated in a region of 10 times smaller area, then Figure 6 shows that $\tau \sim 1$ for $T \lesssim 100 \text{ K}$ and the method using the optically thin assumption would underestimate the mass by a significant factor. We will return to these mass estimates when discussing other inferred protostellar properties.

3.3. Hot Core Environment

The structure and kinematics of hot molecular core emission lines that trace dense and warm molecu-

lar gas can also be used to characterize the protostar. Figure 7 shows moment 0 maps of a lower excitation line of $\text{H}_2\text{CO}(3_{2,1} - 2_{2,0})$, $E_{\text{up}} = 68.1 \text{ K}$, a higher excitation line of $\text{H}_2\text{CO}(9_{1,8} - 9_{1,9})$, $E_{\text{up}} = 174 \text{ K}$, $\text{CH}_3\text{OH}(4_{-2,3} - 3_{-1,2})$, $E_{\text{up}} = 45.46 \text{ K}$, and $\text{CH}_3\text{OCH}_3(22_{4,19} - 22_{3,20})$, $E_{\text{up}} = 253.41 \text{ K}$. We see that the two higher excitation species are concentrated in a region that is close to and overlapping with the main mm continuum peak, but with a slight offset of about $0.2''$ (i.e., $\sim 1000 \text{ au}$). Some emission from these species is also seen extending around and just exterior to the mm continuum ring. The two lower excitation species have a more extended distribution with their strongest emission just exterior to the mm continuum ring. These results indicate that there is dense, warm molecular gas present just outside the ring, but also even hotter gas near the main mm continuum peak and likely to be heated by a source at this location. The upper state energies of these transitions indicates that a typical value of $\sim 100 \text{ K}$ for the dust temperature used above is a reasonable choice in the inner $0.5''$ scale region.

In addition, other molecules are detected in the spectra of G28.2-0.05, both relatively simple, such as $\text{SO}_2(22_{2,20} - 22_{2,21})$, $E_{\text{up}} = 248.44 \text{ K}$, $\text{H}_2\text{S}(2_{2,0} - 2_{1,1})$, $E_{\text{up}} = 83.98 \text{ K}$, to more complex hot core lines, such as $\text{C}_2\text{H}_5\text{CN}(27_{1,27} - 26_{1,26})$, $E_{\text{up}} = 157.73 \text{ K}$. Thus, G28.2-0.05 appears to be a relatively chemically rich massive protostar, e.g., compared to other sources studied with the same spectra set up, such as G339.88-1.26 ([Zhang et al. 2019b](#)), IRAS 07299-1651 ([Zhang et al. 2019a](#)) or G35.20-0.74N ([Zhang et al. 2022](#)). A detailed chemical characterisation of G28.2-0.05 will be presented in a companion paper to this one ([Gorai et al., in prep.](#)).

In Figure 8 we show the average spectra of the four lines shown in Fig. 7. These spectra exhibit a central main Gaussian peak, but with evidence of high velocity line wings, especially to more redshifted velocities. The lines peak at velocities close to the reported literature source systemic velocity of 95.6 km/s (see §1). Hence, we adopt this value as the systemic velocity of the source throughout this work.

In Figure 9 we present the moment 0, 1 and 2 maps of the CH_3OCH_3 line. The velocities near the main mm continuum peak are seen to be close to the systemic velocity of $+95.6 \text{ km s}^{-1}$, but become blueshifted by several km/s as one moves around the ring. The moment 2 map, which shows the estimate of the 1D line of sight velocity dispersion, σ , exhibits values as high as 2.5 km s^{-1} near the main mm continuum peak.

We now use the velocity dispersion of the highest excitation species, i.e., the CH_3OCH_3 line, to estimate a dynamical mass of the protostar assuming it traces

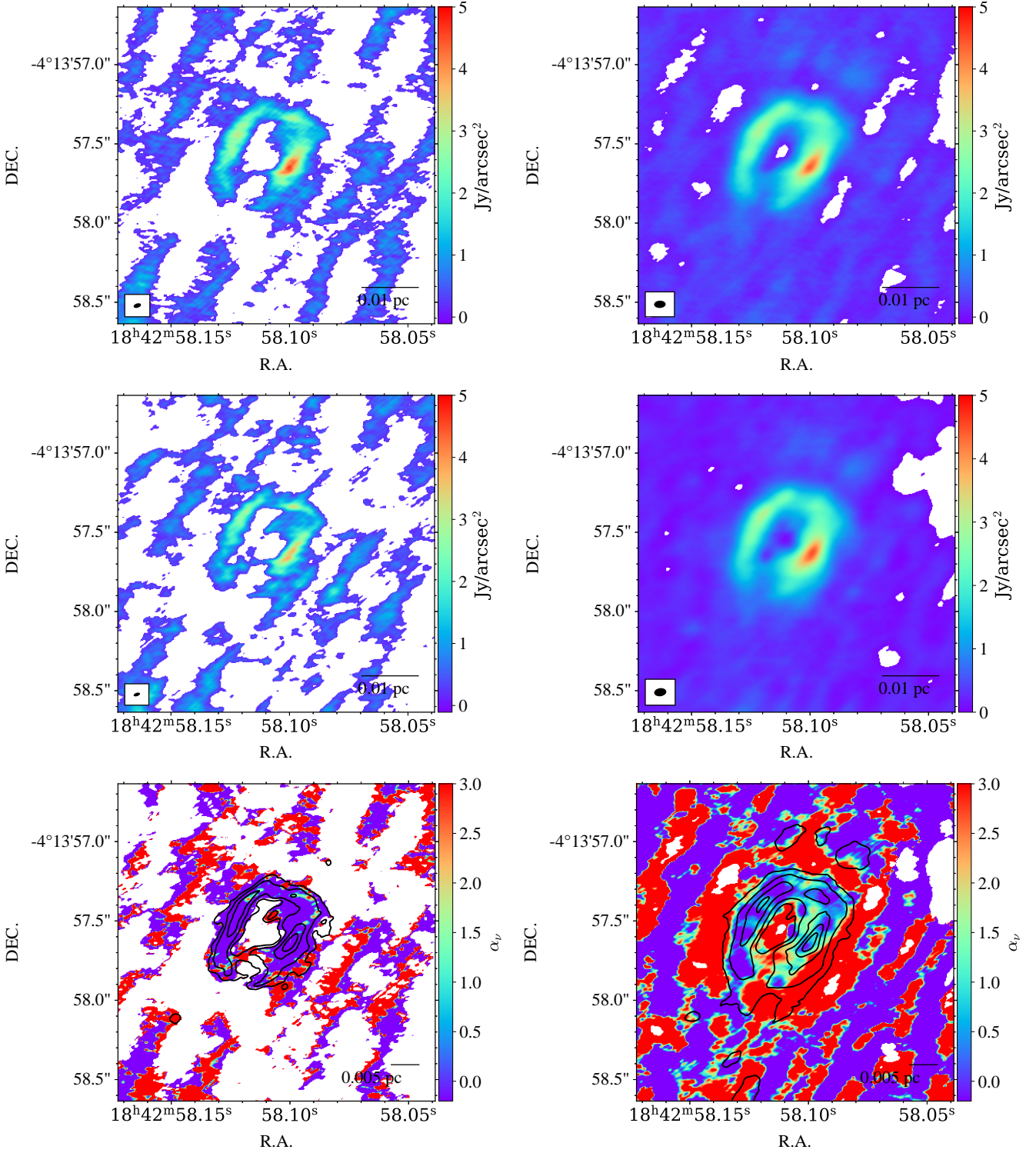


Figure 5: Top row: 216.575 GHz (spw8) continuum images of E only and C+I+E combined respectively. The beam sizes are accordingly $0.042'' \times 0.021''$ and $0.073'' \times 0.046''$. Middle row: Similar to the top row, but for 233.926 GHz (spw0). The beam sizes are respectively $0.048'' \times 0.027''$ and $0.077'' \times 0.051''$. Bottom row: E only and C+I+E combined spectral index map between spw8 and spw0 ($\alpha_\nu = \log(I_{\nu_1}/I_{\nu_2}) / \log(\nu_1/\nu_2)$, where $\nu_1 = 216.575$ GHz and $\nu_2 = 233.926$ GHz). The overlaid continuum contours levels are respectively the same as in Figure 2.

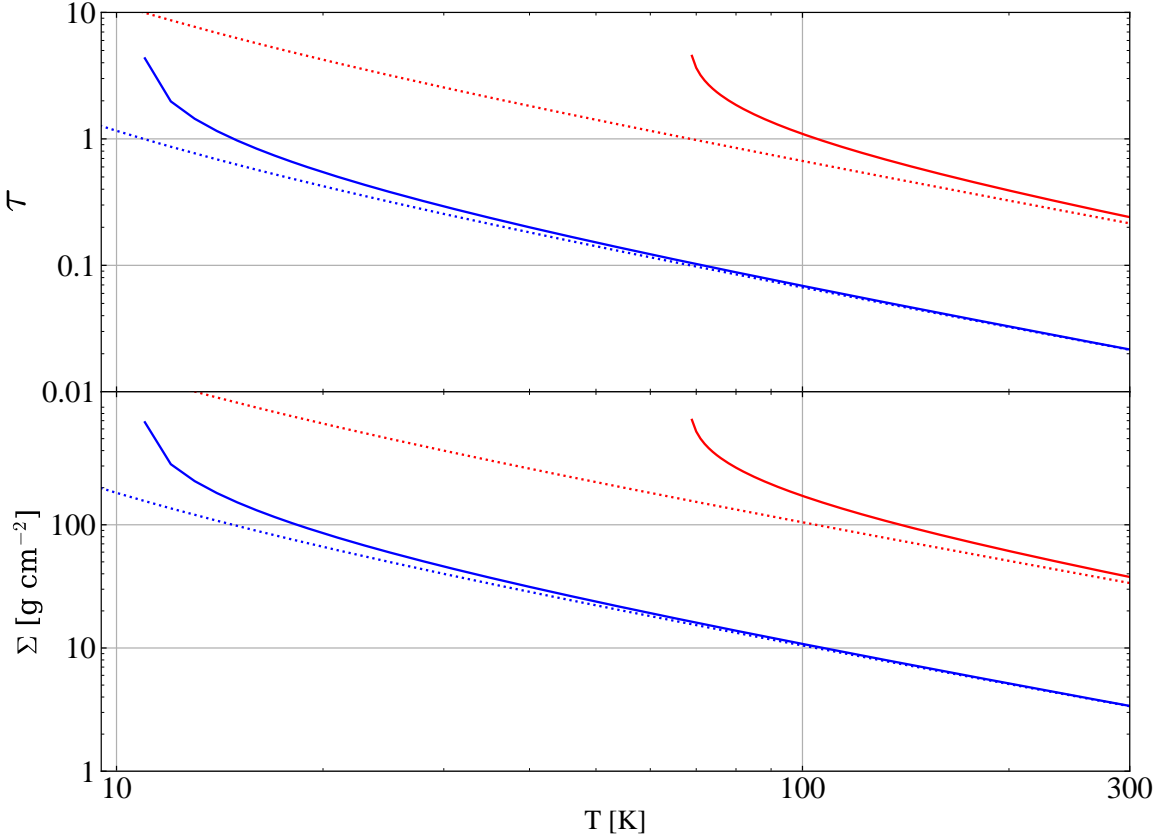


Figure 6: (a) *Top:* Optical depth (τ) of inner-scale dust around G28.2-0.05, i.e., within a projected radius of $0.5''$ (2,850 au), versus assumed dust temperature. The blue dotted line shows τ evaluated from a uniform face-on slab of material in this region, with its mass surface density estimated assuming 0.19 Jy is due to optically thin dust emission at 1.3 mm. The solid blue line shows the equivalent τ , but allowing for optical depth in the slab. The red dotted and solid lines show the equivalent cases when assuming this 1.3 mm continuum emission is concentrated in a 10 times smaller area, e.g., a uniform slab of radius 900 au. (b) *Bottom:* As (a), but now showing the implied mass surface densities, Σ_{mm} , of the slabs.

virialized motions of a region extending out to radius, $R = 1,700$ au ($0.3''$). This radius is justified as being the approximate extent of the emission from the main mm continuum peak. The measured 1D velocity dispersion in this region is $\sigma = 2.95 \text{ km s}^{-1}$. Thus the dynamical mass assuming virial equilibrium is $M_{\text{dyn}} = 5\sigma^2 R/G \simeq 84 M_{\odot}$. The uncertainty in this mass estimate is at least $\sim 20\%$ due to kinematic distance uncertainty to the source and choice of radius of region traced by CH_3OCH_3 emission. Furthermore, the method assumes virial equilibrium of material distributed in a uniform density sphere, which is an idealization of the actual distribution of the gas. Nevertheless, we see that the dynamical mass estimate is comparable to the previ-

ous estimate of dusty gas mass, but is about a factor of two larger. The dynamical mass is expected to be larger since it probes the potential of the total mass enclosed in the region, i.e., of the gas and the protostar.

3.4. $H30\alpha$ emission

Figure 10 presents the moment 0, 1 and 2 maps of $H30\alpha$, only including pixels with values five times larger than the root mean square noise measured from line free channels in the neighborhood of the spectral line. The moment 0 map shows a structure, including ring and extended NW-SE emission, that has close correspondence to the 1.3 mm continuum emission. This is additional evidence that a large fraction of the 1.3 mm continuum

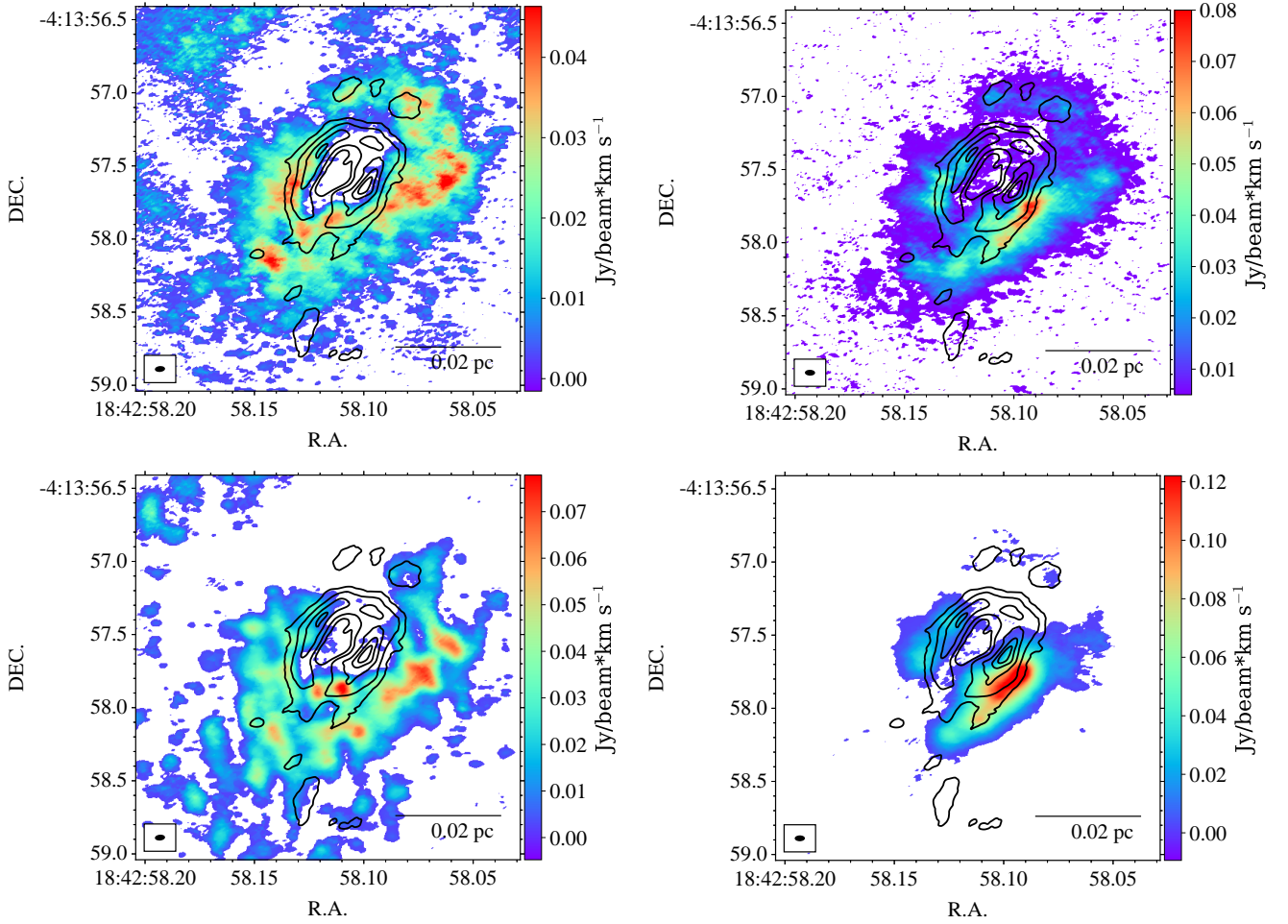


Figure 7: (a) *Top left:* Moment 0 map of $\text{H}_2\text{CO}(3_{2,1} - 2_{2,0}$, $E_{\text{up}} = 68.1$ K) only considering cells above 1σ of the spectral rms measured over representative emission free channels. The black contours show the 1.3 mm continuum emission (0.5, 1, 1.5, 2, 2.5, 3, 3.5, 4, 4.5, 5, 5.5, 6 Jy/arcsec²). (b) *Top right:* As (a), but for $\text{H}_2\text{CO}(9_{1,8} - 9_{1,9}$, $E_{\text{up}} = 174$ K). (c) *Bottom left:* As (a), but for $\text{CH}_3\text{OH}(4_{-2,3} - 3_{-1,2}$, $E_{\text{up}} = 45.46$ K). (d) *Bottom right:* As (a), but for $\text{CH}_3\text{OCH}_3(22_{4,19} - 22_{3,20}$, $E_{\text{up}} = 253.41$ K).

emission is tracing ionized gas, as already concluded from the 1.3 cm to 1.3 mm spectral index analysis.

The moment 1 map reveals a very strong velocity gradient towards the main mm continuum peak. At the location of the peak, the velocity is close to the $+95.6$ km s⁻¹ systemic velocity of the protostar inferred from molecular lines (see above). Then, in the direction of elongation of the mm continuum source there is an ordered, relatively smooth gradient to blueshifted velocities in the SE and redshifted velocities in the NW, with velocities differences of up to ± 10 km s⁻¹ being observed. We will see later in §3.5 that this direction of H30 α velocity gradient is perpendicular to a large-scale CO outflow from the region. This fact suggests that rotation, either in a disk or in a disk wind, plays a role in setting this kinematic structure, which we dis-

cuss in more detail below. Other features seen in the moment 1 map include that the NE side of the ring and northern spur have blueshifted velocities, again by about 10 km s⁻¹ from the systemic. The southern spur, which connects to the main mm continuum peak, shows redshifted velocities by up to about 10 km s⁻¹ from the systemic. The moment 2 map shows that 1D velocity dispersions can exceed 10 km s⁻¹ in the ring, but have much lower values in the northern and southern spurs.

Figure 10d presents a map of the ratio of H30 α integrated intensity to 1.3 mm continuum. The ratio between H30 α integrated intensity and free-free continuum intensity for optically thin Local Thermodynamic Equilibrium (LTE) conditions is (see, e.g., Zhang et al.

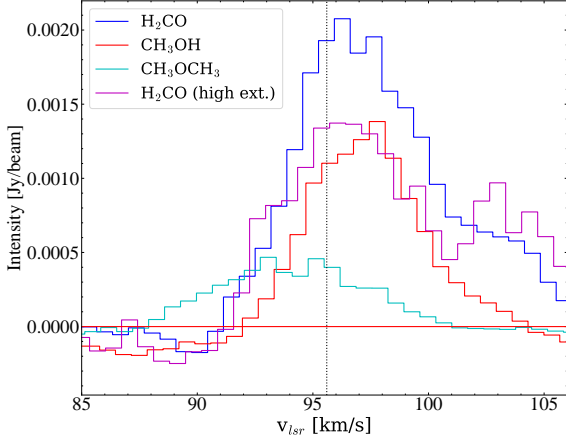


Figure 8: Averaged $\text{H}_2\text{CO}(3_{2,1} - 2_{2,0}, E_{\text{up}} = 68.1 \text{ K})$ (cyan), $\text{CH}_3\text{OH}(4_{-2,3} - 3_{-1,2}, E_{\text{up}} = 45.46 \text{ K})$ (magenta), $\text{H}_2\text{CO}(9_{1,8} - 9_{1,9}, E_{\text{up}} = 174 \text{ K})$ (gold), and $\text{CH}_3\text{OCH}_3(22_{4,19} - 22_{3,20}, E_{\text{up}} = 253.41 \text{ K})$ (gray) spectrum of G28.2-0.05 over an aperture $3''$ radius. We notice the lines both show good Gaussian-like single peak shape. The black dotted line shows the systemic velocity from the literature at 95.6 km/s , which is consistent to the peaks of both lines. Hence, we adopt the literature value as the systemic velocity of the source and used through this work.

2019a)

$$\frac{\int I_{\text{H30}\alpha} dv}{I_{1.3\text{mm}}} = \frac{4.678 \times 10^6 \text{ km s}^{-1} (T_e/\text{K})^{-1}}{[1.5 \ln(T_e/\text{K}) - 8.443](1 + N_{\text{He}^+}/N_{\text{H}^+})}. \quad (3)$$

For an ionized gas temperature of $T_e = 10^4 \text{ K}$ and $N_{\text{He}^+}/N_{\text{H}^+} = 0.1$, we obtain a reference value for the ratio of 79 km s^{-1} . If the temperature is as low as $5,000 \text{ K}$, then the value increases to about 200 km s^{-1} .

Most of the $\text{H30}\alpha$ emitting region shows line to continuum ratios $\lesssim 200 \text{ km s}^{-1}$, which could thus be consistent with optically thin LTE conditions. Some relatively low values could be due to the presence of dust contributions to the mm continuum, e.g, in the regions just outside the ring.

We next consider if the implications of the kinematics of the $\text{H30}\alpha$ emission for the dynamics of the system. The spectrum of this emission extracted from a region with radius of $0.3''$ around the main mm continuum peak is shown in Figure 11. If we attempt a virial analysis based on the velocity dispersion within this region, as was done above for CH_3OCH_3 emission, we find that the 1D velocity dispersion is 14.2 km s^{-1} and so $M_{\text{dyn}} = 5\sigma^2 R/G \simeq 2,000 M_{\odot}$, i.e., $> 20\times$ larger

than that inferred from CH_3OCH_3 . We conclude that the $\text{H30}\alpha$ emission is most likely to be tracing an ionized wind that is escaping from the massive protostar. For example, this may be the ionized base of a rotating magnetocentrifugally launched disk wind. Such winds typically achieve speeds of order the escape speed from their launching radii, r_{dw} , i.e.,

$$v_{\text{w,esc}} = 23.0 \left(\frac{m_*}{30 M_{\odot}} \right)^{1/2} \left(\frac{r_{\text{dw}}}{100 \text{ au}} \right)^{-1/2} \text{ km s}^{-1}. \quad (4)$$

Inspection of Figure 11 reveals that there is high velocity $\text{H30}\alpha$ -emitting gas out to at least 30 km s^{-1} to both redshifted and blueshifted velocities. The models of rotating ionized disk winds of Tanaka et al. (2016) (e.g., see their Figs. 15 and 16) appear to be highly relevant to explain the general features of broad line-width with large-scale velocity gradient that we see in the $\text{H30}\alpha$ emission from G28.2-0.05.

3.5. CO and SiO Outflows

Figure 12 presents the moment 0 maps of $^{12}\text{CO}(2-1)$ emission that traces outflowing molecular gas: the blueshifted emission is integrated from $+80$ to $+95 \text{ km s}^{-1}$; the redshifted emission is integrated from $+96$ to $+115 \text{ km s}^{-1}$. The overall morphology is that expected from a wide-angle bipolar outflow, with the P.A. of the near-facing blueshifted outflow axis being in the NE direction ($\sim 43^\circ$, i.e., consistent with being perpendicular to both the major axis of the main mm continuum peak and the direction of maximum velocity gradient of $\text{H30}\alpha$ emission. Note that there is some redshifted $\text{CO}(2-1)$ emission in the NE direction (and some blueshifted emission in the SW direction), as would be expected in a wide-angle outflow. This morphology is consistent with the previous study of Klaassen et al. (2011).

SiO line emission is another tracer of protostellar outflows. It is expected to be strong in regions of faster flows and/or strong shocks that may lead to destruction or sputtering of dust grains, which then enhances the gas phase abundance of SiO . Figure 12 shows blueshifted ($+80$ to $+95 \text{ km s}^{-1}$) and redshifted ($+96$ to $+115 \text{ km s}^{-1}$) integrated intensity maps of $\text{SiO}(5-4)$ emission. This emission is much sparser than the high velocity $\text{CO}(2-1)$ emission. The blueshifted SiO is again found mostly in the NE direction and at a narrower range of position angles from the protostar, i.e., apparently tracing the more central part of the cavity. Some redshifted emission is also seen in this region. The SiO emission is much weaker towards the SW side, where there it is dominated by a modest knot of redshifted emission.

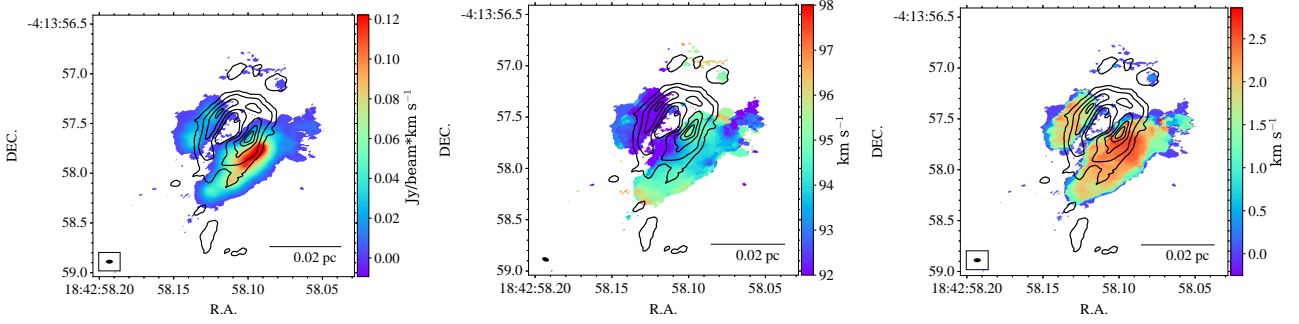


Figure 9: Moment 0, 1 and 2 maps (left to right) of $\text{CH}_3\text{OCH}_3(22_{4,19} - 22_{3,20}$, $E_{\text{up}} = 253.41$ K) emission, only including pixels that are above 1σ spectral rms (see Table 2 spw7). The black contours show the 1.3 mm continuum emission (0.5, 1, 1.5, 2, 2.5, 3, 3.5, 4, 4.5, 5, 5.5, 6 Jy/arcsec²).

Figure 13 presents spectra of CO(2-1) and SiO(5-4) extracted from a region of radius $10''$ centered on the protostar (based on C configuration data). In the CO spectrum, we see there is an absence of signal near the systemic velocity, likely due to absorption from ambient gas. CO emission is seen to extend to velocities that are up to about $\pm 25 \text{ km s}^{-1}$ from the systemic velocity of the system. The SiO(5-4) spectrum is more continuous, peaking near the systemic velocity, but also extending out to over the same velocity range seen in CO(2-1).

Based on this extracted spectrum, Figure 14 presents an analysis of the CO-traced outflow mass and momentum, following the methods of Zhang et al. (2019b) that were applied to similar data for the G339.88-1.26 massive protostar. The key assumptions of this method are the choice of CO abundance, i.e., $X_{\text{CO}} = [^{12}\text{CO}/\text{H}_2] = 10^{-4}$, the choice of excitation temperature, i.e., $T_{\text{ex}} = 10 - 50 \text{ K}$ (see also Dunham et al. 2014) and the assumption that the emission is optically thin. We follow Zhang et al. (2019b) to adopt a fiducial excitation temperature of 17.5 K, which minimizes the mass estimate from the (2-1) transition. A choice of $T_{\text{ex}} = 50 \text{ K}$ will increase the mass by a factor of 1.5.

From this analysis we obtain the following fiducial estimates that should be regarded as minimum values. We find masses of outflowing gas of $0.464 M_{\odot}$ and $1.06 M_{\odot}$ in the blue and redshifted components, respectively. These components have total momenta of $3.93 M_{\odot} \text{ km s}^{-1}$ and $10.8 M_{\odot} \text{ km s}^{-1}$, respectively. The mean (mass-weighted) velocities of the components are thus 8.48 km s^{-1} and 10.2 km s^{-1} , respectively. We associate the outflows with a size of $10''$, i.e., $L_{\text{out}} = 57,000 \text{ au}$, and so the outflow timescales are $3.19 \times 10^4 \text{ yr}$ and $2.65 \times 10^4 \text{ yr}$, respectively. Thus the mass flow rates are $1.46 \times 10^{-5} M_{\odot} \text{ yr}^{-1}$ and $4.00 \times 10^{-5} M_{\odot} \text{ yr}^{-1}$ and the momentum injection rates are $1.23 \times 10^{-4} M_{\odot} \text{ km s}^{-1} \text{ yr}^{-1}$ and $4.07 \times 10^{-4} M_{\odot} \text{ km s}^{-1} \text{ yr}^{-1}$, respectively.

Figure 14 also shows the distribution of mass with velocity. Such distributions are important diagnostics that can be compared with theoretical models of massive protostellar outflows (e.g., Staff et al. 2019). In principle, such comparisons allow constraints to be placed on the evolutionary stage, inclination of outflow axis to the line of sight and other properties of the protostellar core.

The same figure also presents the mass spectrum of the outflow with a log-log scaling. In this panel we also compare with the outflow mass spectra of G339.88-1.26 (Zhang et al. 2019b), which is more collimated and thus likely to be at an earlier evolutionary stage. We see that G28.20+0.05 has a more powerful low velocity outflow than G339.88-1.26, but the latter has a larger amount of mass at high velocities. Some of these differences could be a result of varying degrees of inclination to the line of sight, however, we suspect that much of the fast outflowing gas that is closer to the outflow axis may have been photodissociated in G28.20+0.05, since this source is already starting to create a HC III region. In this case, the prediction would be that there are relative broad and strong tracers of atomic outflow components, such as [OI] and [CII] lines.

4. PROTOSTELLAR PROPERTIES FROM SED MODELING

The MIR to FIR spectral energy distribution (SED) can be used to constrain protostellar properties. In particular, for core accretion Zhang & Tan (2018) have presented a grid of model SEDs that survey the three intrinsic parameters of initial core mass, M_c , clump mass surface density, Σ_{cl} , and current protostellar mass, m_* . The viewing angle to the outflow axis, θ_{view} , and the level of foreground extinction, A_V , are the remaining two additional parameters that are derived from the SED fitting. All other core properties, such as initial core radius (R_c), current accretion rate (\dot{m}_*), bolometric luminosity

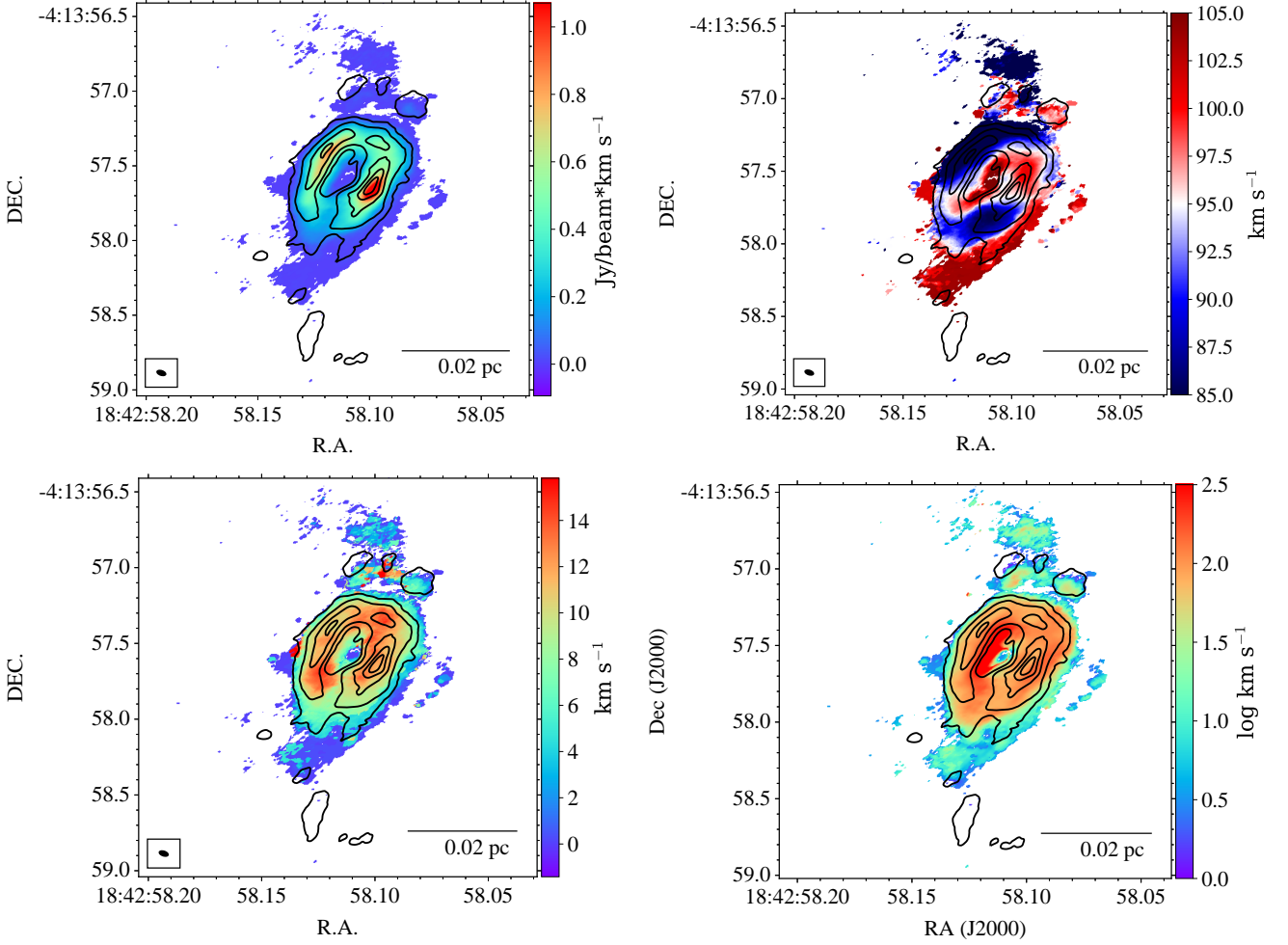


Figure 10: (a) Top left: H30 α moment zero map, only considering pixels with integrated intensity above 5σ of the spectral rms measured over emission free velocity channels in the averaged velocity spectrum ($\sigma_{H30\alpha} \sim 0.8$ mJybm $^{-1}$). The black contours show the 1.3 mm continuum emission (0.5, 1, 1.5, 2, 2.5, 3, 3.5, 4, 4.5, 5, 5.5, 6 Jy/arcsec 2). Bottom left: H30 α moment one map overlaid with 1.3 mm contours. The contours levels are same as in the top left panel. Again, only pixels with H30 α integrated intensity greater than 5σ of the spectral noise are included in showing the moment 1 maps. Bottom right: H30 α to continuum intensity ratio overlaid with 1.3 mm contours. The contours levels are same as in the top left panel.

(L_{bol}) and outflow opening angle, are determined from M_c , Σ_{cl} and m_* .

Figure 15 presents the background subtracted SED of G28.2-0.05 from $3.6 \mu\text{m}$ to 6 cm , i.e., based on archival *Spitzer*-IRAC (3.6 to $8 \mu\text{m}$), *WISE* ($22 \mu\text{m}$) and *Herschel* PACS and SPIRE (70 to $500 \mu\text{m}$). We have also measured the fluxes of the source at 53 and $214 \mu\text{m}$ from *SOFIA*-HAWC+ (Law et al., in prep.).

We compile data from *Herschel* SPIRE/PACS, *WISE*, *Spitzer* IRAC, *SOFIA*-HAWC+, *ALMA* (this work) and archival *VLA* data (Sewilo et al. 2011, and references therein) to construct the spectral energy distribution (SED). Table 3 summarizes the integrated flux densities within an optimal aperture of $15.5''$ radius. The

SOFIA-HAWC+ data is obtained from recent observations (Proj. ID 09_0164, PI: Law, C.Y.) to map the large scale dust continuum and polarization respectively at $53, 89, 154$, and $215 \mu\text{m}$. Here we include the observed and reduced $53 \mu\text{m}$ and $215 \mu\text{m}$ data to construct the multi-wavelength SED. The optimum aperture was defined by which beyond 30% of that radius, the background flux increases is within 10% (Telkamp et al. 2022, in prep). The integrated flux at *Herschel* and *Spitzer* wavelengths are derived following the methods in the SOMA survey (Liu et al. 2019). We fit only the *Herschel*, *WISE*, *Spitzer* and *SOFIA* data to a grid of models following the Zhang & Tan (2018) radiative transfer models. The fitting was performed using the

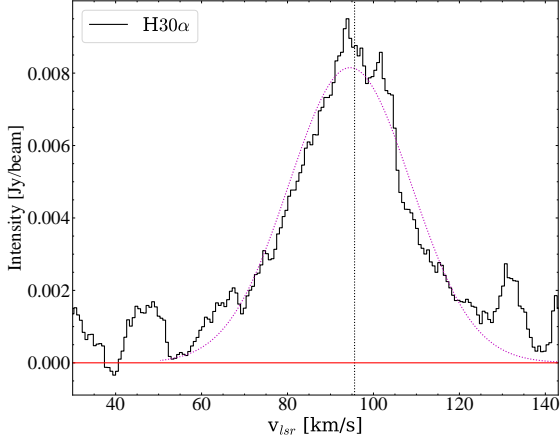


Figure 11: H30 α averaged spectrum toward a circular aperture of 0.3'' radius from the main mm continuum peak. The red dotted line is the Gaussian fit to the spectrum. The corresponding dispersion is 14.2 km/s. The vertical black dotted line represents the systemic velocity of the source.

python package *sedcreator* (ver. 6.0.4)⁷ (Fedriani et al. 2022, in prep.).

The best-fitting model SEDs are plotted in Figure 16. The physical parameters of the best five fitted models are presented in Table 4. Constraints in the main parameter space of M_c , Σ_{cl} and m_* are summarised in Figure 17. These results indicate that G28.20+0.05 harbors a protostar that currently has a mass of $m_* \sim 24 M_\odot$ and is forming from a core with initial mass of $\sim 400 M_\odot$ in a clump with mass surface density of $\Sigma_{cl} \sim 3 \text{ g cm}^{-3}$. We note that this estimate for m_* is consistent with our earlier dynamical mass estimate, if there is also a similar mass in dusty gas present within the 0.3'' scale region of the protostar.

5. FRAGMENTATION PROPERTIES OF G28.20+0.05

We characterise the fragmentation properties of G28.20+0.05 and its surroundings by applying the dendrogram algorithm (Rosolowsky et al. 2008). We carry this out on images before primary beam correction, i.e., so that it has a uniform noise map. Following Cheng et al. (2018), Liu et al. (2018), and O'Neill et al. (2021), the fiducial dendrogram parameters that we use are $\text{minvalue} = 4\sigma$ (the minimum intensity considered in the analysis); $\text{mindelta} = 1\sigma$ (the minimum spacing between

isocontours); $\text{minpix} = 0.5$ beam area (the minimum number of pixels contained within a structure).

In Figure 18 we present the dendrogram identified structures respectively in the C only and C+I configurations. In the C only image, dendrogram finds the main central core, but then only two additional smaller cores (with masses $6.67 M_\odot$, $7.66 M_\odot$ assuming 20 K). Furthermore these two additional cores are quite close to the main core, i.e., within about 4'', and only separated from the main core's boundary by less than one beam FWHM. Thus, there is an absence of dendrogram-detected sources beyond 4'', i.e., beyond about 23,000 au or ~ 0.1 pc. The dendrogram analysis of the C+I image yields a larger number of fragments (or "cores"), but these all overlap with the central region within about 4''. We note that, assuming a temperature of 20 K, the mass sensitivity of the dendrogram analysis for the C image is $1.30 M_\odot$ and the C+I image is $0.387 M_\odot$. For 100 K, these mass sensitivities would decrease by a factor of 6. Thus the main conclusion to be drawn is that there is a lack of compact mm emission sources beyond about 0.1 pc from the massive protostar. Other protostars in the vicinity would be expected to appear as such compact sources. Thus G28.20+0.05 appears to be forming in near splendid isolation.

Close examination of the mm continuum images does reveal a relatively extended ring of emission about 8'' to the south of the main source. This corresponds to a source already noted by Sewilo et al. (2011) based on VLA radio 7 mm and 2 cm data. Such a source likely corresponds to a small HII region around an already formed relatively massive star, e.g., a B star. However, it is not prominent in ALMA 1.3 mm continuum, indicating it does not have a large amount of warm dust around it.

6. DISCUSSION AND CONCLUSIONS

We have presented 1.3 mm continuum and line ALMA observations of the massive protostar G28.2-0.05 ($d = 5.7$ kpc) using three array configurations to achieve sensitivity to a high spatial dynamic range from a MRS of 11'' down to a smallest beam of $\sim 0.04''$, corresponding to about 200 au. Analysis of these data, along with ancillary MIR to FIR data, indicate the presence of a massive protostar with current protostellar mass of $\sim 24 M_\odot$. The protostar is launching powerful outflows, both in the form of a rotating ionized disk wind and as larger-scale molecular flows. Thus it appears to still be undergoing active accretion. At the same time, there is clear evidence that it is starting to produce ionizing feedback within its protostellar core, i.e., by ionizing its disk wind, but also by ionizing some surrounding, denser gas

⁷ <https://github.com/fedriani/sedcreator>

Table 3: Integrated flux density from *Spitzer* 3.6 μm to *VLA* 6 cm

Facility	Wavelength	Integrated intensity	Aperture radius
	μm	Jy	"
<i>Spitzer</i>	3.6	0.424 \pm 0.598	15.5
<i>Spitzer</i>	4.5	1.34 \pm 0.149	15.5
<i>Spitzer</i>	5.8	5.07 \pm 0.567	15.5
<i>Spitzer</i>	8.0	7.740 \pm 1.650	15.5
<i>WISE</i>	22	13.0 \pm 27.5	15.5
<i>SOFIA</i>	53	1449 \pm 144.1	30
<i>Herschel</i>	70	1561 \pm 77.3	15.5
<i>Herschel</i>	160	1222 \pm 282	15.5
<i>SOFIA</i>	215	746 \pm 187	40
<i>Herschel</i>	350	167 \pm 81.9	15.5
<i>Herschel</i>	500	26.9 \pm 33.5	15.5
<i>ALMA</i>	1282	0.827(2.63) ^a	0.5(5.0)
<i>ALMA</i>	1294	0.842(2.28) ^a	0.5(5.0)
<i>ALMA</i>	1301	0.778(2.41) ^a	0.5(5.0)
<i>ALMA</i>	1362	0.756(2.31) ^a	0.5(5.0)
<i>ALMA</i>	1367	0.766(2.32) ^a	0.5(5.0)
<i>ALMA</i>	1372	0.737(2.58) ^a	0.5(5.0)
<i>ALMA</i>	1374	0.739(2.52) ^a	0.5(5.0)
<i>ALMA</i>	1382	0.720(2.05) ^a	0.5(5.0)
<i>ALMA</i>	1385	0.726(2.13) ^a	0.5(5.0)
<i>VLA</i>	6900	0.645 \pm 0.065	0.9 ^b
<i>VLA</i>	13000	0.548 \pm 0.055	0.5
<i>VLA</i>	20000	0.494 \pm 0.050	0.8 \times 0.6 ^b
<i>VLA</i>	36000	0.297 \pm 0.045	3.6 \times 3.8 ^b
<i>ATCA</i>	45000	0.326	1.9 \times 1.9 ^b
<i>VLA</i>	60000	0.150 \pm 0.015	2.19

^a The numbers in brackets are C+I combined enclosed flux within the larger 5'' radius aperture. The corresponding uncertainties of the fluxes are set to be 10% of the flux. ^bThe integrated flux measured in [Sewilo et al. \(2011\)](#) is measured within the source size defined by the long and short axes, thus here we present the two axes values. Also note that the single value in the 6.9 mm measurement is the source size (FWHM), which is adopted from [Sewilo et al. \(2008\)](#).

Table 4: Parameters of the Best Five Fitted Models

χ^2	M_c	Σ	R_{core}	m_*	θ_{view}	A_V	M_{env}	$\theta_{\text{w,esc}}$	\dot{M}_{disk}	$L_{\text{bol,iso}}$	L_{bol}
	M_{\odot}	g cm^{-2}	pc	M_{\odot}	$^{\circ}$	mag	M_{\odot}	$^{\circ}$	$M_{\odot} \text{ yr}^{-1}$	L_{\odot}	L_{\odot}
0.45	400	3.160	0.08	24	13	420.24	361.65	13	1.9e-03	1.3e+06	3.0e+05
0.51	480	3.160	0.09	24	51	394.49	440.54	12	2.0e-03	2.5e+05	2.9e+05
0.54	320	3.160	0.07	24	13	392.25	276.82	15	1.8e-03	1.8e+06	3.1e+05
0.57	400	3.160	0.08	16	22	77.77	368.90	10	1.5e-03	9.7e+04	1.0e+05
0.89	320	3.160	0.07	16	22	89.59	293.14	12	1.4e-03	1.0e+05	1.1e+05

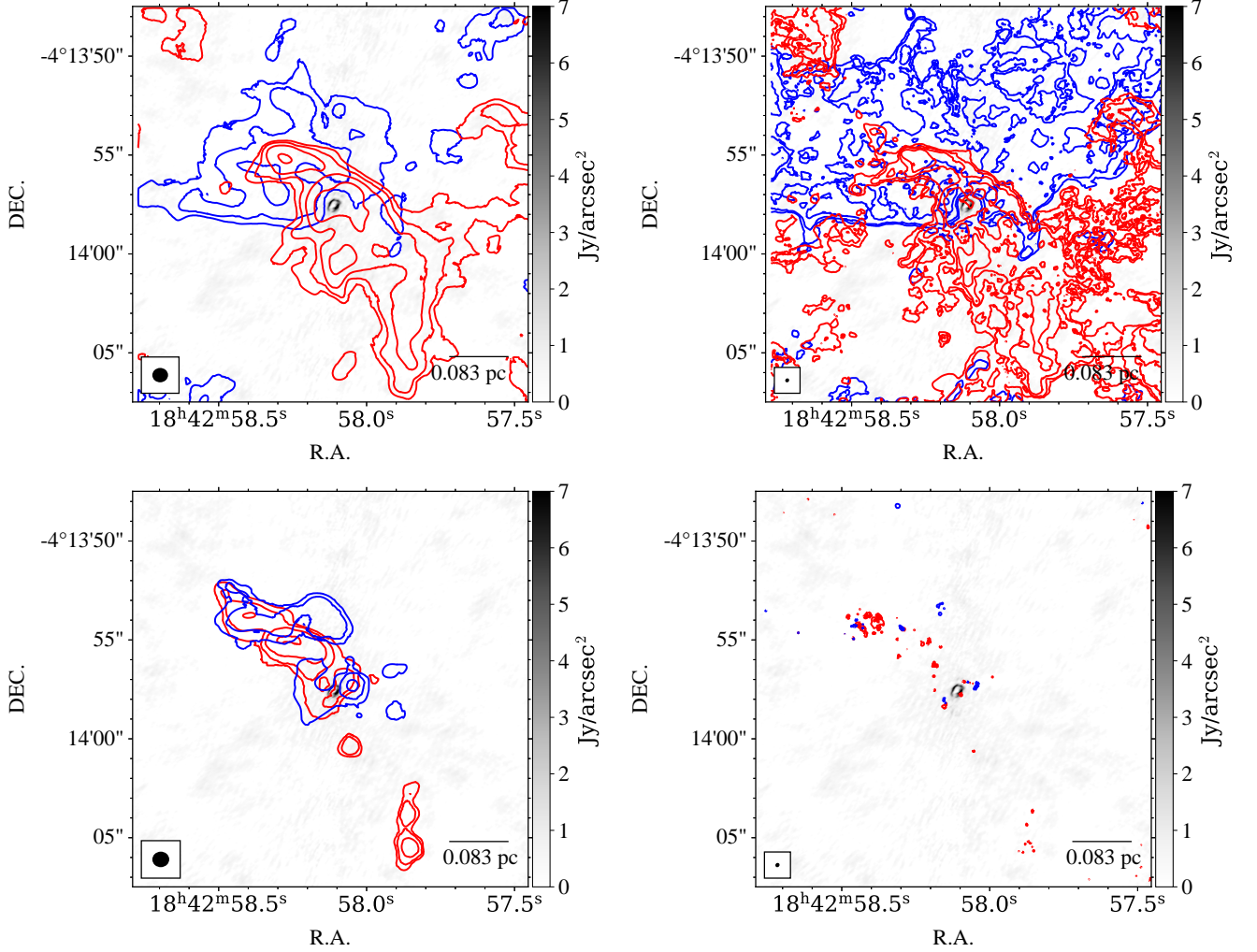


Figure 12: (a) *Top Left:* Integrated intensity maps of CO(2-1) emission tracing outflowing gas as observed in C configuration. The blue contours show blueshifted emission from +80 to +95 km s⁻¹. The contours levels are [1.28, 2.5, 5, 10, 20] Jy bm⁻¹. The red contours show redshifted emission from +96 to +115 km s⁻¹. The contours levels are [1.28, 2.5, 5, 10, 20] Jybm⁻¹. Only pixels that are above 1 σ spectral rms (= 0.31 Jy bm⁻¹) are included. The grey scale shading shows the 1.3 mm continuum image (C+I+E). (b) *Top Right:* As (a), but for C+I combined configurations of CO(2-1) emission. The contours levels for the blueshifted and the redshifted emissions are [0.16, 0.32, 0.64, 1.28, 2.5, 5] Jybm⁻¹. (c) *Bottom Left:* As (a), but now showing integrated intensity maps of SiO(5-4) emission (C configuration). The blue contours show blueshifted emission from +80 to +95 km s⁻¹. The red contours show redshifted emission from +96 to +115 km s⁻¹. The contours levels are [0.16, 0.32, 0.64, 1.28, 2.56, 5.12] mJy bm⁻¹. Only pixels that are above 1 σ spectral rms (= 0.279 mJy bm⁻¹) are included. (d) *Bottom Right:* As (c), but now for C+I combined configurations of SiO(5-4) emission. The contours levels are [0.01, 0.02, 0.04, 0.06, 0.08, 0.1, 0.12] Jy bm⁻¹.

Aperture radius or size	Flux (Jy)	Σ (g cm ⁻²)	Mass (M_{\odot})
		(20K,100K,300K)	(20K,100K,300K)
0.5'' (C+I+E)	0.733	256, 40.4, 13.0	737, 117, 37.4
0.5'' (C+I)	0.809	282, 44.6, 14.3	813, 129, 41.3
5'' (C+I)	2.10	8.28, 1.31, 0.421	2111, 333, 107
All dendrogram leaves	0.450	46.2, 7.32, 2.35	452, 71.6, 23.0

Table 5: Fluxes, mass surface densities and masses of structures identified in ALMA 1.3 mm continuum images of G28.20+0.05 (see text).

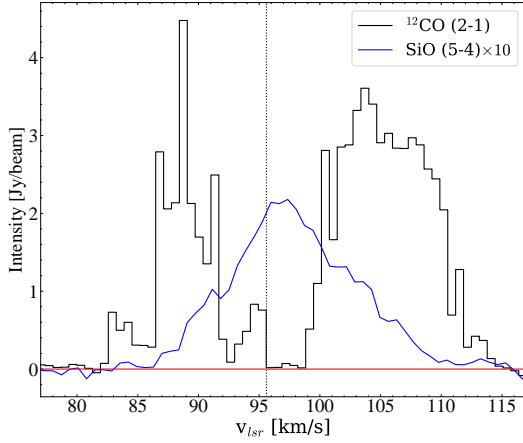


Figure 13: CO(2-1) and SiO(5-4) averaged spectra extracted from a circular aperture of radius 10''.

structures, as evidenced by the presence of a cm to mm free-free emitting “ring”. The nature of this structure is still somewhat uncertain, but could involve the ionized surfaces of dense molecular accretion structures, e.g., filaments or streamers, that are generic features within a massive turbulent core (e.g., McKee & Tan 2002, 2003; Myers et al. 2013). Our cm to mm spectral index analysis suggests the presence of dust in and around this ring, however, higher frequency ALMA observations are needed for a more definitive characterization. Emission lines from dense and warm molecular gas are also seen in this region, and furthermore enable a dynamical mass estimate of $\sim 80 M_{\odot}$ within about 2,000 au scales.

An crucial aspect in massive star formation theory is whether massive stars can form in relatively isolated

environments. Competitive accretion models (e.g., Bonnell et al. 2001) *require* the presence of a surrounding massive protocluster in order for a massive star to form. On the other hand, core accretion models (e.g., McKee & Tan 2003) can be valid in both isolated and in relatively crowded environments. From our analysis of the larger scale 1.3 mm continuum image, we argue that the protostar is forming in an isolated environment, i.e., with no compact and strong 1.3 mm continuum sources identified beyond a 4'' radius, corresponding to ~ 0.1 pc, and extending out over the ALMA FOV to about 0.4 pc in radius. This apparent dearth of protostellar companions in a protocluster around the massive protostar is a strong constraint on massive star formation theories.

ACKNOWLEDGEMENT

We thank M. Sewilo for discussions and providing access to VLA data of G28.20+0.05. This paper makes use of the following *ALMA* data: ADS/JAO.ALMA#2015.1.01454.S *ALMA* is a partnership of ESO (representing its member states), NSF (USA) and NINS (Japan), together with NRC (Canada), MOST and ASIAA (Taiwan), and KASI (Republic of Korea), in cooperation with the Republic of Chile. The Joint *ALMA* Observatory is operated by ESO, AUI/NRAO and NAOJ. This research made use of *astrodendro*, a Python package to compute dendrograms of Astronomical data (<http://www.dendrograms.org/>). Law Chi Yan acknowledges support from the Nordic ALMA Regional Centre (ARC) node based at Onsala Space Observatory. The Nordic ARC node is funded through Swedish Research Council grant No 2017-00648.

REFERENCES

- Bonnell, I. A., Clarke, C. J., Bate, M. R., & Pringle, J. E. 2001, *MNRAS*, 324, 573, doi: [10.1046/j.1365-8711.2001.04311.x](https://doi.org/10.1046/j.1365-8711.2001.04311.x)
- Butler, M. J., & Tan, J. C. 2009, *ApJ*, 696, 484, doi: [10.1088/0004-637X/696/1/484](https://doi.org/10.1088/0004-637X/696/1/484)
- . 2012, *ApJ*, 754, 5, doi: [10.1088/0004-637X/754/1/5](https://doi.org/10.1088/0004-637X/754/1/5)

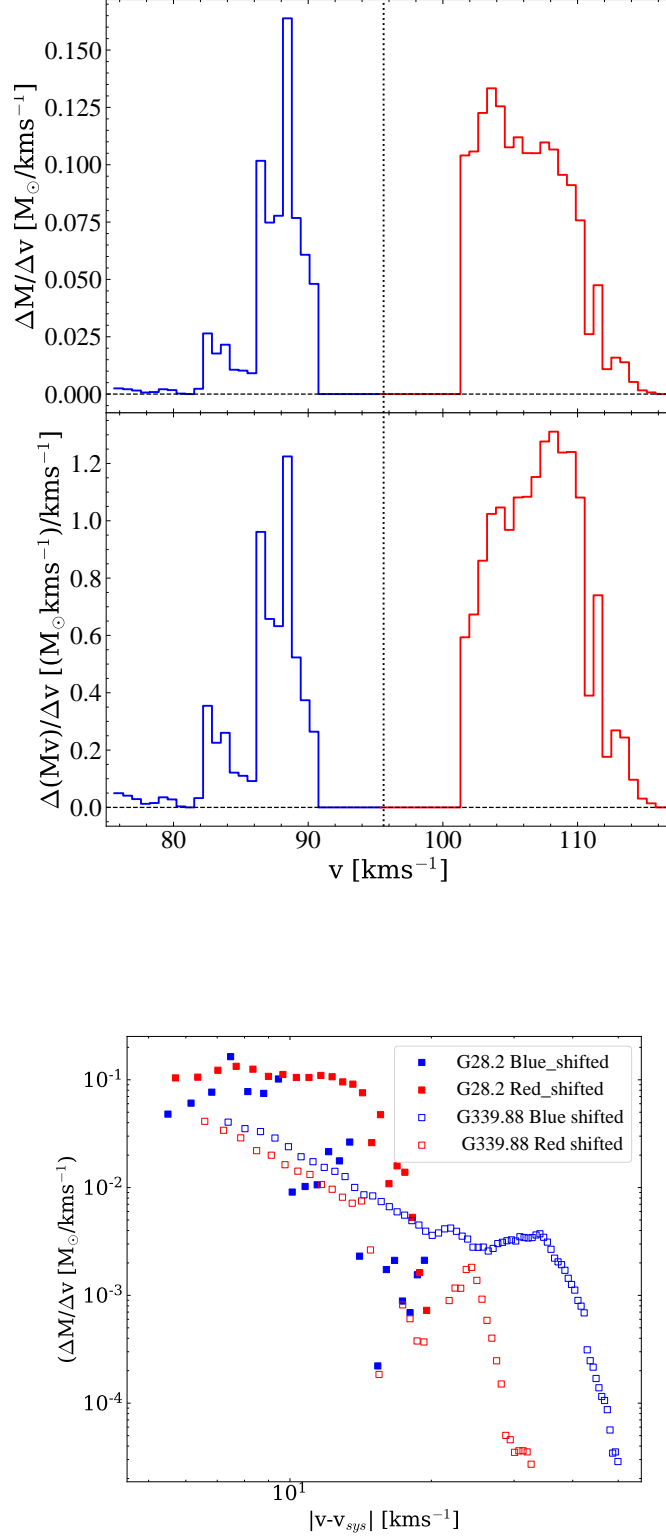


Figure 14: (a) *Top:* Distribution of outflow mass inferred from CO(2-1) versus velocity. (b) *Middle:* Distribution of outflow momentum inferred from CO(2-1) versus velocity. (c) *Bottom:* Mass spectra of blue and redshifted outflow components. The equivalent data from the G339.88-1.26 massive protostar (Zhang et al. 2019b) are also shown.